



## Multimode solitons in optical fibers: a review

YIFAN SUN,<sup>1,2</sup>  PEDRO PARRA-RIVAS,<sup>1</sup>  GOVIND P. AGRAWAL,<sup>3</sup>  TOBIAS HANSSON,<sup>4</sup>   
CRISTIAN ANTONELLI,<sup>5</sup>  ANTONIO MECOZZI,<sup>5</sup>  FABIO MANGINI,<sup>1</sup>  AND STEFAN WABNITZ<sup>1,\*</sup> 

<sup>1</sup>Department of Information Engineering, Electronics, and Telecommunications, Sapienza University of Rome, 00184 Rome, Italy

<sup>2</sup>Service OPERA-Photonique, Université libre de Bruxelles, B-1050 Brussels, Belgium

<sup>3</sup>The Institute of Optics, University of Rochester, Rochester, New York 14627-0186, USA

<sup>4</sup>Department of Physics, Chemistry and Biology, Linköping University, SE-58183 Linköping, Sweden

<sup>5</sup>Department of Physical and Chemical Sciences, University of L'Aquila, 67100 L'Aquila, Italy

\*Corresponding author: stefan.wabnitz@uniroma1.it

Received 6 June 2024; revised 30 July 2024; accepted 30 July 2024; posted 30 July 2024 (Doc. ID 531393); published 31 October 2024

This review describes recent theoretical and experimental advances in the area of multimode solitons, focusing primarily on multimode fibers. We begin by introducing the basic concepts such as the spatial modes supported by a multimode fiber and the coupled mode equations for describing the different group delays and nonlinear properties of these modes. We review several analytic approaches used to understand the formation of multimode solitons, including those based on the 3D+1 spatiotemporal nonlinear Schrödinger equation (NLSE) and its approximate 1D+1 representation that has been found to be highly efficient for studying the self-imaging phenomena in graded-index multimode fibers. An innovative Gaussian quadrature approach is used for faster numerical simulations of the 3D+1 NLSE. The impact of linear mode coupling is discussed in a separate section using a generalized Jones formalism because of its relevance to space-division multiplexed optical communication systems. The last section is devoted to the relevant experimental studies involving multimode solitons. © 2024

Chinese Laser Press

<https://doi.org/10.1364/PRJ.531393>

### 1. INTRODUCTION

In the realm of nonlinear optics, the phenomenon of temporal solitons has been a subject of fascination for over five decades [1,2], ever since the first prediction of temporal solitons in 1973 [3] and their experimental observation in 1980 [4]. These self-sustained wave packets exhibit remarkable properties, propagating over long distances without distortion due to a balance between chromatic dispersion and nonlinearity [see Fig. 1(a)]. Extensive research efforts have been dedicated to unraveling the mysteries of solitons [5] and harnessing them for various applications, spanning from telecommunications [6] to supercontinuum sources [7], ultrafast mode-locked fiber laser sources [8], and cavity soliton frequency combs [9]. Similarly, spatial optical solitons, akin to their temporal counterparts, are self-trapped light beams capable of maintaining their transverse shape while propagating through nonlinear media, avoiding the divergence associated with freely diffracting beams [see Fig. 1(b)]. The presence of light alters the properties of nonlinear materials, such as refractive index, resembling the intensity profile of the beam and forming an optical lens effect. The concept of self-trapped light beams was initially introduced by Askaryan in 1962 [10], followed by comprehensive investigations in both 1D and 2D diffractive systems [11–14].

While traditional temporal or spatial solitons have primarily been explored in one or two dimensions, recent advancements have unveiled a fascinating realm of solitons involving both spatial and temporal degrees of freedom, known as spatiotemporal solitons [5,15,16], also called light bullets [17]. These solitons represent multidimensional states, as they necessitate the balance among diffraction, dispersion, and nonlinearity across spatial and temporal dimensions in the course of their propagation. This complexity presents new challenges as well as interesting opportunities in nonlinear dynamics. One significant challenge is that these multidimensional states are highly susceptible to perturbations [16]. A notable example of this fragility is the spatiotemporal wave collapse, which is commonly observed in multidimensional solitons within optical materials exhibiting Kerr nonlinearity [16,18–20]. Nevertheless, spatiotemporal solitons have been studied in various configurations [20–31]. Among them, multimode fibers (MMFs) provide a convenient test-bed [32] and have garnered considerable interest in the study of such solitons, owing to their cost-effectiveness and ease of alignment. The interaction of diffraction and spatial confinement in a multimode fiber leads to the formation of multiple co-propagating spatial modes, each with distinct dispersive properties, such as different phase and group velocities, second- and higher-order dispersions. The dispersion of these spatial

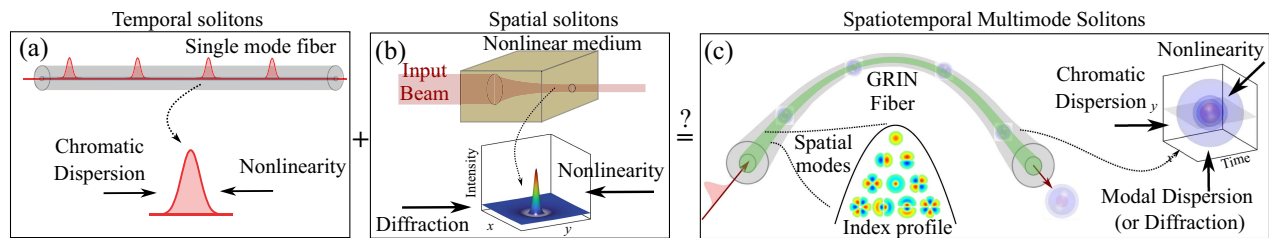


**Fig. 1.** (a) Temporal solitons propagate within a single-mode fiber, forming due to the equilibrium between chromatic dispersion induced temporal broadening and nonlinearity induced pulse compression. (b) Spatial solitons manifest in Kerr nonlinear media, shaping a beam with a consistent beam waist as it travels, emerging from the interplay of spatial diffraction induced beam divergence and nonlinear self-focusing. (c) Spatiotemporal MMS propagate in graded-index multimode fibers, where the interaction between beam diffraction and fiber confinement creates spatial multimodal beams. MMS formation is more complex, necessitating a balance not only between chromatic dispersion broadening and nonlinear pulse compression, but also a balance between nonlinear beam trapping and modal walk-off due to the disparate group velocities of the fiber modes.

modes can be balanced by Kerr nonlinearity, causing the modes to become locked together in time. As a result, the multimode field propagates as a single, shape-preserving “ball” of energy in both space and time. These equilibrium states are known as multimode solitons (MMSs) [see Fig. 1(c)].

There are two major motivations for studying MMSs: 1) the intrinsic scientific interest in propagation-invariant waves, and 2) the potential to interpret complex phenomena, especially in more than one dimension, through soliton dynamics. Interpreting instabilities, pulse formation, supercontinuum generation, and other phenomena in one dimension using the soliton concept in the frame of the 1D NLSE has proven to be highly beneficial. Similarly, MMSs could provide a foundation for understanding multidimensional nonlinear phenomena. While the community has demonstrated several instances where this approach is effective, further research is needed before we can definitively state that “a field can be described as a superposition of solitons and dispersive waves,” as is often done for one-dimensional systems.

Following early work [27,28,33–35], MMSs have gained increasing attention, particularly in graded-index (GRIN) multimode fibers (GIMFs), which minimize intermodal dispersion and reduce modal walk-off time, thus facilitating the formation of an MMS. Many experiments involving multimode solitons in MMFs have explored phenomena such as soliton fission [36], walk-off solitons [37], singlemode spatiotemporal soliton attractors [38], collisions [39], dispersive radiation sideband generation [40,41], and MMS formation in multimode step-index fibers (SIMFs) [42,43]. The development of MMS in conservative systems has spurred interest in the study of the emergence of MMS in dissipative systems, such as spatiotemporal mode-locked lasers [44–46] and different multimode cavity configurations [47,48]. Furthermore, GIMFs have emerged as valuable testbeds for highly multimode systems [21], enabling the observation of a variety of phenomena such as beam self-cleaning [49], thermalization of optical waves [50–52], and supercontinuum generation [53].

This review paper focuses on recent theoretical and experimental advancements in MMSs in conservative systems, with a primary focus on MMFs. We begin by introducing the foundational concepts of MMF and MMS, elucidating the phenomena associated with MMS in relation to the MMF

properties in Section 2. Many of these phenomena, such as modal walk-off and MMS formation, can be effectively modeled by the generalized coupled mode equation, with simple examples provided in Section 3. Next, we review analytic approaches to MMS using the two-coupled mode equations in Section 4, and discuss extensions to the 3D+1 spatiotemporal nonlinear Schrödinger equation (NLSE) in Section 5. To enhance understanding, the comprehensive 3D+1 model is simplified to a reduced 1D+1 NLSE representation in Section 6, which is highly efficient for studying the self-imaging-effect-induced phenomena in GIMFs. In Section 7, we introduce an innovative Gaussian quadrature approach tailored for numerical simulations of the generalized NLSE, potentially improving computational efficiency. In Section 8, we examine the propagation regime in space-division multiplexed (SDM) optical communication systems designed with MMFs, discussing the model using a generalized Jones formalism. This model highlights the impact of linear coupling effects, primarily due to manufacturing imperfections and environmental perturbations. Finally, in Section 9, we focus on the relevant experimental studies involving the MMS phenomena.

In essence, this review endeavors to offer a comprehensive overview of MMS, from MMF properties, their theoretical analysis, innovative numerical approaches, the impact of random linear coupling, and practical experiments. By exploring these domains, the paper aims to enrich understanding and acknowledgment of the significance of MMS, thus driving progress in MMS research and technology.

## 2. MMF EIGENMODES AND MODAL DISPERSIONS

In this section, we first focus on the spatial eigenmodes of two types of MMFs: the step-index multimode fiber (SIMF) and the GIMF. We discuss their key properties related to the MMS, setting the stage for understanding their impact on soliton formation. Subsequently, we introduce the generalized multimode NLSE (GMMNLSE), which is relevant for describing a broad variety of MMFs with identifiable eigenmodes. We provide concise examples, ranging from the propagation of linear multimode pulse fields to the formation of MMS, the Raman-induced MMS self-frequency shift, MMS fissions,

and MMS collisions. These examples serve to effectively illustrate the discussed concepts, thereby laying a solid foundation for analytical and experimental studies.

### A. Overview of the Relationship between MMF and MMS

MMFs are capable of supporting many guided modes simultaneously. To gain a comprehensive understanding of MMFs, several key concepts must be grasped, as depicted in Fig. 2.

- **Eigenmodes.** Eigenmodes represent distinct transverse profiles of the spatial modes that can propagate within an MMF, illustrating how optical fields distribute across the fiber's cross-section. Calculation of the modal areas and their overlap is necessary to define the modal nonlinear coefficients and the strength of nonlinear mode coupling.

- **Eigenvalues ( $n_{\text{eff}}$ ).** The modal eigenvalues, denoted as  $n_{\text{eff}}$  and representing a mode's effective refractive index, quantify the increase in the propagation constant  $\beta = n_{\text{eff}}k_0$  at a specific wavelength, when compared with the vacuum wave number  $k_0$ . Since  $n_{\text{eff}}$  varies with frequency, for each mode of index  $p$  the different derivatives  $\beta_n^{(p)}(\omega) = \frac{\partial^n \beta^{(p)}}{\partial \omega^n}$  with respect to frequency (or wavelength) directly affect the properties of guided modes such as modal pulse broadening, modal group velocity, and mode beating.

- **$\chi^{(3)}$  nonlinearity.** The nonlinearity of an MMF results from the complex third-order optical susceptibility of the fiber's material (typically silica). There are two main categories of cubic nonlinear effects in fibers according to their response times: the virtually instantaneous Kerr effect, and the delayed nonlinear Raman and Brillouin scattering. As the light intensity increases, the Kerr effect may compensate for both intramodal pulse broadening and intermodal walk-off, leading to the MMS formation.

Subsequent subsections will discuss each of these concepts in more detail, providing a comprehensive understanding of MMF modes and their significance in MMS formation.

### B. MMF Spatial Eigenmodes

Light travels longitudinally in fibers, while remaining confined transversely to the core through total internal reflection resulting from the refractive index difference between the core and the cladding. This confinement establishes boundary conditions, leading to specific guided propagation modes that

depend on the fiber's transverse refractive index profile. The diversity of index profiles gives rise to various types of MMF, each characterized by spatial modes with distinct transverse beam profiles and eigenvalues. This subsection introduces the eigenmodes by using the specific examples of the SIMF and GIMF with identical core sizes.

In the case of a SIMF, the fiber's core has a larger refractive index  $n_{\text{co}}$  and is surrounded by a cladding with the index  $n_{\text{cl}}$  such that  $\Delta n = n_{\text{co}} - n_{\text{cl}} > 0$ . The SIMF's transverse refractive index profile is given by

$$n(x, y, \lambda) = \begin{cases} n_{\text{cl}}(\lambda) + \Delta n, & \text{if } x^2 + y^2 < R^2, \\ n_{\text{cl}}(\lambda), & \text{otherwise,} \end{cases} \quad (1)$$

where  $R$  denotes the core's radius. The refractive index of the fiber not only varies with the wavelength  $\lambda$  but also with the spatial coordinates  $(x, y)$ . In the context of silica fibers, the wavelength dependence of  $n_{\text{cl}}(\lambda)$  is commonly characterized using a Sellmeier equation [54], which can provide the refractive index changes over a wide wavelength range. We use the following values for the SIMF parameters: the core's radius  $R = 25 \mu\text{m}$  and a refractive index difference  $\Delta n = 0.0137$  compared to the cladding. The index profile  $n(x, y = 0, \lambda = 1.45 \mu\text{m})$  is shown by a black curve in Fig. 3(a).

Based on the fiber's index profile, we calculate the first 15 eigenmodes  $F(x, y, \lambda_s)_{m,l}$  at  $\lambda_s = 1.45 \mu\text{m}$  by employing the semivectorial finite-difference method [55]. These modes  $F(x, y, \lambda_s)_{m,l}$ , designated as linearly polarized (LP) with indices  $m$  (azimuthal) and  $l$  (radial), are displayed on the top in Fig. 3. Degenerate modes sharing the same  $m, l$  values are denoted by a, b. To simplify references to these modes, we assign a single-mode index  $p$ . For instance,  $F_{11a}$  and  $F_{11b}$  correspond to modes  $p = 2$  and  $p = 3$ , respectively.

To illustrate the relationship among eigenmodes, eigenvalues, and refractive index distribution, we plot the mode profiles  $F_p(x, y = 0)$  in Fig. 3(a) for three distinct radial modes ( $p = 1, 6, 15$ ), each shifted vertically by its corresponding mode eigenvalue, using blue and green curves at wavelengths of  $1.55 \mu\text{m}$  and  $1.70 \mu\text{m}$ , respectively. The corresponding modal eigenvalues at three wavelengths are shown in Fig. 3(b). These modes primarily reside within the core of the fiber. Remarkably, higher-order modes, or those with longer

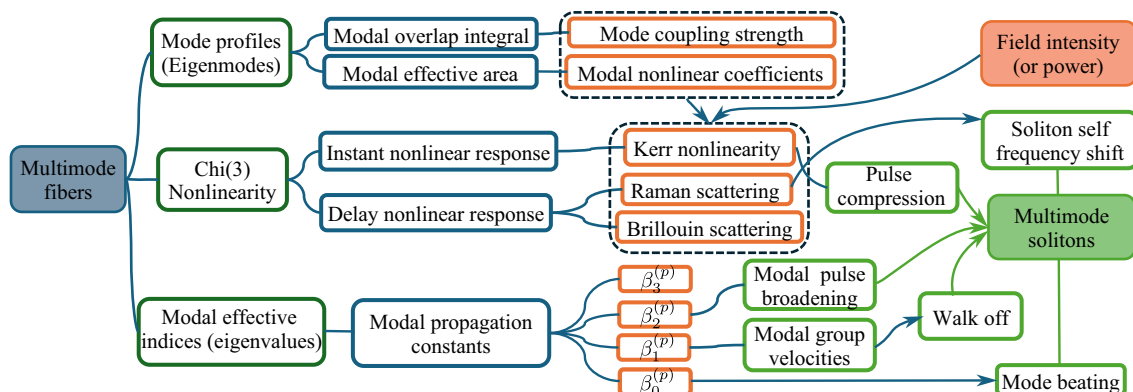


**Fig. 2.** Overview of the relationships between the fundamental properties of MMFs and the key physical phenomena leading to the formation of an MMS.

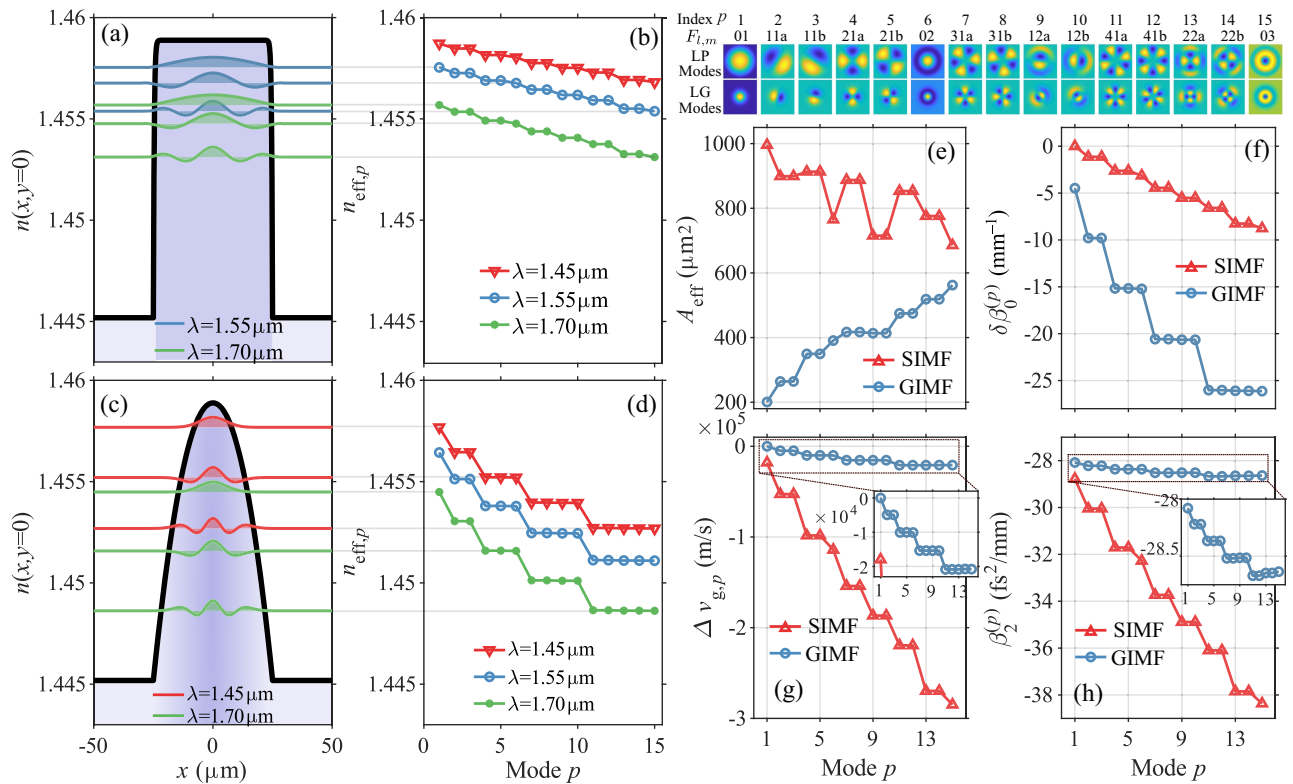


**Fig. 3.** Refractive index profiles  $n(x, y = 0)$  (black solid line) of SIMF in (a), (b) and GIMF in (c), (d) and their corresponding eigenmode profiles  $F_p(x, y = 0)$  ( $p = 1, 6, 15$ ), modal effective indices  $n_{\text{eff},p}$  ( $p = 1, \dots, 15$ ), (e)–(h) Mode dispersion comparison between the SIMF and the GIMF with the same core radius of  $50 \mu\text{m}$  at  $1.45 \mu\text{m}$ , for (e) mode effective areas, (f) relative zero-order mode dispersion  $\delta\beta_0^{(p)} = \beta_0^{(p)} - \beta_0^{(1)}$ , (g) relative group velocity  $\Delta v_{g,p} = 1/\beta_1^{(p)} - 1/\beta_1^{(1)}$ , (h) second-order dispersion  $\beta_2^{(p)}$ . The fiber radius for the two fibers is  $R = 25 \mu\text{m}$ .

wavelengths, have a smaller effective index, indicating reduced confinement for them. As a result, the number of supported modes varies with wavelength. While MMFs can accommodate more modes at shorter wavelengths, they may support only a single mode at much longer wavelengths, thereby classifying them as singlemode fibers when the wavelength surpasses a certain threshold value (cutoff wavelength).

The shape of the refractive index profile of an MMF influences its guided modes. This is illustrated in Fig. 3(c) using the example of a GIMF with a core radius  $R = 25 \mu\text{m}$ . The GIMF's refractive index follows a parabolic distribution:

$$n(x, y, \lambda) = \begin{cases} n_{\text{cl}}(\lambda) + \Delta n \left( 1 - \frac{x^2 + y^2}{R^2} \right), & \text{if } x^2 + y^2 < R^2 \\ n_{\text{cl}}(\lambda), & \text{otherwise} \end{cases} \quad (2)$$

This distribution leads to eigenmodes resembling Laguerre-Gaussian (LG) modes. The refractive index  $n(x, y = 0, \lambda = 1.45 \mu\text{m})$  and LG mode profiles  $F_p(x, y = 0)$  are depicted in Fig. 3(c) for modes  $p = 1, 6, 15$  (the first three radial modes:  $\text{LG}_{01}$ ,  $\text{LG}_{02}$ ,  $\text{LG}_{03}$ ) at wavelengths of  $1.45 \mu\text{m}$  and  $1.70 \mu\text{m}$  using red and green curves. While mode profiles for GIMF and SIMF fibers exhibit significant similarities, it is worth noting that the mode areas of a GIMF are considerably smaller than those of a SIMF. To rigorously characterize the influence of mode profiles, it is essential to define the effective areas of the MMF modes.

### 1. Effective Mode Areas

The mode's area significantly influences MMF dynamics in the nonlinear (high-power) regimes. This is due to the fact that, for an identical optical power, modes with smaller spatial dimensions lead to elevated field intensities (optical power per unit area), thus inducing more pronounced refractive index changes through the Kerr effect. In the presence of nonlinear effects, the mode's effective area (MEA) is introduced as follows [56]:

$$A_{\text{eff}}^{(p)} = \frac{\left( \iint |F_p(x, y)|^2 dx dy \right)^2}{\iint |F_p(x, y)|^4 dx dy}, \quad (3)$$

where the mode profiles are both normalized and mutually orthogonal:

$$\iint_{-\infty}^{\infty} F_n(x, y) F_m(x, y) dx dy = \delta_{nm}. \quad (4)$$

### 2. Modal Nonlinear Coefficients

The modal effective area (MEA) is not enough to quantify the strength of nonlinear effects in an MMF because the nonlinear interaction among the modes also depends on the wavelength of incident light and fiber material. Therefore, one needs to introduce the modal nonlinear coefficient (MNC), which can be calculated as

$$\gamma^{(p)} = \frac{2\pi n_2}{\lambda A_{\text{eff}}^{(p)}}, \quad (5)$$

where  $n_2$  is the nonlinear refractive index of the MMF that produces a change in the refractive index,  $\Delta n = n_2 I$ , which depends linearly on the local intensity  $I$  of light and has the dimensions of  $\text{m}^2/\text{W}$ . Different effective mode areas in an MMF lead to different MNCs for its various modes.

### 3. Modal Nonlinear Lengths

The modal nonlinear length (MNL) is the characteristic length scale over which significant nonlinear optical effects occur in an optical fiber. It provides a measure of the distance along the fiber at which a light pulse is significantly affected by nonlinear interactions. The nonlinear length of a mode is defined as [56]

$$L_N^{(p)} = [\gamma^{(p)} P_0^{(p)}]^{-1}, \quad (6)$$

where  $P_0^{(p)}$  is the input peak power of mode  $p$ . This form indicates that a higher input power or a larger MNC leads to a shorter nonlinear length.

It is worth noting that the nonlinear length of a mode is proportional to its MEA, indicating that the MEA is a key parameter for each mode and serves as a critical parameter for distinguishing nonlinear performance across various modes of an MMF.

### 4. Nonlinear Responses

Optical pulses propagating inside an MMF with high peak powers may be affected by several nonlinear effects. We briefly introduce the effects associated with the third-order nonlinear optical susceptibility ( $\chi^{(3)}$ ) for which the nonlinear polarization is proportional to the third power of the electric field. Effects associated with the  $\chi^{(3)}$  nonlinearity can be grouped into two main categories according to their response time, which can be either very short or delayed in time (typically  $<1$  ps). The former encompasses the well-known Kerr effect, which produces a nearly instantaneous change in the refractive index proportional to pulse intensity. This change alters the propagation constants of all excited modes and gives rise to nonlinear phenomena such as self-phase modulation (SPM), cross-phase modulation (XPM), and four-wave mixing (FWM).

A delayed nonlinear response implies that the nonlinear polarization not only depends on the electric field at the current time, but also on the field values at earlier times. This delay is attributed to light-induced molecular vibrations involving either optical phonons (Raman scattering) or acoustic phonons (Brillouin scattering). We refer to Ref. [56] for further details. Only Raman scattering is relevant for short pulses that are of interest in this review. As a result of Raman scattering, a longer-wavelength pulse, known as the Stokes pulse, undergoes amplification in the presence of a shorter-wavelength (pump) pulse. In silica fibers, maximum gain occurs for a relative frequency shift of about 13 THz (or 100 nm) from the pump. As the intensity of the Stokes pulse increases, it can serve as the pump and generate another pulse at a longer wavelength through a cascaded Raman process, thus potentially producing multiple pulses from a single pump pulse.

### 5. Raman-Induced Self-Frequency Shift

The Raman gain affects ultrashort pulses (width  $<1$  ps) in a different way through a process called intrapulse Raman scattering [56]. The spectrum of such pulses is so wide that its low-frequency components can be amplified by the high-frequency

components of the same pulse. Consequently, the entire spectrum of a short pulse continuously shifts towards longer wavelengths as it propagates along the fiber. This effect is particularly strong for solitons and is often referred to as the soliton self-frequency shift (SSFS). As we discuss later, it also occurs for an MMS forming inside an MMF.

### C. Modal Dispersion

Let us introduce modal dispersion, a key property of MMFs, which is associated with the eigenvalues corresponding to different guided modes. These eigenvalues are crucial, as they directly influence the propagation of optical pulses through different guided modes. We initiate our discussion by focusing on the frequency dependence of eigenvalues of the modes, and obtain the associated modal dispersion properties. By considering different orders of modal dispersion for both GIMFs and SIMFs, we are able to find several specific properties of GIMFs. GIMFs exhibit a mode-beating distance that is nearly wavelength independent, a reduced chromatic-dispersion-induced pulse broadening, and a minimal intermodal walk-off. Such attributes render GIMFs a fertile ground for observing many intriguing phenomena, including periodic self-imaging [57], formation of multimode solitons [37,38], and collisions of such solitons [39].

The eigenvalues of MMF modes are the effective modal indices  $n_p(\lambda)$ . They quantify the change in a mode's propagation constant induced by the fiber's refractive index profile. As shown in Figs. 3(b) and 3(d),  $n_p(\lambda)$  for SIMFs and GIMFs decreases with the mode order  $p$  and wavelength  $\lambda$ , indicating that a weaker waveguide confinement occurs for HOMs or at longer wavelengths.

To discuss modal dispersion, we consider the frequency dependence of the propagation constant  $\beta^{(p)}(\omega)$  for mode  $p$ :

$$\beta^{(p)}(\omega) = \frac{\omega}{c} n_p(\omega). \quad (7)$$

Different derivative orders of  $\beta^{(p)}$  with respect to frequency  $\omega$  provide us with several dispersion parameters,

$$\beta_n^{(p)}(\omega) = \frac{\partial^n \beta^{(p)}}{\partial \omega^n}, \quad (8)$$

which play a crucial role when short pulses propagate inside an MMF. Utilizing these coefficients, we can elucidate the influence of dispersion on various physical phenomena in MMFs.

#### 1. Modal Propagation Constants

The propagation constant (zeroth-order dispersion)  $\beta_0^{(p)}(\omega)$  in Eq. (8) quantifies the rate of phase change for mode  $p$  with propagation. Figure 3(f) compares for SIMF and GIMF the phase difference,  $\delta\beta_0^{(p)} = \beta_0^{(p)} - \beta_{0,\text{SIMF}}^{(1)}$ , between the propagation constant of mode  $p$  and that of the fundamental mode of the SIMF. In the case of a GIMF,  $\beta_0^{(p)}$  exhibits a distinct step-wise decrease as the mode order  $p$  increases across different degenerate mode groups.

Changes in the modal propagation constant  $\beta_0^{(p)}$  with  $p$  play a crucial role in MMFs and lead to phenomena such as multi-mode interference or mode beating. This beating rate stems from the difference of  $\beta_0$  for any two modes and can be used to define the mode-beating length (MBL) as

$$L_B^{(p,q)} = 2\pi/|\beta_0^{(p)} - \beta_0^{(q)}|. \quad (9)$$

Mode beating is particularly pronounced in GIMFs, where the phase-rate differences between adjacent mode groups are nearly identical. For example, as shown in Fig. 3(f), the modes 1, 6, and 15 satisfy the relation  $\beta_0^{(1)} - \beta_0^{(6)} = \beta_0^{(6)} - \beta_0^{(15)}$ . This feature enhances the mode-beating process, which involves multiple high-order modes. Whenever an optical beam excites multiple modes of a GIMF, the total intensity, obtained by adding the contributions of all modes [see Eq. (25)], exhibits a periodic evolution (the self-imaging effect). The period of mode beating is determined by the constant difference in propagation constants between adjacent groups of modes.

Interestingly, for femtosecond pulses, the intensity at points of maximum beam compression may become so high that it induces multiphoton absorption or ionization [58]. In turn, a visible photoluminescence is generated, which scatters out of the fiber as a series of bright spots, providing an experimental verification of the self-imaging phenomenon [57]. The self-imaging period does not depend on power and is equal to the beating length of different radial modes:

$$Z_{SI} = 2\pi/|\beta_0^{(6)} - \beta_0^{(1)}|. \quad (10)$$

By using the data plotted in Fig. 3(f), we calculate the self-imaging distance to be  $Z_{SI} \approx 2\pi/(11 \times 10^{-3} \text{ m}^{-1}) \approx 0.58 \text{ mm}$ , which closely matches the experimentally observed values [57].

A remarkable property of a GIMF is its near-constant MBL for different wavelengths. To elucidate this feature, Fig. 4(a) shows the wavelength dependence of  $L_B^{(1,6)}$  for modes  $p = 1$  and  $p = 6$  for both the GIMF and the SIMF. Remarkably, as the wavelength shifts from 1.1  $\mu\text{m}$  to 1.8  $\mu\text{m}$ ,  $L_B$  in SIMF varies from 2.8 mm to 1.7 mm but its value for the GIMF remains fixed at 0.58 mm.

From a different perspective, the self-imaging period  $Z_{SI}$  in a GIMF depends on the core radius  $R$  and the refractive index difference as  $Z_{SI} \approx \pi R/\sqrt{\Delta}$  [57], where  $\Delta = (n_{co}^2 - n_{cl}^2)/n_{co}^2$  is the relative index difference between the core  $n_{co}$  and the cladding  $n_{cl}$ . Typically, the refractive index varies with wavelength, which is a common characteristic of optical materials. However, if  $\Delta$  undergoes minimal changes across a range of wavelengths, the self-imaging period remains nearly constant. This feature implies that the self-imaging phenomenon in GIMFs exhibits a remarkable wavelength stability.

When non-radial modes are excited in a GIMF by launching a beam off-set from the core's center, the beam's shape exhibits transverse oscillations with distance. This process doubles the spatial period of self-imaging, owing to the beating between radial and non-radial modes. The resulting self-imaging period results from the propagation constant difference between two such modes and is given by  $Z'_{SI} = 2\pi/(\beta_0^{(2)} - \beta_0^{(1)}) = 1.16 \text{ mm}$  [see the blue curve in Fig. 4(a)].

The evolution of periodic mode beating leads to collective intensity oscillations, which in turn facilitates the emergence of spectral sidebands. This phenomenon is associated with resonant dispersive radiation in regions of anomalous dispersion [41,59] and with a so-called geometric parametric instability (GPI) in the region of normal dispersion [60]. The frequencies of the GPI-induced resonant spectral peaks adjacent to the pump frequency follow the relation

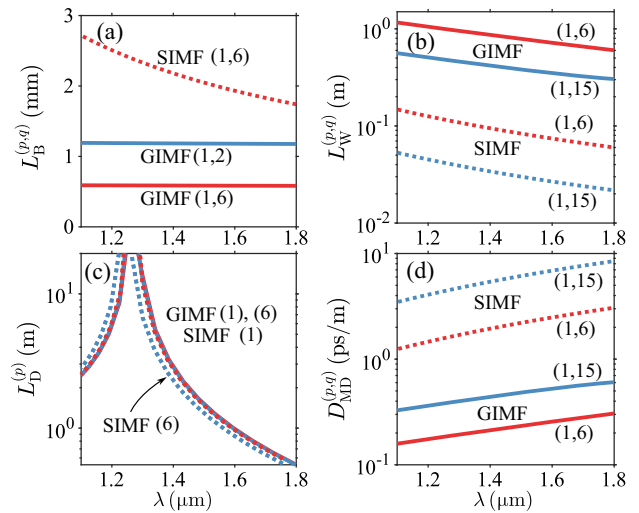


**Fig. 4.** Characteristic lengths of GIMFs and SIMFs at different wavelengths: (a) mode beating length  $L_B^{(p,q)}$ ; (b) modal walk-off length  $L_W^{(p,q)}$ ; (c) dispersion length  $L_D^{(p)}$ . In (d) we show the differential mode delay  $D_{MD}^{(p,q)}$  for modes  $p$  and  $q$ , for an input pulse temporal duration  $T_0 = 110 \text{ fs}$  (FWHM: 184 fs). The significance of each length scale in (a)–(c) becomes apparent when the pulse propagation distance exceeds these characteristic lengths, indicating that the corresponding effect has a significant influence.  $D_{MD}^{(p,q)}$  detailed in (d) quantifies the temporal separation (ps) between two modes per unit of propagation distance (m).

$$f_b = \pm \frac{\sqrt{b}}{2\pi} \sqrt{\frac{2\pi}{Z_{SI}\beta_2^{(1)}}}, \quad b = 1, 2, 3, \dots \quad (11)$$

## 2. Intermodal Dispersion

The group velocity of a multimode optical pulse depends not only on the optical frequency (chromatic dispersion) but also on its constituent modes. For mode  $p$  at wavelength  $\lambda$ , the first-order term  $\beta_1^{(p)}(\lambda)$  in Eq. (8) is inversely proportional to the group velocity

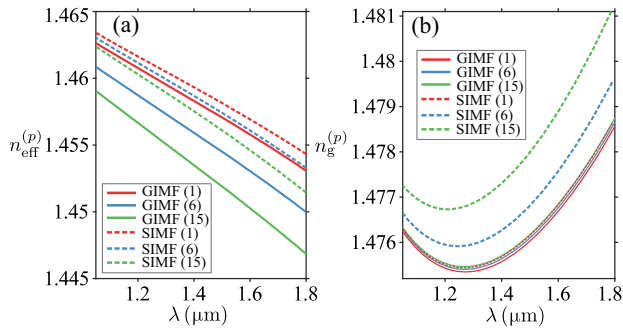
$$v_g^{(p)}(\lambda) = 1/\beta_1^{(p)}(\lambda). \quad (12)$$

Figure 3(g) shows the relative group velocity  $\Delta v_g^{(p)} = v_g^{(p)} - v_{g,GIMF}^{(p)}$  between a mode of order  $p$  of either a GIMF or a SIMF, and the fundamental mode of a GIMF at  $\lambda = 1450 \text{ nm}$ . We may observe that, when compared to SIMF, modes of GIMF propagate faster and exhibit smaller group velocity differences. Additionally, for both fibers the group velocity of LOMs is larger than that of HOMs.

It may appear surprising that LOMs have higher group velocities than HOMs, since the effective index decreases as the mode number grows larger [see Figs. 3(b) and 3(d)]. Therefore, the phase velocity of LOMs is smaller than that of HOMs. However, the group velocity has an inverse dependence on the modal group index, which includes the effects of dispersion and is defined as

$$n_g^{(p)}(\omega) = n_{eff}^{(p)} + \omega \frac{d}{d\omega} n_{eff}^{(p)}. \quad (13)$$

For a more detailed comparison, we illustrate in Fig. 5 the wavelength dependence of both the modal effective index  $n_{eff}^{(p)}$



**Fig. 5.** Modal effective index  $n_{\text{eff}}^{(p)}(\lambda)$  in (a) and modal group index  $n_g^{(p)}(\lambda)$  in (b) as functions of wavelength for mode  $p = 1, 6, 15$  in both GIMF and SIMF.

and the modal group index  $n_g^{(p)}$  for modes  $p = 1, 6, 15$  for both GIMF and SIMF. As can be seen, contrary to the effective index, the modal group index grows larger with mode number for both types of fibers. Moreover, the modal effective index decreases monotonically with increasing wavelength. In contrast, the modal group index reaches its minimum value near the zero-dispersion wavelength, where the largest group velocity is reached. In regions of anomalous dispersion, an increasing  $n_{\text{eff}}$  for mode  $p$  means a decrease in the group velocity of that mode as its wavelength grows larger.

The differential mode delay (DMD) quantifies the temporal delay between modes per unit distance; it is defined as

$$D_{\text{MD}}^{(p,q)} = \beta_1^{(p)} - \beta_1^{(q)}. \quad (14)$$

In Fig. 4(d) we show the wavelength dependence of  $D_{\text{MD}}^{(p,q)}(\lambda)$ , for the mode pairs (1, 6) and (1, 15) for both GIMF and SIMF. For both types of fiber, the DMD increases with wavelength. In addition, an increase in the relative mode number difference leads to larger values of  $D_{\text{MD}}^{(p,q)}(\lambda)$ . Consequently, the formation of MMS is much more difficult for modes with large DMDs, when compared with MMS composed of adjacent modes.

For GIMFs, the DMD values of  $<1$  ps are an order of magnitude smaller than those for SIMFs. For example, at a wavelength of  $1.45 \mu\text{m}$  the temporal delay associated with modal dispersion is  $D_{\text{MD}}^{(1,6)} \approx 0.22$  ps/m for a GIMF but approximately  $2.4$  ps/m for a SIMF. Utilizing  $D_{\text{MD}}^{(p,q)}(\lambda)$  allows for a rough estimate of the propagation delay between modes in the linear regime. For instance, when a pulse travels  $5$  km inside a GIMF, its relative delay is approximately  $1.1$  ns for two neighboring modes. This estimate agrees with experimental findings, as found in Ref. [61].

The walk-off distance for pulses carried by different modes depends not only on the relative group velocities of these modes but also on pulse duration. Longer pulses have less pronounced walk-off compared to shorter pulses. For a pulse of duration  $T_0$ , the walk-off distance between modes  $p$  and  $q$  is defined as

$$L_{\text{W}}^{(p,q)} = T_0 / |\beta_1^{(p)} - \beta_1^{(q)}|. \quad (15)$$

Here  $L_{\text{W}}^{(p,q)}$  stands for the distance over which two pulses separate in time by an amount equal to their temporal width.

A longer walk-off length implies more interaction time due to their temporal overlap during propagation, while a shorter length suggests significant temporal separation over a shorter distance.

Low-order modes (LOMs) travel faster compared to high-order modes (HOMs), e.g.,  $\beta_1^{(1)}(\lambda_1) < \beta_1^{(6)}(\lambda_1)$  at any given wavelength. Whenever an MMS is formed by trapping different modes via the Kerr nonlinearity, the resulting group velocity of the MMS will be intrinsically linked to its modal composition. Therefore, one may expect that an MMS composed of HOMs will propagate more slowly than an MMS composed of LOMs.

The binding mechanism for different modes composing an MMS is that the Kerr nonlinearity induces a spectral blue shift for HOMs and a red shift for LOMs. This is due to the fact that modal group velocities decrease as wavelength increases in the case of anomalous dispersion, i.e.,  $\beta_1^{(p)}(\lambda_1) < \beta_1^{(p)}(\lambda_2)$  for  $\lambda_1 > \lambda_2$ . Consequently, the red-shifted LOMs decelerate while the blue-shifted HOMs accelerate, gradually approaching an equilibrium point where group velocities become balanced across all modes. An illustrative example of this phenomenon can be found in Fig. 7, as detailed in Section 2.B.1.

As previously mentioned, the Raman effect induces a progressive red shift of the soliton, which decreases its group velocity. In GIMFs, the Raman effect also contributes to the MMS formation, since it reduces the speed mismatch between the fast LOMs (which have higher nonlinear coefficients and undergo the largest SSFS) and the slow HOMs. On the other hand, when two multimode Raman solitons with distinct modal compositions are generated during the fission of a single MMS, their different group velocities may lead to collisions between them as outlined in Ref. [39]. This scenario is elucidated by the example presented in Fig. 11(d) in Section 2.B.4.

### 3. Chromatic Dispersion

Chromatic or group-velocity dispersion (GVD) characterizes the dispersive broadening of optical pulses within each mode of an MMF. As a consequence of material and waveguide dispersion, different frequency components within the pulse in a given mode travel at different speeds, resulting in pulse spreading in time upon its propagation. The GVD is governed by the second-order term  $\beta_2^{(p)}(\omega)$  in Eq. (8). In standard silica optical fibers, there is a zero-dispersion wavelength (ZDW), close to  $1.3 \mu\text{m}$ , such that  $\beta_2^{(p)}(\omega) = 0$ . Consequently, optical pulses propagating near this wavelength are little affected by GVD, but the impact of higher-order dispersions on the pulses may become significant.

For a transform-limited (i.e., unchirped) Gaussian pulse with initial temporal width  $T_0$ , propagating in either the normal or anomalous dispersion regime, its temporal width increases with distance  $z$  as [56]  $T(z) = T_0[1 + (z|\beta_2^{(p)}|/T_0^2)^2]^{1/2}$ . It is useful to introduce a characteristic dispersion length for mode  $p$  as

$$L_{\text{D}}^{(p)} = T_0^2 / |\beta_2^{(p)}|. \quad (16)$$

Consequently, for a pulse carried by mode  $p$  the pulse broadening ratio,  $T/T_0 = [1 + z/L_{\text{D}}^{(p)}]^{1/2}$ , becomes significant as it travels a distance greater than  $L_{\text{D}}$ .

In Fig. 4(c), we plot  $L_D^{(p)}(\lambda)$  as a function of wavelength for both GIMF and SIMF. As can be seen, for wavelengths around the ZDW of 1.26  $\mu\text{m}$ ,  $L_D^{(p)}(\lambda)$  tends towards infinity because  $\beta_2^{(p)}(\omega) \approx 0$ . The ZDW corresponds to an inflection point for  $\beta_1^{(p)}(\omega)$ , and optical pulses propagate at their fastest speed at this wavelength when compared with other wavelengths. In the normal dispersion regime ( $\lambda < 1.3 \mu\text{m}$ ), the group velocity increases with wavelength; in the anomalous dispersion regime ( $\lambda > 1.3 \mu\text{m}$ ), the opposite happens.

The GVD is different for different guided modes in MMFs. This is depicted in Fig. 3(h), where the value of  $\beta_2^{(p)}(\omega)$  at 1.45  $\mu\text{m}$  is shown for both SIMF and GIMF. The GIMF has smaller GVD values and exhibits narrower gaps across its mode groups compared to the SIMF, as further illustrated by the dispersion lengths plotted in Fig. 4(c). Consequently, GIMFs are expected to produce much less temporal broadening compared to SIMFs, suggesting that a smaller input power will be necessary to form multimode solitons in GIMFs.

### D. Soliton Formation Conditions

By comparing the relevant characteristic lengths, we can find interesting conditions for the formation of solitons. For simplicity, here we focus on a fundamental soliton involving only one mode of an MMF. Similar to the case of singlemode fibers, a soliton involving only the mode  $p$  will have a hyperbolic secant profile:

$$A_p(t) = \sqrt{P_0^{(p)}} \operatorname{sech}(t/T_0), \quad (17)$$

where  $P_0^{(p)}$  and  $T_0$  are the peak power and duration of the soliton, respectively. From this, energy of this soliton is found to be

$$\mathcal{E}^{(p)} = \int_{-\infty}^{\infty} |A_p(t)|^2 dt = 2T_0 P_0^{(p)}. \quad (18)$$

By comparing the nonlinear length [Eq. (6)] with the dispersion length [Eq. (16)], we obtain the soliton order for mode  $p$  [56]:

$$N^{(p)} = \sqrt{\frac{L_N^{(p)}}{L_D^{(p)}}} = \sqrt{\frac{2\pi n_2 P_0^{(p)} T_0^2}{\lambda A_{\text{eff}}^{(p)} |\beta_2^{(p)}|}}. \quad (19)$$

For  $N^{(p)} < 1$ , dispersive effects dominate over the nonlinear effects, preventing the formation of a soliton. When  $N^{(p)} > 1$ , higher-order solitons may form, exhibiting a periodic evolution. A fundamental soliton is formed when  $N^{(p)} = 1$ . Given that both the effective mode area ( $A_{\text{eff}}^{(p)}$ ) and dispersion ( $\beta_2^{(p)}$ ) are different for different modes for an MMF, a soliton's peak power will also depend on  $p$ . By setting  $N^{(p)} = 1$ , we find the following relations for the peak power  $P_0^{(p)}$  and the energy of a soliton of duration  $T_0$ :

$$P_0^{(p)} = \frac{\lambda A_{\text{eff}}^{(p)} |\beta_2^{(p)}|}{2\pi n_2 T_0^2}, \quad (20)$$

$$\mathcal{E}^{(p)} = \frac{\lambda A_{\text{eff}}^{(p)} |\beta_2^{(p)}|}{\pi n_2 T_0}. \quad (21)$$

As the duration  $T_0$  varies,  $P_0^{(p)}$  and  $\mathcal{E}^{(p)}$  change as shown in Fig. 6(b) for the two types of fibers for the formation of solitons

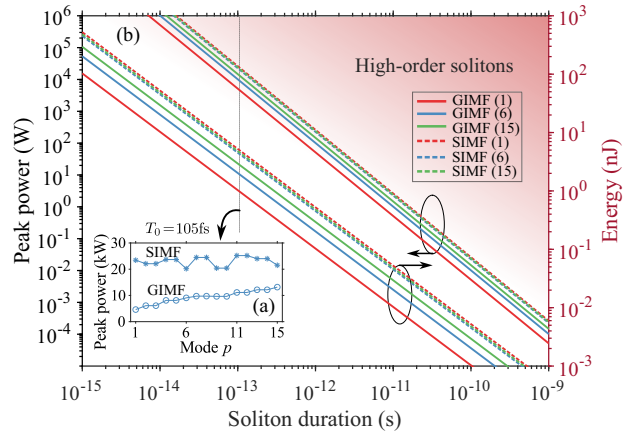


**Fig. 6.** (a) Peak power of a fundamental soliton carried by a mode with index  $p$  in SIMF and GIMF, respectively, for a 105 fs pulse duration. (b) Required peak powers and energies for forming a fundamental soliton of varying duration in mode  $p$  for SIMF and GIMF when  $\lambda = 1550 \text{ nm}$ . Fiber parameters are consistent with those in Fig. 3.

at  $\lambda = 1550 \text{ nm}$ . For nanosecond pulses, the peak power needed is in the milliwatt range (or picojoule energy). For picosecond pulses, it reaches kilowatt levels (or nanojoule energy). For femtosecond pulses, the soliton needs peak powers in the megawatt range and energies reaching microjoule levels.

The dependence of the peak power on the mode number is shown in Fig. 6(a) for  $T_0 = 105 \text{ fs}$ . The evolution of the required peak power closely matches the effective mode area in Fig. 3(e). Modes with larger effective mode areas require higher peak power (or energy) to form a soliton. The GIMF requires 4.6 kW peak power for mode 1 and 12 kW for mode 15, while the SIMF needs higher powers of around 22 kW for each mode.

The formation of an MMS inside an MMF requires compensation of temporal walk-off associated with different mode pairs. By equating the walk-off length  $L_W^{(p,q)}$  from Eq. (15) with the dispersion length in Eq. (16) and the nonlinear length in Eq. (6), we can determine the temporal duration of an MMS involving any two specific modes:

$$T_w^{(p,q)} = \frac{|\beta_2^{(p)}|}{|\beta_1^{(p)} - \beta_1^{(q)}|}. \quad (22)$$

Based on the dispersion parameters of the two fibers in Fig. 3,  $T_w^{(1,6)}$  of the first two radial modes is found to be 115 fs for a GIMF and 12 fs for a SIMF. Therefore, based on the walk-off compensation condition for forming an MMS, the duration and peak power for GIMF should be around 115 fs and 3.8 kW (see Section 2.B.1 where we provide numerical examples of MMS formation). Since  $\beta_1^{(p)}$  and  $\beta_2^{(p)}$  vary with wavelength [see Eqs. (7) and (8)], the values of  $T_w^{(p,q)}$  also change. As a result, the “walk-off” soliton duration will also depend on wavelength (see Fig. 32 in Ref. [37]). For a soliton with  $T_0 > T_w^{(1,6)}$ , walk-off compensation becomes more critical, but it may be compensated for higher-order MMS with larger peak powers. For example, observing MMS in a SIMF requires a peak power in the MW range (or energy  $\sim 100 \text{ nJ}$ ) [42].



In the case of a soliton propagating in the fundamental mode, by substituting the mode effective area  $A_{\text{eff}}^{(p)}$  with the beam area of the fundamental mode  $\pi R_0^2$  ( $R_0$  is the waist of the fundamental mode), one may rewrite the relation Eq. (21) between the soliton energy and duration as follows:

$$M_1 = \mathcal{E}^{(p)} T_0 = \frac{\lambda R_0^2 |\beta_2^{(1)}|}{n_2}. \quad (23)$$

For MMSs, this relation can be approximated by replacing the mode energy  $\mathcal{E}^{(p)}$  with the total energy  $\mathcal{E}$ , the mode effective area  $A_{\text{eff}}^{(p)}$  with the beam area  $\pi R_g^2$  ( $R_g$  is the beam waist) in an MMF, and the second-order dispersion  $\beta_2^{(p)}$  with that of the fundamental mode  $\beta_2 = \beta_2^{(1)}$  (supposing that the difference between chromatic dispersion of different modes can be neglected). Thus, the condition for the existence of an MMS can be expressed in terms of the beam size, pulse energy, and duration, as follows [62]:

$$M \equiv \mathcal{E} T_0 = \frac{\lambda R_g^2 |\beta_2|}{n_2} > M_1. \quad (24)$$

As we shall discuss in Section 9, the experimental results have indeed demonstrated the validity of such a relationship (see Fig. 31 in Section 9).

### E. Insights into the Relationship between MMS and MEA

Building on these foundational concepts, a thorough comparison of SIMF and GIMF can yield profound insights, facilitating a deeper understanding of MMS dynamics in multimode fibers.

An important consideration is that even when two pulses have identical durations and energies (or peak powers), their nonlinear lengths in the same MMF can differ vastly if their modal compositions are not the same. This suggests that the mode distribution of a pulse plays a crucial role in determining the nonlinear dynamics inside MMFs. For the same power and wavelength, the nonlinear length [Eq. (6)] of any mode is proportional to its MEA [Eq. (3)]. This feature indicates that modes with a smaller MEA have larger nonlinear coefficients [Eq. (5)] and they can excite a larger nonlinearity for the same given field power.

The MEA  $A_{\text{eff}}^{(p)}$  in a GIMF increases with the mode order, while the MEA in a SIMF decreases, as seen in Fig. 3(e). This suggests that, for the same peak power, nonlinear effects may preferentially affect LOMs in GIMFs and HOMs in SIMFs, respectively. As an example, LOMs in a GIMF may initially compensate for their dispersion-induced pulse broadening via the Kerr effect, leading to the formation of an MMS composed by these modes [38].

Conversely, SIMFs are more likely to favor the formation of an MMS composed of HOMs, because of their smaller MEAs [see Fig. 3(e)] and higher MNCs. This is the reason that HOM Raman solitons are preferentially observed in SIMFs [42], while the Raman-beam cleanup is typically observed in GIMFs, rather than SIMFs [63]. With this insight, we can also understand Ref. [43], where a lower input-energy threshold was observed for generating a Raman MMS when the input beam was offset from the core's center to enhance the excitation of

HOMs of the fiber, compared to the case of on-center beam's coupling (see Fig. 36 in Section 9.F).

In general, linear LOMs propagate faster than HOMs at the same wavelength, due to their larger group indices [see Fig. 5(b)]. In GIMFs, the Raman effect can initially cause a stronger red-shift for LOM components in individual pulses, because of their relatively higher nonlinear coefficients compared with HOMs. This red-shift decreases the speed of pulses in the LOMs [see the explanation of  $\beta_1^{(p)}(\lambda)$  in Section 2.C], thereby minimizing the group-velocity mismatch between LOMs and HOMs and facilitating the formation of an MMS.

Furthermore, for an MMS in GIMFs, the pulse in the fundamental mode is red-shifted the most, and HOMs with shorter wavelengths serve as pumps, thus facilitating a substantial energy transfer from HOMs to the fundamental mode via the Raman effect. This explains why a significant Raman beam clean-up is observed, as shown in Ref. [38]. This phenomenon is harder to occur in SIMFs because their fundamental mode does not have the largest nonlinear parameter.

The mode size increases in all MMFs as wavelength increases, which in turn decreases the MNCs. This feature potentially contributes to the observed decrease in the rate of red shift (SSFS) of a Raman MMS as it propagates over longer distances. Furthermore, at higher wavelengths the number of modes within an MMF diminishes, especially affecting HOMs, which lose their confinement as wavelength increases.

The nonlinear coupling among the modes of an MMF depends on the overlap of their mode profiles. Generally speaking, nonlinear coupling between two radial modes ( $l = 0$ ) tends to be stronger than that between a radial and a non-radial mode. Furthermore, within the same degenerate group, nonlinear coupling is stronger when compared with the coupling between two non-degenerate modes.

During mode competition within an MMF, modes with a larger MNC are more likely to dominate the nonlinear dynamics. This may partially explain the occurrence of self-cleaning observed in GIMFs [49]. It can also explain the observation of speckled patterns in SIMFs, which is indicative of the dominance of HOMs in SIMFs.

## 3. COUPLED MODE EQUATIONS

### A. Coupled Multimode Nonlinear Schrödinger Equations

Building upon the insights gained from the preceding section, we discuss a widely used model for describing the evolution of optical pulses inside MMFs. As usual, the optical field of each pulse is written as the product of a rapidly evolving optical carrier  $\exp[i(\beta_0^{(0)} z - \omega_0 t)]$  and a slowly varying envelope  $E(x, y, z, t)$ , where  $\omega_0$  denotes the frequency at which the pulse's spectrum peaks. The envelope  $E(x, y, z, t)$  is normalized in a way that  $|E(x, y, z, t)|^2$  is expressed in units of  $\text{W}/\text{m}^2$ . This envelope can be expanded in terms of the eigenmodes of an MMF as follows:

$$E(x, y, z, t) = \sum_{p=1}^N F_p(x, y) A_p(z, t), \quad (25)$$

where  $F_p(x, y)$  are the previously introduced transverse mode profiles and the mode amplitudes  $A_p$  have units of  $\sqrt{\text{W}}$ .

The evolution of each modal component  $A_p$  along the propagation direction  $z$  is governed by the generalized multimode nonlinear Schrödinger equations (GMMNLSE) [64,65]

$$\frac{\partial A_p(z, t)}{\partial z} = \mathcal{D}\{A_p(z, t)\} + \mathcal{N}\{A_p(z, t)\}, \quad (26)$$

where the dispersion operator is given by

$$\mathcal{D} = i(\beta_0^{(p)} - \beta_0^{(1)}) - (\beta_1^{(p)} - \beta_1^{(1)}) \frac{\partial}{\partial t} + i \sum_{q \geq 2}^4 \frac{\beta_q^{(p)}}{q!} \left( i \frac{\partial}{\partial t} \right)^q, \quad (27)$$

and the dispersion coefficients represent a Taylor-series expansion of  $\beta^{(p)}(\omega)$  in Eq. (7) evaluated at the frequency  $\omega_0$ :

$$\begin{aligned} \beta^{(p)}(\omega) &= \beta_0^{(p)} + \beta_1^{(p)}(\omega - \omega_0) + \frac{1}{2}\beta_2^{(p)}(\omega - \omega_0)^2 \\ &+ \sum_{n \geq 3}^{\infty} \frac{1}{n!} \beta_n^{(p)}(\omega - \omega_0)^n. \end{aligned} \quad (28)$$

It is assumed that the pulse evolves in a reference frame moving at the velocity of the fundamental mode  $1/\beta_1^{(1)}$ . All phase and group velocities are referenced to the corresponding values for the fundamental mode, i.e., the first two terms in Eq. (27) are relative to the fundamental mode.

The modes are coupled by the nonlinear effects such as SPM, XPM, and FWM, whose impact in Eq. (26) is included by the following nonlinear terms:

$$\begin{aligned} \mathcal{N}A &= i \frac{n_2 \omega_0}{c} \left( 1 + f_s \frac{i}{\omega_0} \frac{\partial}{\partial t} \right) \sum_{l, m, n}^N \left[ (1 - f_R) S_{plmn}^K A_l A_m A_n^* \right. \\ &\left. + f_R S_{plmn}^R A_l \int_{-\infty}^t h_R(\tau) A_m(z, t - \tau) A_n^*(z, t - \tau) d\tau \right], \end{aligned} \quad (29)$$

where  $S_{plmn}^K$  and  $S_{plmn}^R$  are the nonlinear mode-coupling coefficients for the Kerr and Raman effects, respectively [64]. The values of  $S_{plmn}^K$  and  $S_{plmn}^R$  are in general different when the modes' polarization is taken into account, whereas they become identical within the scalar description of the fiber modes that we adopt in this section [66]. Therefore, we can drop the superscripts K and R and express the nonlinear coefficients as

$$S_{plmn} = \frac{\iint dx dy F_p F_l F_m F_n}{\sqrt{\iint dx dy F_p^2 \iint dx dy F_l^2 \iint dx dy F_m^2 \iint dx dy F_n^2}}, \quad (30)$$

where we made the further assumption of real-valued transverse mode profiles. Equation (29) incorporates the effects of Kerr nonlinearity, Raman scattering (associated with the coefficient  $f_R$ ), and self-steepening (related to the coefficient  $f_s$ ). The nonlinear index of silica is  $n_2 = 2.7 \times 10^{-20} \text{ m}^2/\text{W}$ , and its Raman fraction is  $f_R = 0.18$ . The Raman response function, which is crucial for capturing the nonlinear response of an MMF to ultrashort pulses, can be approximated by

$$h_R(t) = (\tau_1^{-2} + \tau_2^{-2}) \tau_1 \exp(-t/\tau_2) \sin(t/\tau_1), \quad (31)$$

where  $\tau_1 = 12.2 \text{ fs}$  and  $\tau_2 = 32 \text{ fs}$  are related to the frequency and the damping time of the Raman response in silica [56].

## B. Numerical Examples of MMS Formation in a GIMF

This subsection provides concise examples illustrating various phenomena, such as the linear multimode walk off, formation of multimode solitons, their fission and creation of Raman solitons, and collision of two such solitons. These examples not only serve to clarify the basic concepts but also provide a basis for both analytical and experimental exploration.

We assume that the input conditions for all modes are the same in the form of Gaussian pulse, centered at  $t_0$  with a duration characterized by its full width at half maximum (FWHM)  $T_{\text{FWHM}} = 1.665 T_0$ . More specifically,

$$A_p(z = 0, t) = C_p \sqrt{\frac{\mathcal{E}}{T_0 \sqrt{\pi}}} e^{-\frac{(t-t_0)^2}{2T_0^2}}, \quad (32)$$

where  $C_p$  represents the initial modal coupling coefficient, and  $\mathcal{E}$  is the input energy. They are found by projecting an input Gaussian beam  $E_{\text{in}}(x, y)$  onto the eigenmode basis, expressed mathematically as

$$C_p = \iint_{-\infty}^{\infty} E_{\text{in}}(x, y) \cdot F_p(x, y) dx dy. \quad (33)$$

Input conditions are varied by adjusting the two width ratios for the input beam. They are defined as

$$r_w = w/w_{\text{mode}, p=1}, \quad r_s = x_0/w_{\text{mode}, p=1}, \quad (34)$$

where  $w$  is beam's width,  $x_0$  is its lateral offset, and  $w_{\text{mode}, p=1}$  is the width of the fundamental mode. The use of these dimensionless parameters allows for describing diverse input conditions for a given input pulse with parameters such as input energy  $\mathcal{E}$ , temporal duration  $T_0$ , and the parameter values  $r_w$  and  $r_s$ .

When an input beam is aligned with the center of the fiber's core, only a few radial modes are excited (specifically modes  $p = 1, 6, 15, \dots$ , as depicted in Fig. 3). For simplicity, we only take into account these three dominant radial modes corresponding to  $p = 1, 6, 15$  in the following examples.

### 1. Modal Walk-Off and the Formation of an MMS

In the linear regime, modal dispersion leads to temporal walk-off of pulses carried by different modes in a multimode GIMF; see Figs. 7(a) and 7(b). In this case, an input beam with  $r_w = 3$  can be decomposed into the first three radial modes ( $p = 1, 6$ , and 15). The input pulse has a Gaussian shape with a duration of  $T_0 = 110 \text{ fs}$  (FWHM: 184 fs) and has an energy of  $\mathcal{E} = 0.01 \text{ nJ}$ . As the peak power of the input pulse is merely 27.5 W, nonlinear effects remain insignificant due to  $L_N^{(1)} \approx 52.2 \text{ m}$ , but dispersion effects play a pivotal role. This can be seen by noting that the dispersion length is  $L_D^{(1)} \approx 0.72 \text{ m}$ . The walk-off lengths  $L_W$  are 0.82 m and 0.40 m for the mode pairs (1,6) and (1,15), which correspond to DMDs of 0.224 ps/m and 0.464 ps/m, respectively. As seen in Fig. 7(a), after propagating over a distance of  $27.7 L_D = 20 \text{ m}$ , the multimode pulse undergoes significant temporal broadening. The peak delay between mode 1 and mode 6 is approximately 4.8 ps and it increases to 9.3 ps for modes 1 and 15. Given that dispersion solely alters the spectral phase, the spectral power distribution remains unaffected, as illustrated in Fig. 7(b).

However, when the input energy is increased to 0.7 nJ, corresponding to a peak power  $P_0 = 3.58 \text{ kW}$ , the peak powers of

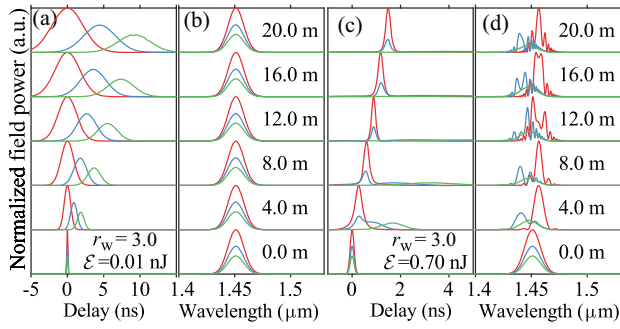


**Fig. 7.** Comparison of the time evolution of temporal and spectral fields in the linear and soliton regimes, respectively: (a), (b) linear regime, (c), (d) MMS regime; the input pulse has a beam size  $r_w = 3$  and a duration of  $T_0 = 110$  fs (FWHM: 184 fs), corresponding to a dispersion length  $L_D \approx 0.72$  m. The normalized temporal and spectral field profiles for modes 1, 6, and 15 are depicted using red, blue, and green curves, respectively, in each panel. For (a), (b) the input pulse energy is  $\mathcal{E} = 0.01$  nJ; for (c), (d)  $\mathcal{E} = 0.70$  nJ; here the Raman effect is neglected, and we set  $f_R = 0$ .

the three excited modes become 1.76 kW for mode 1, 1.10 kW for mode 6, and 0.72 kW for mode 15, and result in different nonlinear lengths for these modes:  $L_N = 0.82$  m for mode 1, 2.55 m for mode 6, and 5.62 m for mode 15. Although  $N^{(1)} = 0.94 < 1$  without considering higher-order mode powers, a qualitatively distinct phenomenon is observed, as shown in Figs. 7(c) and (d). Mode 1 experiences significantly less temporal broadening, facilitating the trapping of a substantial portion of the energy from mode 6. This interaction leads to the formation of an MMS that evolves as a single entity. The group delay of the MMS in Fig. 7(c) falls in between that of modes 1 and 6 in Fig. 7(a). This feature shows that an averaging of the linear group velocities of the constituent modes occurs when an MMS forms. In order to sustain this balanced group velocity, the Kerr nonlinearity produces a red-shift for mode 1 (which decreases its speed) and a blue-shift for mode 6 (which increases its speed) [see Fig. 7(d)]. Note also that the peak power of mode 15 is not large enough to be trapped into the MMS. As a result, the pulse in this mode spreads its energy into a dispersive wave, without much change in its spectral characteristics, as seen in Fig. 7(d).

By varying the input pulse energy, we can determine the threshold for MMS formation. In Figs. 8(a)–8(c), we plot the temporal power distribution (normalized to its maximum value) for modes 1, 6, and 15 at the fiber's output as a function of input pulse energy. In the quasi-linear regime ( $0 < \mathcal{E} < 0.5$  nJ), three modes exhibit significant walk-off and pulse broadening. However, owing to its large nonlinear coefficient  $\gamma^{(1)}$  and its high peak power, mode 1 begins to exhibit less broadening as the input energy increases. To illustrate this feature quantitatively, we plot in Figs. 8(d)–8(f) the pulse peak temporal position, the peak power, and the pulse duration. The temporal position of peak power for mode 1 exhibits a large delay when an MMS forms by trapping mode 6 [see Fig. 8(d)], while the power of all modes keeps increasing [see Fig. 8(e)].

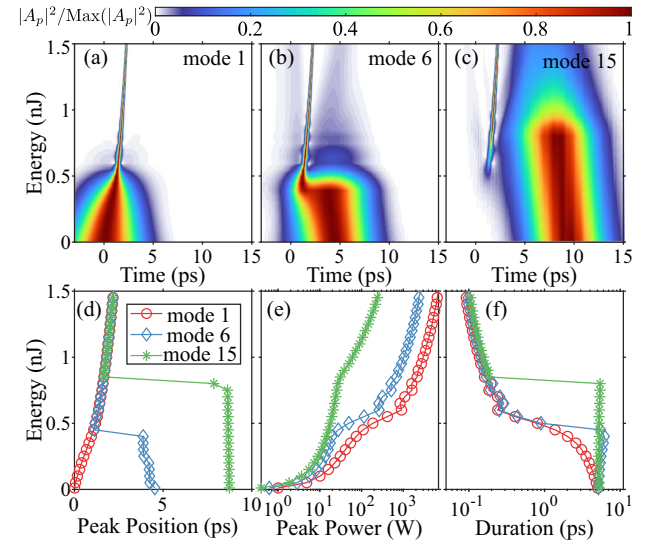


**Fig. 8.** MMS within a GIMF: panels (a)–(c) illustrate the normalized temporal power for modes 1, 6, and 15, respectively, at the output of a 20 m long GIMF, versus input pulse energy. The input pulse has a Gaussian shape with a duration of  $T_0 = 110$  fs (FWHM: 184 fs), a wavelength of 1.45  $\mu\text{m}$ , and a beam width parameter  $r_w = 3$ . Panels (d)–(f) detail corresponding temporal positions of peak power, peak power, and pulse duration at the fiber output. Effects of higher-order dispersion ( $\beta_n^{(p)} = 0, n > 2$ ), Raman ( $f_R = 0$ ), and self-steepening ( $f_S = 0$ ) are disregarded, in order to focus on MMS dynamics only.

However, only the duration of mode 1 is significantly reduced [see Fig. 8(f)]. At an energy of around 0.5 nJ, the peak position of mode 6 aligns with mode 1 [see Fig. 8(d)], which can be considered as the threshold for MMS generation. For mode 15, even though a bit of energy is trapped, most of its energy flows away as a dispersive wave [see Fig. 8(c)], until 0.8 nJ, which is also observed as the turning point of peak power changes in Fig. 8(e). As the MMS forms, the durations of pulses in all three modes become very close to each other, as shown in Fig. 8(f).

## 2. Influence of the Input Beam's Size on MMS

Next, let us consider what is the influence of the input conditions (specifically, the input modal composition) on the formation and propagation characteristics of an MMS, for a given input energy. In Figs. 9(a)–9(c) we plot the output temporal profiles of power (normalized to their maximum values) in modes 1, 6, and 15, respectively, versus input beam waist width  $r_w$ . Here the input energy is fixed at  $\mathcal{E} = 1$  nJ. The corresponding pulse peak temporal position, the pulse peak power, and the pulse duration are depicted in Figs. 9(d)–9(f), respectively. At this energy level, the input pulse energy is effectively redistributed among modes 1 and 6 in order to efficiently form an MMS (see Fig. 8), whereas a portion of input energy coupled to mode 15 only contributes to dispersive waves.

When  $r_w = 1$ , only mode 1 is excited, since the input beams have the same size as mode 1. A singlemode soliton within mode 1 is formed, as indicated by the zero peak power for modes 6 and 15. As  $r_w$  increases, the group velocity of the MMS decreases, which is reflected in the larger group delay at

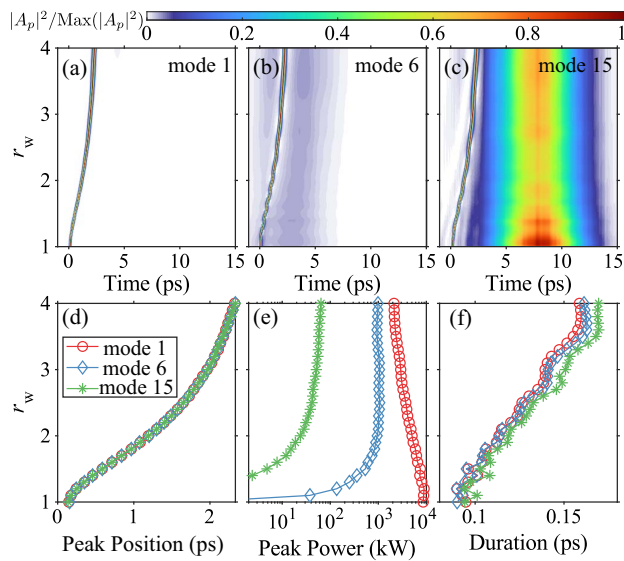


**Fig. 9.** Output mode evolution versus input beam size  $r_w$  (input modal content): the normalized temporal field powers of (a) mode 1, (b) mode 6, and (c) mode 15 at the output of a GIMF are plotted as a function of the normalized input beam size  $r_w$ , when the input pulse energy is 1 nJ, and the pulse duration is  $T_0 = 110$  fs (FWHM: 184 fs), corresponding to a dispersion length  $L_d \approx 2$  m. Panels (d)–(f) detail the corresponding temporal positions of output peak position, peak power, and pulse duration. Here we neglect the effects of higher-order dispersion ( $\beta_n^{(p)} = 0, n > 2$ ), Raman scattering ( $f_R = 0$ ), and self-steepening ( $f_S = 0$ ).

the output, as shown in Fig. 9(d). Moreover, with an increase in  $r_w$ , the high-order modal content of the MMS in modes 6 and 15 also increases, as can be seen in Fig. 9(e). The duration of the MMS expands from 0.1 ps to 0.17 ps, wherein the duration of the pulse in the fundamental mode is slightly shorter than that of pulses in the higher-order modes, as demonstrated by Fig. 9(f).

### 3. Raman Multimode Solitons and Soliton Fission

In the previous examples, the Raman effect was not considered ( $f_R = 0$ ) in the GMMNLSE model. Now, we aim to illustrate how the Raman effect affects MMS. To achieve this, we introduce the Raman effect by setting the delayed nonlinear response coefficient to  $f_R = 0.18$  in Eq. (29). Once the input energy exceeds 1 nJ, the Raman effect becomes notably influential. Here, we provide two examples to showcase its impact on MMS.

In Fig. 10 we illustrate the evolution of the MMS for an input pulse with  $\mathcal{E} = 3$  nJ and a duration of  $T_0 = 110$  fs (FWHM: 184 fs), propagating through a 2 m GIMF. At this energy level, nonlinear effects intensify, enhancing mode coupling and inducing significant temporal and spectral changes. The LOMs undergo a red-shift, whereas the HOMs experience a blue-shift at  $z = 0.4$  m [see Fig. 10(b)], in order to maintain a GVD-induced balance of their different group velocities. As a result, a Raman MMS forms, with a relatively narrower temporal duration and a noticeably red-shifted spectrum, owing to SSFS. At  $z = 2$  m, the central spectrum of the Raman MMS shifts to  $1.52 \mu\text{m}$ . This is accompanied by a decrease in the

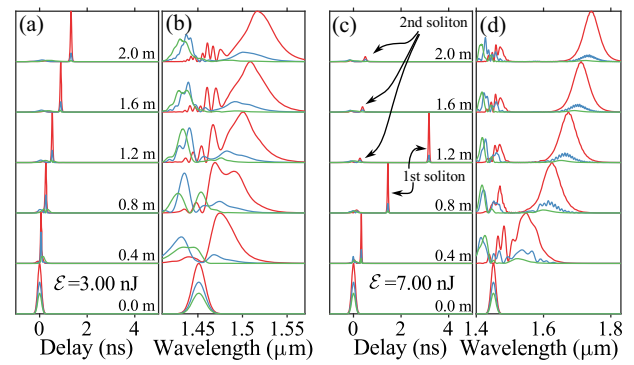


**Fig. 10.** Temporal and spectral evolution of Raman MMS in a 2 m GIMF, when the input pulse energy is (a), (b) 3 nJ and (c), (d) 7 nJ. Here  $f_R = 0.18$ ; other parameters are the same as Fig. 7.

soliton group velocity. When comparing with the MMS group delay in Fig. 7(c), where a 20 m propagation leads to approximately 1.5 ns delay, the MMS in Fig. 10(a) only propagates over 2 m.

When increasing the input energy up to 7 nJ, as depicted in Figs. 10(c) and 10(d), there is sufficient nonlinearity to reorganize the field around  $t = 0$  into a second MMS. This suggests that the initial high-order soliton undergoes fission, resulting in two different MMSs. The first soliton, which carries most of the energy, exhibits a greater delay (extending beyond the plotting window at 1.6 m and 2.0 m) and a larger SSFS. The second MMS carries less energy; however, this is sufficient to form another Raman MMS, featuring a reduced delay and SSFS. Further energy increments can lead the second MMS to gather more energy, resulting in larger group delays (slower group velocities) and heightened SSFS, as detailed in the subsequent subsection.

### 4. SSFS Control and Soliton Collisions

In previous subsections, we observed different dynamics of multimode solitons in MMFs, including modal walk-off, formation of an MMS, and its fission. We also discussed the dependence of the MMS properties on physical parameters such as the input pulse's duration, its group velocity, and SSFS upon varying its energy or modal content. Here, we discuss the possibility of controlling the SSFS of an MMS by adjusting its modal content. Under specific conditions, two Raman MMSs with different group velocities may undergo inelastic collisions, resulting in an energy exchange between them.

As an example, we cite the result in Ref. [39]. In this study, the input beam led to the excitation of the first 15 modes, and the input pulse's duration was 70 fs with a center wavelength of  $1.4 \mu\text{m}$ . Figure 11(a) shows simulated output spectra for a 2 m long GIMF as a function of input pulse energy using  $r_w = 2$  and  $r_s = 0$ , corresponding to the excitation of only radial modes. The SSFS of the first MMS (S1) at the output is visible for input energies exceeding 1 nJ, while the SSFS of the second MMS (S2) becomes pronounced beyond 5 nJ. The SSFS of both Raman MMSs increases with growing input energy.

When the input beam is slightly shifted from the center of the fiber axis, additional non-radial HOMs are introduced ( $r_w = 2.8, r_s = 0.5$ ). In this case, a similar spectral evolution

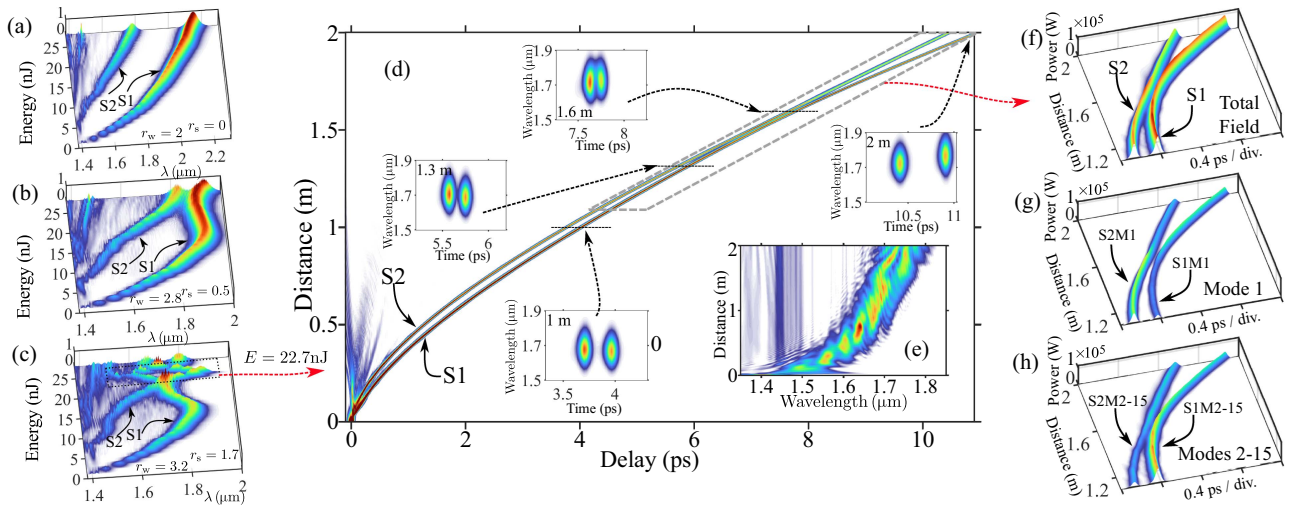


**Fig. 11.** Output spectra are plotted as a function of input pulse energy for a 2 m GIMF under different input conditions: (a)  $r_w = 2$ ,  $r_s = 0$ ; (b)  $r_w = 2.8$ ,  $r_s = 0.5$ ; (c)  $r_w = 3.2$ ,  $r_s = 1.7$ . The temporal and spectral field evolutions as a function of propagation distance are depicted in (d), (e), with inset panels showing the field spectrogram at specific distances. For better visualization, the dashed region in (d) is re-plotted in (f). Panels (g) and (h) illustrate the evolution of fundamental mode content and the sum of other mode contents (modes 2 to 15) with respect to the total in (f). Reprinted with permission from Ref. [39]. Copyright 2022, Optica.

occurs as seen in Fig. 11(b). However, at 15 nJ, S1 undergoes less SSFS-induced red-shift and temporal delay when compared with S2, owing to its reduced fundamental mode content. As the input beam undergoes further energy increase and axial position shift ( $r_w = 3.2$ ,  $r_s = 1.7$ ), the special spectral evolution of S1 seen in Fig. 11(c) becomes evident. The corresponding experimental demonstration is shown in Fig. 40 of Section 9.H. As seen in Fig. 11(c), a surprising spectral feature occurs for input energies between 22.5 nJ and 26 nJ: the soliton spectra exhibit large separations before merging again.

To understand these dynamics, we show the temporal and spectral evolutions of the MMS in Figs. 11(d) and 11(e): here the input energy is 22.7 nJ. Initially, the input pulse splits into two solitons (S1 and S2), which collide and then separate due to their inelastic energy exchange. Despite S2 having a smaller peak power when compared with S1 before their collision [see Fig. 11(f)], S2 gradually exhibits a larger delay (and larger SSFS), eventually leading to its collision with S1.

The analysis of the modal contents reveals that S2 has a relatively larger contribution from the fundamental mode (S2M1) when compared with S1 (S1M1), as depicted in Fig. 11(g). This occurs even though the sum of other mode contents in S1 (S1M2-15) is larger than that of S2 (S2M2-15), as shown in Fig. 11(h). Since the fundamental mode dominates the nonlinear strength, S2 experiences a larger SSFS and group delay, resulting in its collision with S1. As a result of their inelastic collision, the two MMSs exchange energy and separate, because S1 gains more energy in the fundamental mode, thus exhibiting a larger group delay. In Section 9, we shall describe observations giving experimental evidence of the spectral evolution and associated dynamics of collisions between MMSs in multimode GRIN fibers [39].

Furthermore, MMS interactions have been theoretically studied in several papers. In Ref. [67], the interaction between two MMSs in a GIMF, each carrying only the degenerate

modes  $LG_{11a}$  and  $LG_{11b}$  with consideration of their polarization states, was studied. In analogy with the case of single-mode fibers, these MMSs exhibit an attraction or a repulsion behavior, on the basis of their relative phase, despite belonging to different fiber modes. However, unlike the single-mode scenario, each soliton transfers some power to the other mode via intermodal four-wave mixing. Despite this intermodal power exchange, both MMSs maintain their bimodal nature, and interact as if they were traveling in a single-mode fiber.

In Ref. [68], the interaction between fundamental solitons in single-mode fibers under the influence of Raman scattering was extensively investigated. The study reveals a net energy transfer from the leading pulse to the trailing pulse, akin to the behavior that we have described for the multimode scenarios. Furthermore, the impact of different soliton amplitudes or phases on the fraction of transferred energy was analyzed.

### C. Discussion

In this section, we first introduced the eigenmodes and eigenvalues of MMFs, which are important for understanding the nonlinear as well as linear properties of an MMF. By comparing two specific MMFs, a SIMF and a GIMF, we found that the GIMF has dominant nonlinear coefficients for LOMs, thus favoring MMSs composed of low-order modes. Moreover, a GIMF has much reduced modal dispersion, which greatly facilitates the MMS formation. In contrast, a SIMF favors the generation of HOM solitons.

Second, by analyzing the modal eigenvalues, we obtain a piece of key information about the propagation properties of MMFs. For instance, equally-spaced propagation constants in GIMFs enhance mode beating, giving rise to the self-imaging effect. Thus, analyzing  $\beta_1$  for different modes and wavelengths helps us to better understand a key property of the MMS in GIMFs: LOMs propagate faster than HOMs in linear regimes. Therefore, the overall group velocity of MMSs is influenced by

their modal content. Building on these fundamental notions, we introduced the GMMNLSE, which is a relevant model for describing ultrashort pulse propagation in a broad range of MMFs with identifiable eigenmodes.

We elucidated a series of phenomena typical of GIMF: MMS formation via compensation of modal walk-off, MMS fission, mode-based SSFS control, and MMS collisions. Specifically, we analyzed how the Raman effect interacts with MMS: it increases the soliton's wavelength, and LOMs exhibit larger SSFS in GIMFs. This has two significant impacts: first, it reduces the velocity of LOMs, thus diminishing their group velocity mismatch with HOMs and favoring their nonlinear trapping. Second, LOMs with increased red shifts are fed energy by the HOMs with a reduced red-shift, resulting in significant energy transfer from HOMs to LOMs, and eventually leading to Raman beam cleanup into the fundamental mode: corresponding experiments are discussed in Section 9.

Lastly, we discussed the possibility of SSFS manipulation by changing the input modal composition of an MMS. Under specific conditions, two MMSs resulting from the fission of an input pulse and propagating with different modal contents may collide at some point along the fiber, owing to their different group velocities. This section lays the groundwork for deeper explorations into MMS, by either analytical methods or experiments, as discussed in subsequent sections.

#### 4. ANALYTICAL APPROACHES FOR MULTIMODE SOLITONS

In this section, we will review the theoretical framework, leading to analytical results, for describing the dynamics of MMSs. Most of these results rely on the variational formulation of Eq. (26) and the derivation of effective theories for describing an MMS by means of a reduced number of degrees of freedom. In this context, most of the literature focuses on two-mode (or bimodal) soliton formation [69–72]. The multimode case, whose treatment is much more complex, has received much less attention [69]. In Section 4.A, we introduce first the variational formulation for the two-mode soliton case. The Kantarovitch, or average variational approach, which is our main method in this section, is presented in Section 4.B. The effective variational theory obtained with this method for the case of a two-mode bright soliton is presented in Section 4.C. Later, in Section 4.D we will present the virial, or moment method, reviewing the results presented in Ref. [72]. Finally, in Section 4.E we present a generalization of this analysis to a multimode context, following Ref. [69].

##### A. Variational Formulation of Two-Mode Solitons

When just considering two modes, and neglecting high-order effects (e.g., high-order dispersion, Raman effect), Eq. (26) can be written as

$$\begin{aligned} \partial_z A_1 &= i\Delta\beta_0^{(1)} A_1 - \Delta\beta_1^{(1)} \partial_t A_1 \\ &+ \frac{i\beta_2^{(1)}}{2} \partial_t^2 A_1 - i(R_{11}|A_1|^2 + 2R_{12}|A_2|^2) A_1, \end{aligned} \quad (35a)$$

$$\begin{aligned} \partial_z A_2 &= i\Delta\beta_0^{(2)} A_2 - \Delta\beta_1^{(2)} \partial_t A_2 \\ &+ \frac{i\beta_2^{(2)}}{2} \partial_t^2 A_2 - i(R_{22}|A_2|^2 + 2R_{21}|A_1|^2) A_2, \end{aligned} \quad (35b)$$

where we have considered the tensor  $R_{plmn} = S_{plmn} n_2 \omega_0 / c$  symmetries [35]

$$R_{mmmn} = R_{mmmm} = R_{mnn} \quad (36)$$

After a straightforward normalization (see, for example, Ref. [73]), Eq. (35) reduces to

$$i(\partial_z + \delta\partial_t)u + \nu_u u + \frac{\beta_u}{2} \partial_t^2 u + (|u|^2 + C|v|^2)u = 0, \quad (37a)$$

$$i(\partial_z - \delta\partial_t)v + \nu_v v + \frac{\beta_v}{2} \partial_t^2 v + (C|u|^2 + |v|^2)v = 0, \quad (37b)$$

with  $\beta_{u,v} = 1$  for anomalous and  $\beta_{u,v} = -1$  for normal GVD. Note that, under the phase transformation

$$u \rightarrow e^{i\nu_u z} u(z, t), \quad v \rightarrow e^{i\nu_v z} v(z, t), \quad (38)$$

Eq. (37) reduces to

$$i(\partial_z + \delta\partial_t)u + \frac{\beta_u}{2} \partial_t^2 u + (|u|^2 + C|v|^2)u = 0, \quad (39a)$$

$$i(\partial_z - \delta\partial_t)v + \frac{\beta_v}{2} \partial_t^2 v + (C|u|^2 + |v|^2)v = 0, \quad (39b)$$

which is the starting point for most of the analytical research that has been performed in this system (see, e.g., Refs. [70,71]). A key parameter here is the cross-phase modulation (XPM) coefficient  $C$ , which couples fields  $u$  and  $v$ . With  $C = 1$ , Eq. (39) is known as the Manakov equations [74]. Alternatively, one can get rid of the walk-off terms by performing the transformation

$$u(z, t) = U(z, t)e^{i\delta^2 z/2 - i\delta t}, \quad V(z, t) = v(z, t)e^{i\delta^2 z/2 + i\delta t}, \quad (40)$$

which yields the system

$$i\partial_z U + \frac{\beta_u}{2} \partial_t^2 U + (|U|^2 + C|V|^2)U = 0, \quad (41a)$$

$$i\partial_z V + \frac{\beta_v}{2} \partial_t^2 V + (C|U|^2 + |V|^2)V = 0. \quad (41b)$$

In this context, the effect of the walk-off can be reintroduced as an initial splitting velocity between the modal components of a pulse as it is injected into the fiber. Thus, the effect of temporal walk-off owing to modal dispersion can be transferred to an initial relative frequency shift among the two input pulse components [75,76].

##### 1. Lagrangian and Hamiltonian Formalisms

The set of Eq. (37) can be derived from the Lagrangian density

$$\mathcal{L} \equiv \mathcal{L}_u + \mathcal{L}_v + \mathcal{L}_{\text{int}}, \quad (42)$$

with

$$\begin{aligned}\mathcal{L}_u &\equiv i(u^* \partial_z u - u \partial_z u^*) + i\delta(u^* \partial_t u - u \partial_t u^*) - \beta_u |\partial_t u|^2 + |u|^4, \\ \mathcal{L}_v &\equiv i(v^* \partial_z v - v \partial_z v^*) - i\delta(v^* \partial_t v - v \partial_t v^*) - \beta_v |\partial_t v|^2 + |v|^4,\end{aligned}$$

and the interaction contribution

$$\mathcal{L}_{\text{int}} \equiv 2 C |u|^2 |v|^2.$$

Then Eq. (39) can be retrieved through the Euler-Lagrange equations

$$\frac{\partial}{\partial z} \left( \frac{\partial \mathcal{L}}{\partial u_z^*} \right) + \frac{\partial}{\partial t} \left( \frac{\partial \mathcal{L}}{\partial u_t^*} \right) - \frac{\partial \mathcal{L}}{\partial u^*} = 0, \quad (43a)$$

$$\frac{\partial}{\partial z} \left( \frac{\partial \mathcal{L}}{\partial v_z^*} \right) + \frac{\partial}{\partial t} \left( \frac{\partial \mathcal{L}}{\partial v_t^*} \right) - \frac{\partial \mathcal{L}}{\partial v^*} = 0. \quad (43b)$$

Similarly, the application of the transformation Eq. (40) to the Lagrangian Eq. (42) leads to the new Lagrangian density

$$\mathcal{L} \equiv \mathcal{L}_U + \mathcal{L}_V + \mathcal{L}_{\text{int}}, \quad (44)$$

with

$$\mathcal{L}_U \equiv i(U^* \partial_z U - U \partial_z U^*) - \beta_u |\partial_t U|^2 + |U|^4, \quad (45)$$

$$\mathcal{L}_V \equiv i(V^* \partial_z V - V \partial_z V^*) - \beta_v |\partial_t V|^2 + |V|^4, \quad (46)$$

$$\mathcal{L}_{\text{int}} = 2 C |U|^2 |V|^2, \quad (47)$$

from where Eq. (41) can be also derived.

By defining the generalized momenta

$$\mathcal{P}_u \equiv \frac{\partial \mathcal{L}}{\partial U_z^*} = iU/2, \quad \mathcal{P}_v \equiv \frac{\partial \mathcal{L}}{\partial V_z^*} = iV/2, \quad (48)$$

this system can be alternatively described by Hamiltonian density obtained through the Legendre transform

$$\mathcal{H} = \mathcal{P}_u U_z^* + \mathcal{P}_u^* U_z + \mathcal{P}_v V_z^* + \mathcal{P}_v^* V_z - \mathcal{L}, \quad (49)$$

which leads to

$$\mathcal{H} = \mathcal{H}_U + \mathcal{H}_V + \mathcal{H}_{\text{int}}, \quad (50)$$

with

$$\mathcal{H}_U = \beta_u |\partial_t U|^2 - |U|^4, \quad \mathcal{H}_V = \beta_v |\partial_t V|^2 - |V|^4, \quad (51)$$

and

$$\mathcal{H}_{\text{int}} = -2 C |U|^2 |V|^2. \quad (52)$$

## 2. Conservation Laws

From the momentum-energy tensor defined through our Lagrangian [77], the following conservation laws can be deduced.

• **Conservation of power.** The powers carried by each mode are defined as

$$P_u \equiv \int_{-\infty}^{\infty} |u|^2 dt, \quad P_v \equiv \int_{-\infty}^{\infty} |v|^2 dt. \quad (53)$$

These quantities satisfy

$$\partial_z P_u = 0, \quad \partial_z P_v = 0, \quad (54)$$

which means that they are conserved individually along propagation in  $z$ . This is a direct consequence of the fact that all terms in Eq. (42) are real [72].

• **Conservation of the total momentum.** The momentum for each field  $u, v$  is defined as

$$J_u \equiv i \int_{-\infty}^{\infty} (u u_t^* - u_t^* u) dt, \quad J_v \equiv i \int_{-\infty}^{\infty} (v v_t^* - v_t^* v) dt. \quad (55)$$

The total momentum  $J = J_u + J_v$  is conserved along propagation, i.e.,

$$\partial_z J = \partial_z (J_u + J_v) = 0. \quad (56)$$

• **Conservation of the total energy.** The last quantity to be conserved is the total energy or Hamiltonian function

$$H = H_u + H_v + H_{\text{int}} = \int_{-\infty}^{\infty} (\mathcal{H}_u + \mathcal{H}_v + \mathcal{H}_{\text{int}}) dt. \quad (57)$$

The conservation law in this case reads

$$\partial_z H = \partial_z (\mathcal{H}_u + \mathcal{H}_v + \mathcal{H}_{\text{int}}) = 0. \quad (58)$$

## B. Average Variational Approach: Rayleigh-Ritz or Kantarovitch Optimization

In this section, we introduce the averaged variational method, which is widely used in order to compute soliton solutions in an optical context [15]. Originally presented in an optical context by Anderson *et al.* [78], this method is also known as the Rayleigh-Ritz or Kantarovitch optimization approach and generalizes its stationary version: the Ritz approach [78–80]. This method allows us to compute approximate analytical solutions of a given nonlinear partial differential equation by applying the principle of least action to a parameter-dependent solution ansatz, based on either the Lagrangian or the Hamiltonian formalism. In what follows, we describe the main steps in either the Lagrangian or the Hamiltonian formalism.

### 1. Kantarovitch Method in the Lagrangian Formalism

The method consists of the following four main steps.

(1) First of all, we need to define an approximate ansatz solution, or trial function, that captures the main features and shape of the state that we want to compute. This ansatz is a function of the form  $u = u[t; q(z)]$ , which depends on  $z$  through a number of parameters:

$$q(z) = \{q_1(z), \dots, q_n(z)\},$$

which are the generalized coordinates of the system.

(2) Given a Lagrangian density associated with a certain set of partial differential equations [see, e.g., Eq. (42)], the next step in this procedure is to compute the effective reduced Lagrangian function of the system, which, in the context of temporal MMSs studied here, is defined as

$$L[q(z)] \equiv \int_{-\infty}^{\infty} \mathcal{L}[u, u^*, \dots; q(z)] dt. \quad (59)$$

(3) After that, we obtain the dynamical system for the generalized coordinates by computing the Euler-Lagrange equations

$$\frac{d}{dz} \left( \frac{\partial L}{\partial (d_z q_m)} \right) - \frac{\partial L}{\partial q_m} = 0 \quad (60)$$

for each parameter  $q_m$  with  $m = 1, \dots, n$ , where we have defined  $d_z q_m \equiv dq_m/dz$ .

(4) Finally, in the last step, we study the dynamics of the reduced system Eq. (60), and rebuild the behavior of the original system by using the initial ansatz.

## 2. Kantarovitch Method in the Hamiltonian Formalism

Equivalently, one may consider the Hamiltonian formalism for obtaining an effective reduced system. The process is equivalent to that followed in the Lagrangian case, but now we use the Hamiltonian

$$H[q(z), p(z)] \equiv \int_{-\infty}^{\infty} \mathcal{H}[u, u^*, \dots; q(z)] dt, \quad (61)$$

where  $p(z) = \{p_1(z), \dots, p_n(z)\}$  are the generalized momenta defined as

$$p_m = \frac{\partial L}{\partial (d_z q_m)}.$$

Then, the effective dynamics of the system are captured by the Hamiltonian equations of motion

$$\frac{dq_m}{dz} = \frac{\partial H}{\partial p_m}, \quad \frac{dp_m}{dz} = -\frac{\partial H}{\partial q_m} \quad (62)$$

for each  $m = 1, \dots, n$ .

## C. Effective Variational Theories for Bimodal Bright Solitons: Escaping versus Bound-State Solitons

Once that variational machinery has been introduced, we will try to answer the following question: which kind of initial condition for Eq. (39) leads to the formation of a two-mode soliton?

Most of the works dealing with two-mode soliton formation focus on a regime where each mode in the fiber experiences anomalous GVD [69–71,75]. In comparison with this case, the mixed scenario has been much less studied [81].

In this section, we will mainly focus on the interaction of bright solitons, where both modal components are propagating in the anomalous dispersion regime. In what follows, we take  $\beta_u = \beta_v = 1$ . In this context, two main behaviors are found: either (i) the two solitons split and escape or (ii) they are trapped, forming a bound state, i.e., a two-mode soliton. These solitons, however, are not static upon propagation, but they undergo oscillations in their separation and peak powers [73]. An example of this regime is depicted in Fig. 12.

The threshold between these two regimes deeply depends on two main factors: the strength of temporal walk-off, or the initial relative frequency shift of the pulses, and the strength  $C$  of the XPM. One of the first researchers who investigated these phenomena was Menyuk in 1987. He found, by performing numerical simulations, that the splitting could be arrested through XPM, and that the threshold for mutually trapped solitons increases with increasing walk-off [73]. After that, many theoretical works focused on understanding this phenomenon and on the analytical determination of that threshold [69–72].

Instead of reviewing these results in chronological order, we have decided to organize them in terms of the variational formalism that was applied.

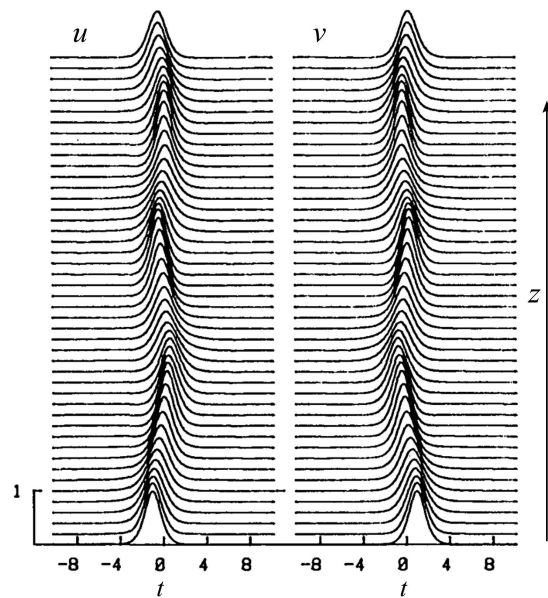


**Fig. 12.** Bound state, or trapped, oscillatory regime for  $C = 2/7$ . Adapted from Ref. [81].

## 1. Lagrangian Formalism

Let us first review some results based on a Lagrangian approach. One of the first works to tackle this problem was that of Ueda and Kath [70]. In the following, we will use these results as the main guiding example for didactic purposes.

Their approach considered the Lagrangian Eq. (44), which is more adequate for investigating soliton formation, in detriment of the explicit appearance of the linear walk-off  $\delta$  in the results.

The general soliton ansatz they considered was

$$u = \eta_u \operatorname{sech}\left(\frac{t - \tau_u}{w_u}\right) e^{i\Phi_u}, \quad v = \eta_v \operatorname{sech}\left(\frac{t - \tau_v}{w_v}\right) e^{i\Phi_v}, \quad (63)$$

with the phases

$$\Phi_u \equiv V_u(t - \tau_u) + \frac{\theta_u}{2w_u}(t - \tau_u)^2 + \phi_u,$$

$$\Phi_v \equiv V_v(t - \tau_v) + \frac{\theta_v}{2w_v}(t - \tau_v)^2 + \phi_v,$$

where  $\eta_{u,v}$ ,  $w_{u,v}$ , and  $\tau_{u,v}$  are the amplitude, width, and central position of the fields  $u$  and  $v$ , respectively. These parameters correspond to the three lowest-order moments of the soliton envelopes.  $V_{u,v}$ ,  $\theta_{u,v}$ , and  $\phi_{u,v}$  represent the three lowest-order moments of the phase  $\Phi_{u,v}$ . These are the nonlinear velocity of the soliton central position, the chirp of the soliton (related to the change of the soliton temporal width), and the linear phase, respectively.

By computing the Euler-Lagrange Eq. (60) with this ansatz, the authors obtained an eight-dimensional reduced dynamical system for describing the evolution of the corresponding ansatz parameters. This effective theory allowed the study of both symmetric and asymmetric soliton configurations. However, due to the complexity of the former scenario, the authors



focused on the symmetric case, which is the one that we review in the following paragraphs.

Let us consider two identical solitons that are symmetrically located in time on opposite points around their mean position, and that propagate in opposite directions (in a reference frame propagating with the average group velocity). This implies:  $w_u = w_v = w$ ,  $\eta_u = \eta_v = \eta$ ,  $\theta_u = \theta_v = \theta$ ,  $V_u = -V_v = -V$ , and  $\tau_u = -\tau_v = -\tau$ . With these considerations, the effective Lagrangian

$$L = \int_{-\infty}^{\infty} \mathcal{L}(u, u^*, v, v^*) dt \quad (64)$$

yields the Euler-Lagrange equations

$$\frac{d\tau}{dz} = V, \quad (65a)$$

$$\frac{dV}{dz} = \frac{CP}{w^2} \partial_{\Delta} F(\Delta), \quad (65b)$$

$$\frac{d\theta}{dz} = \theta, \quad (65c)$$

$$\frac{d\theta}{dz} = \frac{4}{\pi^2 w^2} \left\{ w^{-1} - \frac{P}{2} - \frac{3}{2} CP \partial_{\Delta} [\Delta F(\Delta)] \right\}, \quad (65d)$$

where

$$F(\Delta) \equiv \frac{\cosh \Delta}{\sinh^3 \Delta} (\Delta - \tanh \Delta), \quad \Delta \equiv \frac{2\tau}{w}, \quad (66)$$

and  $P = P_u = P_v = 2\eta^2 w$  is the conserved mode power [see Eq. (53)]. The fixed points of this system correspond to a shape-preserving two-mode soliton, which is a center of the dynamics; hence it is neutrally stable: any small fluctuation of the system will drive it away from this point [82]. Interestingly, around this point a continuous family of oscillatory states may appear, which correspond to dynamical two-mode solitonic states. We will come back to this in a few paragraphs.

A way to obtain more information about this bimodal soliton system is by studying the effective Hamiltonian

$$H = H_u + H_v + H_{\text{int}} = \int_{-\infty}^{\infty} (\mathcal{H}_U + \mathcal{H}_V + \mathcal{H}_{\text{int}}) dt, \quad (67)$$

associated with our ansatz. After some algebra, the Hamiltonian can be reorganized as  $H = H_I + H_K$ , where

$$H_I \equiv \frac{1}{6} \left( \frac{P}{2} - \frac{1}{w} \right)^2 + \frac{\pi^2}{24} \theta^2 \quad (68a)$$

is a measure of the internal energy in each soliton, which is taken up by pulse-width oscillations and

$$H_K \equiv \frac{1}{2} V^2 - \frac{CP}{2w} F(\Delta) \quad (68b)$$

represents the kinetic and potential energy due to the coupling between the  $u$  and  $v$  solitons [70]. As we know from the conservation law Eq. (58),  $H = \mathcal{E} = \text{const}$ , where  $\mathcal{E}$  is the initial energy of the system, that is,  $\mathcal{E} \equiv H(0)$ .

Depending on the sign of  $\mathcal{E}$ , two behaviors are possible.

- $\mathcal{E} < 0$ : **bound state regime**. The two pulses attract each other, and form a bound state, wherein the pulse central position  $\tau$  and width  $w$  undergo periodic oscillations in  $z$  [70,73]. This bound state corresponds to a dynamic two-mode soliton.
- $\mathcal{E} > 0$ : **escaping or splitting regime**. When  $H = \mathcal{E} > 0$ , however, the two pulses have enough initial velocities, or frequency-shift (walk-off) to overcome the XPM-induced attraction, yielding two well-separated independent solitons.

The condition  $H = \mathcal{E} = 0$  marks a separatrix, i.e., the threshold between these two behaviors. This condition provides the escape velocity  $V_e$ .

In the chirp-free case ( $\theta = 0$ ), the escape velocity for two initially superimposed solitons ( $\tau = 0$ ) reads

$$V_e^2 = \mu P^2 C \left( 1 + \frac{C}{2} \right), \quad \mu \equiv \frac{1}{6}. \quad (69)$$

Thus, the formation of two-mode solitons depends on the initial velocity, mode energy, and on the strength of the XPM interaction  $C$ . In the phase plane defined by the parameters  $\tau$  and  $V$  [see Fig. 13(a)], the escape velocity is the separatrix between the bound state and the escaping soliton regime.

In the bound-state regime, there is a continuous family of oscillatory states for continuous values of  $H = \mathcal{E} < 0$ , which correspond to oscillations of the bimodal soliton central position [see closed orbit in Fig. 13(a)]. Such an oscillatory dynamic can be described by combining Eq. (65a) with (65b). This leads to the second-order ODE

$$\frac{d^2 \Delta}{dz^2} - \frac{2 CP}{w^3} \partial_{\Delta} F(\Delta) = 0, \quad (70)$$

where  $w$  is a constant [see Eq. (65c)].

In a strongly bound system, where  $\Delta$  is small ( $\Delta \ll 1$ ),

$$F(\Delta) \approx 1/3 - 2\Delta^2/15,$$

and one gets the simplified equation

$$\frac{d^2 \Delta}{dz^2} + \omega_{\Delta}^2 \Delta = 0, \quad \omega_{\Delta}^2 \equiv \frac{8 CP}{15 w^3}, \quad (71)$$

which describes the relatively small amplitude oscillations of the soliton positions ( $\Delta$ ) with frequency  $\omega_{\Delta}$ . Thus, in the chirp-free case  $\Delta$  experiences harmonic oscillations in  $z$  of the form

$$\Delta \propto 2 \tau \propto \cos(\omega_{\Delta} z).$$

An example of this oscillation is shown in Fig. 13(b) using a dotted line. Note that the escape velocity can also be determined by transforming Eq. (70) into an energy conservation equation, as discussed in Refs. [71,83].

Obviously, the previous analysis only provides a qualitative description of the bimodal soliton system. A more realistic description requires the consideration of the chirp, and thus the modification of  $w$ . Indeed, numerical results obtained with the original Eq. (39) reveal the presence of oscillations in both the pulse positions and widths (see Fig. 2 in Ref. [70]); moreover, these two oscillations are not commensurate, i.e., non-periodic.

To better understand the reason for these disagreements, it is necessary to consider the presence of pulse chirp ( $b \neq 0$ ), and

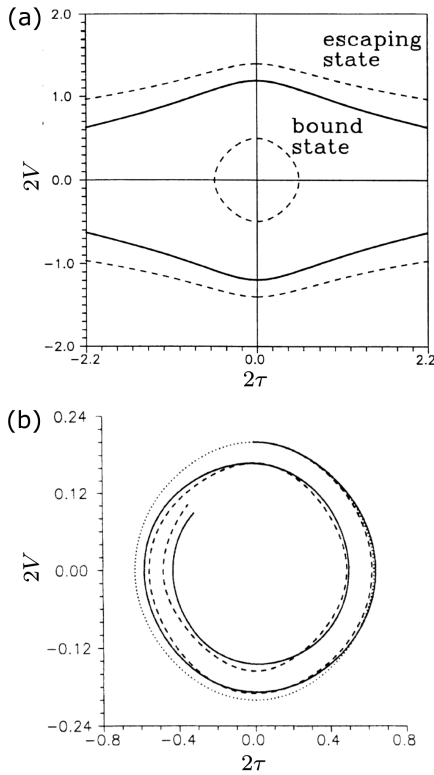


**Fig. 13.** (a) Regions of bound and escaping solitons in the  $(\tau, V)$  phase space for  $\theta = 0$ . (b) Comparison of simulations carried out using Eq. (39) (solid line), Eq. (65) for  $\theta \neq 0$  (dashed line) and for  $\theta = 0$  (dotted line). Adapted from Ref. [70].

study the full system of Eqs. (65a)–(65d), which now allows for the variation of  $w$  and thus  $\eta$ . This extra degree of freedom shows that the periodic orbits in phase space are not periodic but quasiperiodic, and the pulse oscillations and width are not commensurate. The reason for this is that the kinetic and internal oscillations of this model are now governed not just by one frequency, but by the two frequencies

$$\omega_K^2 = \omega_\Delta, \quad \omega_I^2 = \frac{P^4}{4\pi^2}. \quad (72)$$

The comparison between the previous analysis and the numerical results is depicted in Fig. 13(b). The presence of this new frequency, due to the extra degree of freedom ( $b \neq 0$ ), shows that the orbits do not close and are quasiperiodic: the pulse position and width are not commensurate.

These results were later revisited by Kaup *et al.* by considering a Gaussian ansatz [75]. Although quantitatively less accurate, this ansatz provides a deeper qualitative insight and analytical predictions not only for the symmetric, but for the asymmetric configuration as well, something that was not possible in previous works. In this context, a more general expression for  $V_e$  was found [see Eq. (19a) in Ref. [75]]. Near the condition  $P_u = P_v$ , this velocity can be approximated also by Eq. (69), but with  $\mu \equiv 1/(2\pi)$ .

In the bound-state regime, the linear stability analysis around the fixed point of the reduced effective dynamical system reveals the presence of not two, but three internal

modes of the two-mode soliton that oscillates with the eigenfrequencies:

$$\omega_1 \approx \frac{1}{4} C^{1/2} (1 + C)^{3/2} P^2, \quad (73a)$$

analogous to  $\omega_K$  in Eq. (72),

$$\omega_2 \approx \frac{1}{4} (1 + C)^2 P^2, \quad (73b)$$

related to  $\omega_I$ , and

$$\omega_3 \approx \frac{1}{4} (1 + C)^{3/2} (1 + 4C) P^2, \quad (73c)$$

a frequency that was not previously predicted, which is responsible for the antisymmetric shape oscillations of the symmetric two-mode soliton [75].

In 1990, Kivshar included explicitly the linear walk-off  $\delta$  in the system description [see Eq. (37)]. In this case, he used the Lagrangian density Eq. (42) and a modified version of the ansatz Eq. (63), where the chirp is neglected and  $\eta_{u,v} = w_{u,v}^{-1} (1 + C)^{-1/2}$  [71]. Similar to the work of Ueda and Kath [70], the author only considered the symmetric solution case (i.e.,  $w_u = w_v = w = \text{const.}$ ,  $V_1 = -V_2 = -V$ ). In this context, the reduced Euler-Lagrange equations simplify to

$$\frac{d\Delta}{dz} = \frac{2}{w} (V + \delta), \quad \frac{dV}{dz} = -\frac{w}{2} \partial_\Delta U_{\text{int}}(\Delta), \quad (74)$$

where  $\Delta$  is the relative distance between the two modes' maxima [same as in Eq. (66)], and

$$U_{\text{int}} \equiv \frac{8C}{(1+C)w^4} \left[ \frac{1}{3} - F(\Delta) \right] = \frac{4CP}{w^3} \left[ \frac{1}{3} - F(\Delta) \right] \quad (75)$$

represents an effective interaction energy between the two modes, where we have used that  $P = \frac{2}{w(1+C)}$ .

In the strongly bound regime ( $\Delta \ll 1$ ),

$$U_{\text{int}} \approx \frac{8CP}{15w^3} \Delta^2, \quad (76)$$

and the combination of Eq. (74) leads to the same Eq. (71), where the oscillatory frequency now reads

$$\omega_\Delta^2 \equiv \frac{16CP}{15w^3}, \quad (77)$$

which is twice the value predicted by Ueda and Kath [70].

By using the conservation of the total energy of the system, a separatrix between the bound state and the escaping soliton regimes was obtained in terms of the walk-off and width of the pulses. Thus, two-mode bound states will form if

$$\frac{1}{2} \left( \frac{2\delta}{w} \right)^2 \leq U_{\text{max}} \equiv \frac{4CP}{3w^3}, \quad (78)$$

which leads to the threshold walk-off

$$\delta_{\text{th}}^2 \leq \frac{2CP}{3w} = \frac{4}{3} \frac{C}{(1+C)w^2}. \quad (79)$$

In terms of the amplitude of the input pulse  $A$ , this threshold reads

$$A_{\text{th}}(\delta, C) = A_g + \frac{1}{2} \sqrt{\frac{3}{2C}} \delta, \quad A_g(C) \equiv \frac{1}{\sqrt{2(1+C)}}, \quad (80)$$

which shows a linear dependence with  $\delta$ , in contrast to previous results by Caglioti *et al.*, where such a dependence is quadratic [69]. Note that within this approach, the gap amplitude  $A_g$  cannot be directly derived: it was obtained by using a result from the inverse scattering method (see discussion in Ref. [72]).

Figure 14 compares, for  $C = 2/3$ , these results with those of Menyuk [73] and Hasegawa [33], who using an analogy based on quantum mechanics, derived a trapping condition with an amplitude threshold which is also proportional to  $\delta$  (see the dashed line in Fig. 14). However, their theory does not predict the amplitude gap  $A_g$  [33].

In our context, these results can be read as follows: when  $A_g < A < A_{th}$  for  $\delta$  fixed, the two modes interact slightly, and the symmetric soliton configuration splits into two independent solitons traveling in opposite directions; for  $A > A_g$  the initial pulses form a bound state, i.e., a two-mode soliton, owing to the intermodal coupling described by the effective interaction energy  $U_{int}$ .

Similar results were found by Karlsson *et al.* when investigating two soliton collisions in singlemode fibers, owing to the effect of XPM for  $C = 2$  [83]. We recommend this work for its completeness and clarity. A generalization of the Lagrangian formalism for two-mode dynamics when considering  $N$  parameters in the soliton ansatz was also proposed by Caglioti *et al.* in 1990 [84].

## 2. Hamiltonian Formalism

Approaching the problem from a different perspective, one may also describe the dynamics of two-mode solitons in the context of the Hamiltonian formalism. The first time that this formulation was used to describe the dynamics of pulses in two-mode fibers was in 1988 with the work of Caglioti *et al.* [69]. By deriving an effective Hamiltonian for an arbitrary number of fiber modes (see Section 4.E), they were able to describe the interaction of a bimodal bright soliton complex in the presence

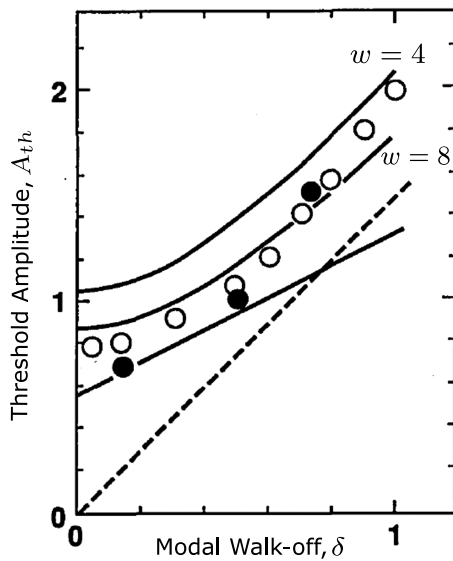


**Fig. 14.** The solid line corresponds to the analytical results of Kivshar [71]. The dashed line shows the estimation of Hasegawa [33]. The numerical results of Menyuk are plotted using filled circles [73]. Here  $C = 2/3$ . Adapted from Ref. [72].

of linear walk-off. The authors found that the threshold amplitude for two-mode soliton formation depends quadratically on  $\delta$ . However, they were not able to predict the gap that appears when  $\delta \rightarrow 0$ , in contrast to Kivshar [71].

One year later, by applying similar approaches, Afanasyev *et al.* found that the interaction of two bright solitons could be described by the interaction Hamiltonian [81]

$$H_{int} = b_0 F(\Delta), \quad b_0 \equiv -\frac{8C}{1+C} \frac{1}{w^3}. \quad (81)$$

The equation of motion associated with this quantity predicts periodic soliton oscillations with a frequency [81]

$$\omega_\Delta^2 = \frac{16}{15} \frac{C}{1+C} \frac{1}{w^2} = \frac{8}{15} \frac{CP}{w}, \quad (82)$$

which is proportional to  $1/w$ , and not to  $1/w^3$  as it was derived in other works [70,71].

In 1992, Mesentev and Turitsyn found a way to characterize the stability of two-mode solitons with equal amplitudes, by deriving integral conditions describing the trapping [85]. By applying Lyapunov stability theory, they were able to derive an exact condition for mutual soliton trapping. Thus, for any initial condition satisfying

$$H < -\frac{\delta^2}{2} (P_u + P_v) - \frac{1}{24} (P_u^3 + P_v^3), \quad (83)$$

a two-mode soliton state will form. Note that this condition is general and it applies to initial pulses with any kind of shape, in contrast to other works that typically used a sech-type solution ansatz.

## D. Moment Approach for Two-Mode Solitons

In 1993, Cao and McKinstrie applied a different approach, based on the virial theorem, for understanding Menyuk's results [72]. The general idea behind this method, known as the moment or virial approach, is to use the conservation laws of the system (see Section 4.A.2) to obtain an expression of a suitable average value of a physical quantity in terms of the conserved quantities  $P_T = P_u + P_v$ ,  $H$ , and  $J$  [86]. In our problem, we are interested in the separation distance between pulses  $\Delta_\tau = 2\tau$ , whose first and second moments are given by

$$\langle \Delta_\tau^n \rangle = P_T^{-1} \int \Delta_\tau^n (|u|^2 + |v|^2) dt, \quad (84)$$

with  $n = 1, 2$ , respectively. From the virial equation, describing the evolution in  $z$  of the variance  $\sigma^2 = \langle \Delta_\tau^2 \rangle - \langle \Delta_\tau \rangle^2$ , Cao and McKinstrie found a sufficient condition for a bound, or trapping state, to form: it reads as

$$H + \frac{\delta^2}{2} P_T + \frac{1}{4} \left( \frac{P_u^2}{w_u} + \frac{P_v^2}{w_v} \right) - \frac{[J + \delta(P_u - P_v)]^2}{2P_T} \leq 0. \quad (85)$$

They considered a general situation where the widths of the two pulses,  $w_u$  and  $w_v$ , can be different from each other. Note that all terms in the previous expression are constants of the motion. Therefore, one may analyze the two-mode behavior by simply considering these invariants, no matter how the pulse shape changes.

By considering a symmetric two-soliton input (i.e.,  $P_u = P_v = P$ ,  $w_u = w_v = w$ ), the authors were able to derive the amplitude threshold condition

$$A_{\text{th}} = \left( \frac{1 + 3\delta^2}{1 + C - 3/w} \right)^2, \quad (86)$$

which is plotted in Fig. 14 for two different widths, namely,  $w = 4$  and 8.

Moreover, considering that pulses do not change their shape during propagation, which is valid for  $\delta$  small, and supposing that their separation distance is also small ( $\Delta \ll 1$ ), they obtained a different value for the frequency at which  $\Delta$  oscillates:

$$\omega_{\Delta}^2 = \frac{4}{5} \frac{1}{(1+C)w^4} = \frac{2}{15} \frac{P}{w^3}, \quad (87)$$

which is also proportional to  $P$ , consistent with other works (see, e.g., Refs. [70,71]).

### E. Multimode Generalization

The generalization of the previous theoretical findings to the case of a number of modes greater than two is practically absent. Only in the work by Caglioti *et al.* was an effective Hamiltonian derived based on a general ansatz for the description of each mode [69]. However, the Hamiltonian system was only utilized for the study of a single and two-mode scenario.

Neglecting high-order effects, the dimensional coupled-mode equations that Caglioti *et al.* considered read as

$$\begin{aligned} (\partial_z + v_m^{-1} \partial_t) A_m &= \frac{i\beta_2^{(m)}}{2} \partial_t^2 \\ &- 2i \left( \frac{R_{mm}}{2} |A_m|^2 + \sum_{l=1}^N R_{ml} |A_m|^2 \right) A_m \end{aligned} \quad (88)$$

for  $m = 1, \dots, N$ .

By writing the general ansatz for the  $m$ th mode as

$$A_m(z, t) = |A_m(z, t)| e^{i\psi_m(z, t)}, \quad (89)$$

and taking

$$|A_m(z, t)|^2 = \frac{P_m}{w_m(z)} f \left[ \frac{t - \tau_m(z)}{w_m(z)} \right], \quad m = 1, \dots, N, \quad (90)$$

with

$$\begin{aligned} \partial_t \psi_m(z, t) &= -\frac{2}{P_m} \{ \xi_m(z) + 2b_m(z)[t - \tau_m(z)] \}, \\ m &= 1, \dots, N, \end{aligned}$$

where  $f(x)$  is any positive-definite even function normalized to one with unit variance,  $P_m$ ,  $\tau_m$ , and  $M_m = w_m^2$  are the zeroth-, first-, and second-order moments of  $|A_m(z, t)|^2$ , namely,

$$P_m = \int_{-\infty}^{\infty} |A_m(z, t)|^2 dt, \quad (91a)$$

$$\tau_m(z) = P_m^{-1} \int_{-\infty}^{\infty} t |A_m(z, t)|^2 dt, \quad (91b)$$

$$M_m(z) = P_m^{-1} \int_{-\infty}^{\infty} (t - \tau_m)^2 |A_m(z, t)|^2 dt, \quad (91c)$$

and  $\xi_m$ ,  $b_m$  are the conjugate variables to  $\tau_m$  and  $M_m$  [69,84], the effective Hamiltonian associated to this system reads  $H = K + V$ , with

$$K = \sum_{m=1}^N \left[ \frac{\xi_m}{v_m} - \frac{\beta_2^{(m)}}{P_m} (\xi_m^2 + 4M_m b_m^2) - \frac{P_m c_1 \beta_2^{(m)}}{4M_m} - \frac{R_{mm} P_m^2 c_2}{4\sqrt{M_m}} \right],$$

and

$$V = -\sum_n \sum_{n \neq m} \frac{1}{2} \frac{R_{mn} P_m P_n}{\sqrt{M_m M_n}} \int_{-\infty}^{\infty} f \left( \frac{t - \tau_m}{\sqrt{M_m}} \right) f \left( \frac{t - \tau_n}{\sqrt{M_n}} \right) dt,$$

$$c_1 \equiv \int_{-\infty}^{\infty} f^{-1} \left( \frac{df}{dx} \right)^2 dx,$$

$$c_2 \equiv \int_{-\infty}^{\infty} f(x)^2 dx. \quad (92)$$

This Hamiltonian possesses  $2 \times N$  degrees of freedom, and the Hamiltonian equations of motion,

$$\begin{aligned} \frac{d\tau_m}{dz} &= \frac{\partial H}{\partial \xi_m}, & \frac{d\xi_m}{dz} &= -\frac{\partial H}{\partial \tau_m}, & \frac{dM_m}{dz} &= \frac{\partial H}{\partial b_m}, \\ \frac{db_m}{dz} &= -\frac{\partial H}{\partial M_m}, \end{aligned}$$

become

$$\frac{d\tau_m}{dz} = \frac{1}{v_m} - \frac{2\beta_2^{(m)} \xi_m}{P_m}, \quad (93a)$$

$$\frac{d\xi_m}{dz} = -\frac{\partial V}{\partial \tau_m}, \quad (93b)$$

$$\frac{dM_m}{dz} = -\frac{8b_m \beta_2^{(m)} M_m}{P_m}, \quad (93c)$$

$$\frac{db_m}{dz} = \frac{4b_m^2 b_m}{P_m} - \frac{P_m c_1 \beta_2^{(m)}}{4M_m^2} - \frac{R_{mm} P_m^2 c_2}{8M_m^{3/2}} - \frac{\partial V}{\partial M_m}. \quad (93d)$$

This reduced Hamiltonian system could be used for investigating, at least qualitatively, the behavior of MMSs in MMFs. However, in their original work, Caglioti *et al.* only focused on the single and two-mode configurations [84]. As far as we know, this effective theory has not been used yet for studying the dynamics of MMS with  $N > 2$ .

Furthermore, to the best of our knowledge, the virial approach has not been systematically applied for studying MMS formation and dynamics.

## 5. SPATIOTEMPORAL SOLITON FORMATION IN THE 3D+1 NLSE DESCRIPTION

In this section, we will review the main theoretical results on the formation and stability of spatiotemporal solitons, hereafter

STSs, in GIMF. These states, also known as light bullets [17], form due to a double balance between Kerr nonlinearity and the simultaneous effect of spatial diffraction and chromatic dispersion [5]. In the following, we will focus on the variational formulation as the main tool for obtaining some analytical insight into the properties of these states. Unless stated differently, here we will focus on spatiotemporal spinningless solitons, which bifurcate from the fundamental LG<sub>0</sub> (i.e., Gaussian) spatial mode, as done in the original works [20,27,28,31,87].

### A. 3D+1 Nonlinear Schrödinger Equation

An alternative approach for characterizing the formation and dynamics of MMS considers a 3D+1 NLSE:

$$\begin{aligned} \partial_z E = & \frac{i}{2k_0} \nabla_{\perp}^2 E - i \frac{k_0 \Delta n}{R^2} (x^2 + y^2) E - i \frac{\beta_2}{2} \partial_t^2 E \\ & + i \frac{k_0 n_2}{n_{co}} |E|^2 E, \end{aligned} \quad (94)$$

where  $k_0 = \omega_0 n_{co}/c$ ,  $\Delta n \equiv (n_{co}^2 - n_{cl}^2)/(2n_{co}^2)$ ,  $R$  is the core radius,  $E = E(x, y, t, z)$  is the electric field component of the wave propagating along the  $z$ -direction,  $\nabla_{\perp}^2 \equiv \partial_x^2 + \partial_y^2$  represents diffraction,  $\partial_t^2$  represents the group-velocity dispersion with its strength  $\beta_2$ , and  $x^2 + y^2$  is the 2D parabolic potential describing the transverse spatial profile of the linear refractive index of the fiber [5].

By making the scaling transformations

$$E = e_c u, \quad t = t_c t', \quad (x, y) = w_c (x', y'), \quad z = z_c z',$$

with

$$\begin{aligned} e_c^2 & \equiv \frac{\sqrt{2|\Delta n|} n_{co}}{R k_0 |n_2|}, & t_c^2 & \equiv R |\beta_2| \sqrt{2/|\Delta n|}, \\ w_c^4 & \equiv \frac{R^2}{2k_0^2 |\Delta n|}, & z_c^2 & \equiv \frac{R}{2|\Delta n|}, \end{aligned}$$

the previous equation becomes

$$\partial_z u = \frac{i}{2} \nabla_{\perp}^2 u + i \frac{d_2}{2} \partial_t^2 u + i \frac{\rho}{2} (x^2 + y^2) u + i \nu |u|^2 u, \quad (95)$$

where we have dropped the (') from all the dimensionless variables. Here  $d_2 \equiv \text{sign}(\beta_2) = \pm 1$ , for anomalous/normal dispersion,  $\nu \equiv \text{sign}(n_2) = \pm 1$ , and  $\rho \equiv \text{sign}(\Delta)$ , with  $\rho = -1$  ( $\rho = 1$ ) being chosen for guiding (antiguinding) materials.

Note that this equation can also be used in the context of BECs, in order to describe nearly 1D condensates, with a cigar-shaped trapping potential ( $\rho < 0$ ) if we exchange the  $z$  coordinate with  $t$ . In this context,  $\nu = 1$  models a self-attractive nonlinearity [15]. In the context of BECs, Eq. (95) is commonly referred to as the Gross-Pitaevskii equation [5].

Equation (95) possesses the Lagrangian density [20,28]

$$\begin{aligned} \mathcal{L} = & -\frac{1}{2} (|u_x|^2 + |u_y|^2) - \frac{d_2}{2} |u_t|^2 + \frac{\rho}{2} (x^2 + y^2) |u|^2 \\ & + \frac{\nu}{2} |u|^4 + \frac{i}{2} (u^* u_z - u u_z^*), \end{aligned} \quad (96)$$

which contains all the relevant information about the system dynamics, including its conservation laws [77]. Indeed, from the Lagrangian density one recovers Eq. (95) from the Euler-Lagrange equations [20]

$$\frac{\partial}{\partial z} \left( \frac{\partial \mathcal{L}}{\partial u_z^*} \right) + \frac{\partial}{\partial t} \left( \frac{\partial \mathcal{L}}{\partial u_t^*} \right) + \frac{\partial}{\partial x} \left( \frac{\partial \mathcal{L}}{\partial u_x^*} \right) + \frac{\partial}{\partial y} \left( \frac{\partial \mathcal{L}}{\partial u_y^*} \right) - \frac{\partial \mathcal{L}}{\partial u^*} = 0. \quad (97)$$

Here, the Hamiltonian density reads

$$\mathcal{H} = \frac{1}{2} (|u_x|^2 + |u_y|^2) + \frac{d_2}{2} |u_t|^2 - \frac{\nu}{2} |u|^4 - \frac{\rho}{2} (x^2 + y^2) |u|^2. \quad (98)$$

Note that an alternative way for deriving Eq. (95) can rely on this functional.

### B. Shape-Preserving Spatiotemporal Spinningless Solitons

Here we will focus on studying shape-preserving STSs in the absence of vorticity [15]. Vortex solitons in the context of cigar-shaped Bose–Einstein condensates, which is equivalent to our case, have been investigated by Malomed *et al.* in Ref. [88]. Thus, we expect these vortex states will be present in our optical scenario.

The shape preserving spatiotemporal states of Eq. (95) can be written in the form  $u(x, y, z, t) = v(x, y, t) e^{i\kappa z}$ , where  $\kappa$  is the propagation constant, and  $v(x, y, t)$  is a real-valued function, describing the steady-state field [5,15]. When applied to Eq. (95), this transformation leads to the  $z$ -independent (real) partial differential equation

$$\frac{1}{2} \nabla_{\perp}^2 v + \frac{d_2}{2} v_t + \frac{\rho}{2} (x^2 + y^2) v + \nu v^3 - \kappa v = 0. \quad (99)$$

Similarly to the previous case, the  $z$ -independent Eq. (99) can be derived from the steady-state Lagrangian density

$$\mathcal{L}_s \equiv -\frac{d_2}{4} v_t^2 - \frac{1}{4} (v_x^2 + v_y^2) + \frac{\rho}{4} (x^2 + y^2) v^2 + \frac{\nu}{4} v^4 - \frac{\kappa}{2} v^2, \quad (100)$$

which can also be derived from Eq. (96) by the application of the previous scaling transformation. This new Lagrangian [Eq. (100)] depends explicitly on  $\kappa$ , in contrast to the Lagrangian density Eq. (96).

#### 1. Ritz Optimization through the Variational Approach

At this stage, we will apply the Ritz-optimization method for finding steady-state STS solutions of Eq. (99). This method, extensively used in the soliton literature [15], is equivalent to the Kantarovich approach that we have described in Section 5.B: the only difference is that now the solution ansatz parameters do not depend on  $z$ , i.e., they remain constant upon propagation.

An essential task before continuing is to define a proper ansatz for capturing the main features of these states. The selection of an ansatz is not entirely arbitrary, but it is justified by different preliminary observations, mostly related to the symmetries of the system. For example, in the absence of a 2D parabolic potential ( $\rho \neq 0$ ) or with radially symmetric potentials, Eq. (95) may have radially symmetric 3D solitons, whose shape can be captured by just considering the radius  $r^2 = t^2 + x^2 + y^2$  as the only independent variable of the system [89,90]. However, in our current case, the potential is 2D, and the  $r$ -dependent ansatz is not valid.

Most of the analytical works on the formation of STSs based on the variational approach have focused on spinningless solitons whose spatial shape is mainly based on a single mode: the fundamental LG mode (LG<sub>0</sub>), which has a Gaussian profile [20,27,28,91].

An appropriate ansatz for the spinningless solitons that we are considering has the form

$$v(x, y, t; \bar{w}_t, w_s, A) = A \operatorname{sech}(\bar{w}_t t) \mathcal{G}(x, y; w_s), \quad (101)$$

with the Gaussian profile

$$\mathcal{G}(x, y; w_s) \equiv \exp\left(-\frac{x^2 + y^2}{2w_s^2}\right)$$

of width  $w_s > 0$ ,  $\bar{w}_t$  is the inverse of the temporal width  $w_t > 0$  (i.e.,  $\bar{w}_t = 1/w_t$ ), and  $A > 0$  is the amplitude of the pulse. The justification of the temporal shape of this ansatz is based on the observation that, in the absence of diffraction and spatial potential, Eq. (95) possesses a sech-shape bright soliton solution in the anomalous GVD regime [5]. Solitons with this shape could also be analyzed by just considering a spatiotemporal Gaussian ansatz, which makes the calculations simpler. This approach was followed by Shtyrina *et al.* in Ref. [91].

By using the definition of the pulse energy

$$\mathcal{E} \equiv \iiint_{-\infty}^{\infty} |u(x, y, t)|^2 dx dy dt,$$

we obtain that

$$A = \sqrt{\frac{\mathcal{E}}{2\pi w_t w_s^2}},$$

and we can make our ansatz [i.e., Eq. (101)] energy-dependent. In this way, the pulse energy becomes the most important control parameter for the STS solutions. Thus, the main parameters of the system are  $\{w_t, \bar{w}_s, \mathcal{E}\}$ .

With this ansatz, the static effective Lagrangian

$$L_s(\bar{w}_t, w_s, \mathcal{E}, \kappa) = \int_{\mathbb{R}^3} \mathcal{L}_s[u(x, y, t; \bar{w}_t, w_s, \mathcal{E}, \kappa); d_2, \nu, \rho] dx dy dt$$

reduces to

$$L_s = \frac{\mathcal{E}}{12} \left[ \frac{1}{w_s^2} \left( \frac{\mathcal{E} \nu \bar{w}_t}{2\pi} - 3 \right) - d_2 \bar{w}_t^2 - 6\kappa + 3\rho w_s^4 \right]. \quad (102)$$

Moreover, the effective Euler-Lagrange Eq. (60) becomes

$$\frac{\partial L_s}{\partial \bar{w}_t} = 0, \quad \frac{\partial L_s}{\partial w_s} = 0, \quad \frac{\partial L_s}{\partial \mathcal{E}} = 0. \quad (103)$$

By combining these expressions, we obtain that the shape-preserving soliton parameters satisfy [20]

$$\mathcal{E} = 2\pi w_s \sqrt{6d_2(1 + \rho w_s^4)}, \quad (104)$$

$$w_t^{-1} = \bar{w}_t = \frac{\mathcal{E} \nu}{4\pi d_2 w_s^2} = \frac{\nu}{2d_2 w_s} \sqrt{6d_2(1 + \rho w_s^4)}, \quad (105)$$

whereas the propagation constant reads as

$$\kappa = \frac{1}{4} \left( 5\rho w_s^2 + \frac{1}{w_s^2} \right). \quad (106)$$

Note that all of the previous quantities are parameterized by the spatial width coefficient  $w_s$ .

Besides, the soliton parameters allow us to compute the peak soliton intensity (i.e., the intensity at the center of the STS) as

$$I_{\text{peak}} = |A|^2 = \frac{\mathcal{E} \bar{w}_t}{2\pi w_s^2} = \frac{3}{\nu w_s^2} (1 + \rho w_s^4). \quad (107)$$

At this stage, we can already obtain some general insights about our system. From Eqs. (104) and (105) we find that, in order to obtain real solutions, it is required that  $d_2(1 + \rho w_s^4) > 0$ . Furthermore, from Eq. (105) we see that  $d_2$  and  $\nu$  must have the same sign, in order for  $\bar{w}_t$  to be positive. This last condition yields two regimes, which correspond to the cases of anomalous-self-defocusing ( $d_2, \nu$ ) = (1, 1) regime, and normal GVD-self-focusing ( $d_2, \nu$ ) = (-1, -1) regime, respectively. Figure 15 shows the modifications of  $w_s, \bar{w}_t$  and  $I_{\text{peak}}$  with  $\mathcal{E}$  for the former (in red) and the latter (in blue) scenarios.

Continuing with the examination of Eqs. (104) and (105), we can also see that when  $1 + \rho w_s^4 = 0$  (i.e., if  $w_s^4 = -1/\rho$ ),  $\mathcal{E}$  and  $\bar{w}_t$  become zero. This means that, with  $\mathcal{E} \rightarrow 0$ , the temporal width of the state  $w_t \rightarrow \infty$ , and the STS becomes the continuous-wave (CW) state of the system, which corresponds to the fundamental Gaussian LG<sub>0</sub> mode with  $w_s = 1$  (see black horizontal line in Fig. 15). In other words, STSs in both regimes bifurcate from the fundamental LG<sub>0</sub> mode when  $\mathcal{E} = 0$ . This means that  $\mathcal{E} \rightarrow 0$ , STSs are basically singlemode based. When increasing  $\mathcal{E}$ , however, STSs separate from the LG<sub>0</sub> state and its multimode composition increases. In what follows, we will consider guiding media, and therefore we shall take  $\rho < 0$ .

Equation (104) can also be written in the form

$$\rho w_s^6 + w_s^2 - \frac{1}{6d_2} \left( \frac{\mathcal{E}}{2\pi} \right)^2 = 0, \quad (108)$$

or in terms of  $\bar{w}_t$  as

$$\mathcal{E} \bar{w}_t^3 - 6\pi \bar{w}_t^2 - \frac{3\rho \mathcal{E}^2}{8\pi} = 0, \quad (109)$$

and they may have either one or two positive real roots, depending on the signs of  $\nu, d_2$ , and  $\rho$ . Unfortunately, this equation, in general, does not possess exact analytical solutions, and we need to solve it either by using approximate analytical methods, or numerically. However, for  $\mathcal{E} \ll 1$ , i.e., very close to the CW where the STS is basically singlemode, one can use the approximation [28]

$$\bar{w}_t \approx \frac{\mathcal{E}}{4\pi}, \quad w_s \approx 1. \quad (110)$$

Let us discuss briefly these two regimes.

• **Anomalous GVD-self-focusing regime.** This scenario was initially analyzed by Yu *et al.* in Ref. [27]. In this regime, Eq. (108) has, for a fixed value of  $\mathcal{E}$ , two real solutions, which correspond to the solution branches  $\mathcal{B}_s$  (solid red line) and  $\mathcal{B}_u$  (dashed red line), respectively (see the red dot in Fig. 15). While  $\mathcal{B}_s$  is neutrally stable,  $\mathcal{B}_u$  is unstable [20]. These two solution branches coexist between  $\mathcal{E} = \mathcal{E}_0 \equiv 0$  and the fold,

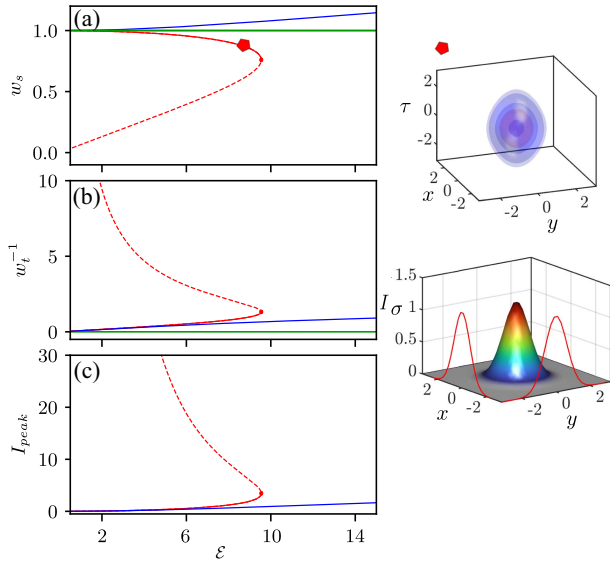


**Fig. 15.** Bifurcation diagrams for STS states as a function of  $\mathcal{E}$  for the anomalous (in red) and normal (in blue) GVD regimes. The green line represents the CW state of the system. (a) shows the spatial width  $w_s$  of the STS as a function of  $\mathcal{E}$ ; (b) shows the inverse of the temporal width  $\tilde{w}_t = w_t^{-1}$ ; (c) represents the STS peak intensity  $I_{\text{peak}}$ . Unstable states are represented with dashed lines, while neutrally stable by solid lines. The horizontal black line corresponds to the fundamental  $\text{LG}_0$  mode. The right column shows an example of the STS solution by using three isosurfaces at different intensities (top), and a cross-section of the same state at constant  $t$ . Adapted from Ref. [20].

or turning point, taking place at  $\mathcal{E} = \mathcal{E}_f$ . The fold position can be calculated analytically, by solving the equation  $d\mathcal{E}/dw_s = 0$ , which leads to  $1 + 3\rho w_s^4 = 0$ , providing that  $1 + \rho w_s^4 > 0$ . The solution of this equation yields the fold parameters

$$w_s^f = (-3\rho)^{-1/4}, \quad \tilde{w}_t^f = (-3\rho)^{1/4}, \quad (111)$$

$$\mathcal{E}_f = 4\pi w_s^f, \quad I_f = \frac{2}{(w_s^f)^2}. \quad (112)$$

• **Normal GVD-self-defocusing regime.** This scenario was partially analyzed by Raghavan and Agrawal in Ref. [28]. In this regime, Eq. (108) has a single real solution, and the solution ansatz parameters are single-valued in  $\mathcal{E}$ . Thus, here there exists just a single STS for any fixed value of  $\mathcal{E}$ . In contrast with the anomalous GVD/self-focusing case, we can see that for the same energy interval, the STS is spatially wider, thinner in time and possesses a lower peak intensity (see Fig. 15).

## 2. Vakhitov-Kolokolov Stability Criterion

The stability of STSs can be estimated by applying different criteria to the reduced equations for the parameters [20]. With the information that we have so far, we may apply the Vakhitov-Kolokolov stability (VKS) criterion [5,92], which relies on the propagation constant  $\kappa$  dependence with  $\mathcal{E}$  [see Eq. (106)]. This dependence is graphically illustrated in Fig. 16(a) for the anomalous dispersion regime. The VKS criterion establishes that an STS state is linearly stable (i.e., with respect to small perturbations), if the derivative of the energy

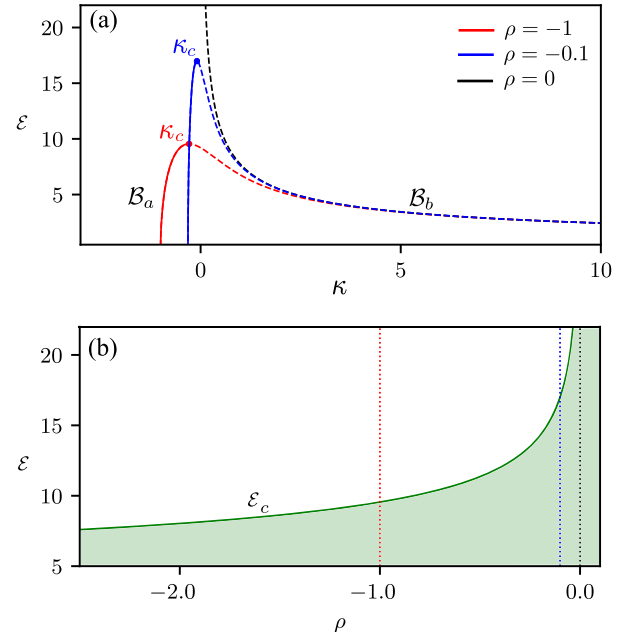


**Fig. 16.** (a) Dependence of the energy  $\mathcal{E}$  on  $\kappa$  for different values of  $\rho$  in the anomalous GVD regime. Stable (unstable) branches are plotted by using solid (dashed) lines. (b) Region of existence of STSs as a function of  $\rho$  (see green shadowed area). The line limiting that area is  $\mathcal{E} = \mathcal{E}_c$ . Vertical dashed lines correspond to the three cases plotted in (a). Adapted from Ref. [20].

with respect to  $\kappa$  is a positive quantity (i.e.,  $d\mathcal{E}/d\kappa > 0$ ), and unstable otherwise. The main idea behind this criterion is based on the analysis of the properties of the linear operator associated with Eq. (95), evaluated on the soliton solution. We recommend the interested reader to consult Section 2.3 in Ref. [5] for details.

The red curve in Fig. 16(a) corresponds to  $\rho = -1$ , the same case that we have studied in the previous section [see red curves in Figs. 15(a)–15(c)]. This criterion shows that  $\mathcal{B}_s$  is stable (see solid line), while  $\mathcal{B}_u$  is unstable (see dashed line). The instability threshold  $\kappa_c$  occurs whenever  $d\mathcal{E}/d\kappa|_{\kappa_c} = 0$ , which leads to

$$\kappa_c = \frac{1}{4} \left( \frac{5\rho}{\sqrt{-3\rho}} + \sqrt{-3\rho} \right), \quad \mathcal{E}_c = \frac{4\pi}{(-3\rho)^{1/4}}. \quad (113)$$

This point corresponds to the fold occurring at  $\mathcal{E}_f$ : in the following, we shall write  $(\kappa_c, \mathcal{E}_c) = (\kappa_f, \mathcal{E}_f)$ . This point is marked by means of a red bullet in Fig. 16(a).

Let us briefly study how the STS stability is impacted by the parabolic potential. To do so, in Fig. 16(a) we plot the modification  $\kappa$  for the other two characteristic values of  $\rho$ : specifically,  $\rho = -0.1$  (in blue) and  $\rho = 0$  (in black). By increasing  $\rho$ , the region of existence of STSs broadens, as the critical point  $(\mathcal{E}, \mu) = (\mathcal{E}_c, \kappa_c)$  moves towards higher values of  $\mathcal{E}$ . The dependence of  $\mathcal{E}_c$  upon  $\rho$  is shown in Fig. 16(b). Here, the green shadowed area corresponds to the region of existence of STSs. For  $\rho = 0$ , only the branch  $\mathcal{B}_u$  survives, and STSs are always unstable. These results show that the presence of a non-vanishing parabolic potential is essential for the stabilization of STSs. This description was already present in the work of Shtyrina *et al.* [91].

### C. Kantarovitch Optimization Method in the Lagrangian and Hamiltonian Formalism

In the previous section, we have focused on the self-preserving  $z$ -independent states. However, a description of the propagation of STSs can be also obtained by considering the Kantarovitch approach, where the ansatz parameters are allowed to depend on  $z$ . This was the approach originally used by Yu *et al.* [27], and Raghavan and Agrawal [28].

Our new ansatz is a product of the static one [see Eq. (101)] and a spacetime-dependent phase contribution, namely,

$$u(z, x, y, t) \equiv v \cdot \exp(i\psi[x, y, t]), \quad (114)$$

with

$$\psi[x, y, t] \equiv t^2\theta(z) + (x^2 + y^2)\alpha(z) + \phi(z),$$

where  $\alpha$  represents the spatial chirp,  $\theta$  the temporal chirp, and  $\phi$  the phase. This ansatz leads to the effective  $z$ -dependent Lagrangian

$$L(z) = -\mathcal{E} \left( \frac{d\phi}{dz} + \frac{\pi^2}{12\bar{w}_t^2} \frac{d\theta}{dz} + w_s^2 \frac{d\alpha}{dz} + \frac{d_2}{6} \bar{w}_t^2 + \frac{\pi^2 d_2 \theta^2}{6\bar{w}_t^2} \right) - \mathcal{E} \left[ (4\alpha^2 - \rho) \frac{w_s^2}{2} + \frac{1}{2w_s^2} \left( 1 - \frac{\nu\mathcal{E}\bar{w}_t}{6\pi} \right) \right]. \quad (115)$$

In this case, the Euler-Lagrange Eq. (60) becomes the 4D dynamical system

$$\frac{d\bar{w}_t}{dz} = f_1 \equiv -2d_2\bar{w}_t\theta, \quad (116a)$$

$$\frac{dw_s}{dz} = f_2 \equiv 2w_s\alpha, \quad (116b)$$

$$\frac{d\theta}{dz} = f_3 \equiv 2d_2 \left( \frac{\bar{w}_t^4}{\pi^2} - \theta^2 \right) - \frac{\mathcal{E}\nu\bar{w}_t^3}{2\pi^3 w_s^2}, \quad (116c)$$

$$\frac{d\alpha}{dz} = f_4 \equiv \frac{1}{2w_s^4} \left( 1 - \frac{\nu\bar{w}_t\mathcal{E}}{6\pi} \right) + \frac{\rho}{2} - 2\alpha^2. \quad (116d)$$

Note that the equilibria, or fixed points, of this system lead to the same set of Eqs. (104)–(106). Besides, the system Eq. (116) provides information about the propagation behavior and spectral stability of the STS, which was not provided by the shape-preserving analysis carried out in Section 5.B.1. The transient and permanent dynamics of STSs by using this set of equations were investigated in Refs. [20,27,28].

Alternatively, the Kantarovitch approach can be also applied in the framework of the Hamiltonian formalism. In this regard, the reduced Hamiltonian

$$H = \mathcal{E} \left[ \frac{d_2\bar{w}_t^2}{6} + \frac{\pi^2 d_2 \theta^2}{6\bar{w}_t^2} + \frac{w_s^2}{2} (4\alpha^2 - \rho) + \frac{1}{2w_s^2} \left( 1 - \frac{\mathcal{E}\nu\bar{w}_t}{6\pi} \right) \right],$$

can be retrieved from the density Eq. (98) and the chirp-dependent ansatz Eq. (114), as discussed in Section 5.B.

The Hamiltonian Eq. (62) then yields the same system of Eq. (116). A detailed study of our system by using this approach can be found in the work by Parra-Rivas *et al.* [31].

#### 1. Spectral Linear Stability and Types of Equilibria

As previously mentioned, Eq. (116) provides information about the STS spectral stability. For obtaining this information we may perform a linear stability analysis of the system Eq. (116) about the equilibria  $q_e = (w_s^e, \bar{w}_t^e, 0, 0)$ . This analysis allows us to determine how the equilibria of the system react against perturbations of the form  $q = q_e + \epsilon\tilde{q}$ , where  $\epsilon \ll 1$  and  $\tilde{q} \equiv (\tilde{w}_s, \tilde{w}_t, \tilde{\theta}, \tilde{\alpha})$ . This, moreover, allows for their classification according to their behavior.

Very close to a fixed point  $q_e$ , the dynamics of the system Eq. (116) are captured by the linear dynamical system

$$\frac{d\tilde{q}}{dz} = \mathcal{J}[q_e]\tilde{q}, \quad (117)$$

where  $\mathcal{J}[q_e]$  is the Jacobian matrix of the vector field  $f$  [see Eq. (116)], which is defined by its components as follows:

$$\mathcal{J}[q_e]_{(i,j)} \equiv \mathcal{D}f_{(i,j)}(q_e) = \left( \frac{\partial f_i}{\partial q_j} \right) (q_e). \quad (118)$$

In our case, the Jacobian matrix becomes

$$\mathcal{J}[q_e] \equiv \begin{bmatrix} 0 & 0 & -2d_2\bar{w}_t^e & 0 \\ 0 & 0 & 0 & 2w_s^e \\ \mathcal{J}_{31} & \frac{\mathcal{E}\nu(\bar{w}_t^e)^3}{\pi^3(w_s^e)^3} & 0 & 0 \\ -\frac{\nu\mathcal{E}}{12\pi(w_s^e)^4} & \mathcal{J}_{42} & 0 & 0 \end{bmatrix}, \quad (119)$$

with

$$\mathcal{J}_{31} \equiv \left[ 8d_2\bar{w}_t^e - \frac{3}{2} \frac{\mathcal{E}\nu}{\pi(w_s^e)^2} \right] \frac{(\bar{w}_t^e)^2}{\pi^2}, \quad (120)$$

$$\mathcal{J}_{42} \equiv \frac{2}{(w_s^e)^5} \left( \frac{\nu\mathcal{E}\bar{w}_t^e}{6\pi} - 1 \right). \quad (121)$$

The stability of the steady STS can be evaluated by solving the linear eigenvalue problem

$$\mathcal{J}w = \lambda w, \quad (122)$$

where  $\lambda$  and  $w$  are the eigenvalue and eigenvector associated with  $\mathcal{J}$ , respectively. The eigenvalues satisfy the bi-quadratic characteristic polynomial

$$\lambda^4 + c_2\lambda^2 + c_0 = 0, \quad (123)$$

with the coefficients  $c_2 \equiv 2(d_2\bar{w}_t^e\mathcal{J}_{31} - w_s^e\mathcal{J}_{42})$ , and

$$c_0 \equiv -d_2 \left[ 4w_s^e\bar{w}_t^e\mathcal{J}_{31}\mathcal{J}_{42} + \frac{\mathcal{E}^2\bar{w}_t^4}{3\pi^4(w_s^e)^6} \right]. \quad (124)$$

Figure 17 shows the modification of the eigenspectrum associated with stable STSs on  $\mathcal{B}_s$  and unstable STSs on  $\mathcal{B}_s$  in the  $\mathcal{E}$  versus  $\kappa$  diagram in the anomalous GVD regime.

In  $\mathcal{B}_s$ , the spectrum consists of four pure imaginary eigenvalues  $\sigma = \{\lambda_A, \lambda_B\} = \{\pm i\omega_A, \pm i\omega_B\}$ , with  $\omega_A > \omega_B > 0$ . A fixed point with these eigenvalues is known as a center [20]. Center points are neutrally stable, in the sense that nearby trajectories (i.e., soliton parameter perturbations) are neither



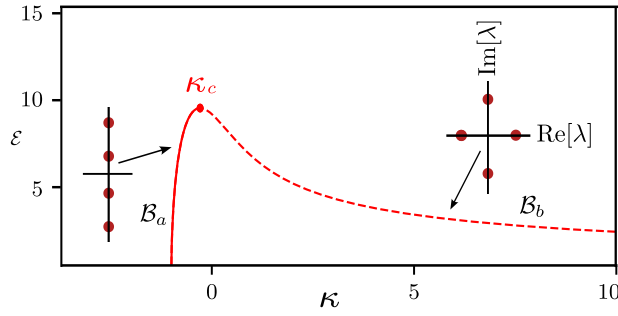


**Fig. 17.** Distribution of the eigenvalues associated with the dynamical system Eq. (116) in the anomalous GVD regime. Adapted from Ref. [20].

repelled nor attracted to it, but they undergo permanent oscillations. To the lowest order in  $\mathcal{E}$ , these four eigenvalues can be approximated by [28]

$$\lambda_A \approx \pm i \left( 4 + \frac{\mathcal{E}^2}{2\pi^2} \right)^{1/2} \equiv \pm i\omega_A, \quad (125a)$$

$$\lambda_B \approx \pm i \frac{\mathcal{E}^2}{4\sqrt{2}\pi^3} \equiv \pm i\omega_B. \quad (125b)$$

Further examination of the eigenvectors associated with these frequencies shows that parameters  $w_s$  and  $\alpha$  oscillate at the higher frequency  $\omega_A$ , while  $w_t$  and  $\theta$  oscillate according to  $\omega_B$ . These two oscillations lead to quasiperiodic oscillations [82], analogous to those predicted for the case of two-mode solitons (see Section 4.C). A numerical study of Eq. (116) regarding this oscillatory regime can be found in Refs. [20,28]. The eigenspectra for STSs on  $\mathcal{B}_w$ , in contrast, correspond to two pure imaginary and two pure real eigenvalues, namely, with  $\sigma = \{\pm\lambda_C, \pm i\lambda_D\}$ . In this case, the associated equilibria are known as saddle-centers, and are unstable [20].

#### D. Numerical Confirmation through 3D+1 Simulations

Let us see how the effective theory developed in the previous section matches with the results obtained by solving our original Eq. (95). Here we will only review the results regarding the anomalous GVD regime. We recommend the interested reader to take a look at Ref. [20] for further details.

To solve this initial value problem, we consider as the initial condition the approximate analytical STS solution of Eq. (101), together with Eqs. (128a) and (128b). The  $z$ -evolution of the initial stable chirp-free STS solution is shown in Figs. 18(a)–18(c) for  $\mathcal{E} = 6$ . In both cases, the top and middle panels compare the  $z$ -evolution of the STS intensity at its center (blue curve), with the analytically predicted intensity value. As we can see, the evolution of the STS intensity is not constant, but it fluctuates around a value that is slightly larger than what is predicted by the analytical theory. We could understand this, if we remember the STS is a center equilibrium: therefore, it is neutrally stable, which means that even numerical noise may perturb such equilibrium, leading to quasiperiodic oscillations.

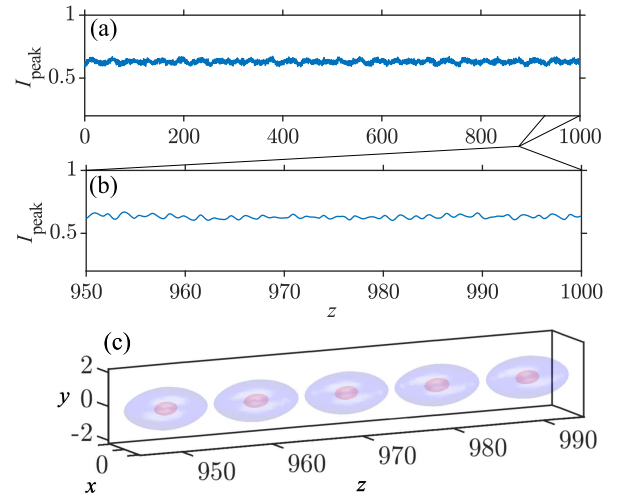


**Fig. 18.** Evolution with distance  $z$  of a stable STS for  $\mathcal{E} = 6$  [see (a)–(c)]. Panel (a) shows the variation of the peak STS intensity versus the propagation distance. Panel (b) shows a close-up view of (a) for the interval  $z \in [950, 1000]$ . Panel (c) shows the evolution of the STS along the interval shown in (b), obtained by plotting two isosurfaces at  $I_1 = 0.5$  (red) and  $I_2 = 0.1$  (blue). The dashed gray straight line in (a) and (b) represents the theoretical value of the STS intensity. Adapted from Ref. [20].

Our simulations reveal the presence of fast, small amplitude intensity fluctuations as shown in Figs. 18(a) and 18(b). This behavior agrees with that obtained when studying the effective reduced system Eq. (116) [20]. These intensity fluctuations are depicted in more detail in Fig. 18(b) for the reduced interval  $z \in (950, 1000)$ . The shape evolution of the STS in such an interval is illustrated in Fig. 18(c) by considering two isosurfaces at intensities  $I_1 = 0.5$  and  $I_2 = 0.1$ , respectively.

The discrepancy between the analytically-obtained stable STS and numerical results becomes larger when we increase STS energy. In Fig. 19(a) we compare the center intensity of STS obtained from the effective theory (in orange) and from numerical simulations in the interval  $z \in (0, 1000)$  (blue circles). The blue circles and the error bars represent the time-averaged intensity values and the corresponding standard deviation for stable states. For low values of  $\mathcal{E}$ , the agreement is quite good, but it worsens with increasing  $\mathcal{E}$ . Eventually, for energy values above  $\mathcal{E} \approx 8.5$  the system undergoes full wave collapse. This region is illustrated by using a red-shaded box. This collapse occurs much earlier than the analytical existence limit predicted by the theory at  $\mathcal{E} = E_f$ .

An example of such destructive dynamics is illustrated in Figs. 20(a) and 20(b) for  $\mathcal{E} = 9$ . The theoretically stable STS maintains its stability for a very short propagation length, but eventually, at  $z \approx 3.5$ , it undergoes wave collapse. This is characterized by a very fast growth rate of the peak intensity. This concentration of the field intensity at the center of the state can also be observed in the STS shell evolution which is shown in Fig. 20(b).

The disagreement between theory and numerical results, which to our knowledge was not disclosed in earlier works, might be corrected by considering higher-order self-defocusing

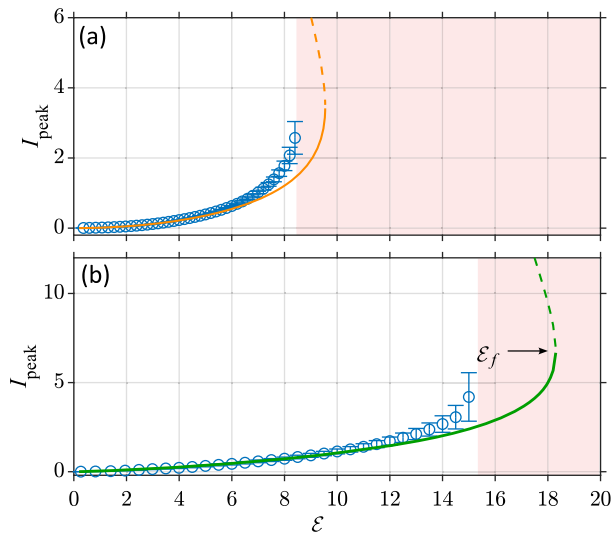


**Fig. 19.** Panels (a) and (b) show the evolution of peak intensity of stable STS with energy  $\mathcal{E}$  for the pure quadratic and pure quartic dispersion scenarios, respectively. In (a), the green line shows the analytical values, while the blue circles and the error bars represent the average intensity values and the standard deviation for stable states. Adapted from Ref. [87].

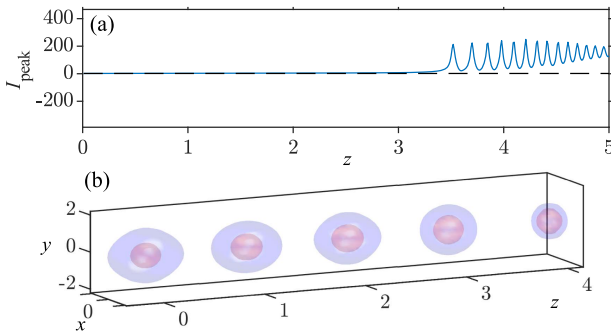


**Fig. 20.** Wave collapse started from an STS for  $\mathcal{E} = 9$ . Panel (a) shows the evolution of the  $I_{\text{peak}}$ , while panel (b) shows the modification of the STS with the propagation.

nonlinearities (e.g., quintic-order nonlinear terms), or high-order dispersive effects.

### E. Stabilization through High-Order Dispersion Effects

At this point, the interesting question arises about what potential mechanism could be exploited for arresting, fully or partially, the wave collapse that we discussed in the previous section. It has been demonstrated before that high-order dispersion effects impact positively soliton stabilization in both conservative and dissipative systems [93–100]. Inspired by these works, Parra-Rivas *et al.* proposed pure quartic chromatic dispersion as a main stabilization mechanism [87]. In this section we review these results, by showing that pure quartic dispersion is able to increase considerably the stability range of STSs, far beyond the limit that is obtained in the case of pure quadratic dispersion, thus delaying the occurrence of wave collapse.

In the presence of pure quartic dispersion, the normalized version of the 3D+1 NLSE reads

$$\partial_z u = \frac{i}{2} \nabla_{\perp}^2 u + id_4 \partial_t^4 u + i \frac{\rho}{2} (x^2 + y^2) u + i\nu |u|^2 u, \quad (126)$$

with  $d_4 = \text{sign}(\beta_4) = \pm 1$ , with  $\beta_4$  being the quartic dispersion coefficient [87]. All other parameters are defined as in Eq. (95). In this case, the Lagrangian density reads as

$$\begin{aligned} \mathcal{L} = & -\frac{1}{2} (|u_x|^2 + |u_y|^2) - d_4 |u_{tt}|^2 + \frac{\rho}{2} (x^2 + y^2) |u|^2 \\ & + \frac{\nu}{2} |u|^4 + \frac{i}{2} (u^* u_z - u u_z^*). \end{aligned} \quad (127)$$

By applying the shape-preserving transformation  $u(x, y, z, t) = v(x, y, t) e^{ikz}$  and the STS ansatz Eq. (101), one may compute the effective steady-state Lagrangian

$$L_s = \frac{\mathcal{E}}{30} \left[ -14d_4 \tilde{w}_t^4 - 30 \kappa + \frac{5}{w_s^2} \left( \frac{\mathcal{E} \tilde{w}_t \nu}{2\pi} - 3 \right) + 15\rho w_s^2 \right],$$

which yields, through the Euler-Lagrange equation [see Eq. (103)], the following parameter relations:

$$\frac{5\nu\mathcal{E}}{\pi w_s^2} - 112d_4 \tilde{w}_t^3 = 0, \quad (128a)$$

$$\tilde{w}_t = \frac{6\pi(w_s^4 \rho + 1)}{\nu\mathcal{E}}, \quad (128b)$$

$$\kappa = -\frac{7}{15} d_4 \tilde{w}_t^4 - \frac{1}{2w_s^2} \left( 1 - \frac{\mathcal{E} \tilde{w}_t \nu}{3\pi} \right) + \frac{\rho w_s^2}{2}. \quad (128c)$$

By combining Eqs. (128a) and (128b), we obtain

$$\mathcal{E}^4 = C_1 d_4 \pi^4 w_s^2 (w_s^4 \rho + 1)^3, \quad (129)$$

with  $C_1 = 1008 \times 24/5$ , which relates  $\mathcal{E}$  and  $w_s$ . By inserting Eqs. (129) into Eq. (128b), we find that  $\tilde{w}_t$  is also completely parameterized in terms of the spatial width  $w_s$ .

In the guiding ( $\rho = -1$ ) self-focusing regime ( $\nu = 1$ ) with  $d_4 = 1$ , the system also presents two STSs branches  $\mathcal{B}_u$  and  $\mathcal{B}_s$ , which coexist within the same energy range, extending from  $\mathcal{E} = 0$  up to the fold ( $f$ ) located at  $(\mathcal{E}, w_s) = (\mathcal{E}^f, w_s^f)$ , where in this case

$$w_s^f = (-7\rho)^{-1/4}, \quad \mathcal{E}^f = \left( C_2 \frac{\pi^4 d_4}{\sqrt{-7\rho}} \right)^{1/4}, \quad (130)$$

with  $C_2 = C_1 (6/7)^3$ . This fold marks an upper energy limit, or threshold, for the STS existence.

The modification of the STS peak intensity with energy  $\mathcal{E}$  in this case is illustrated in Fig. 19(b). The comparison between Figs. 19(a) and 19(b) shows that the STS existence region for pure quartic dispersion is  $\Delta\mathcal{E} \approx 8.753$  larger than in the quadratic case. The stability of these states was confirmed by applying the VKS and Lyapunov stability [87] criteria.

In this case, the authors also compare the effective theory and the full numerical simulations by using Eq. (126) [see Fig. 19(b)]. This comparison shows that pure quartic

dispersion significantly delays the appearance of wave collapse, by increasing by more than twice the  $\mathcal{E}$ -range of STS existence. Although engineering an MMF with pure quartic dispersion appears to be challenging, this is relatively straightforward to do in a ring cavity configuration, by using a waveshaper [98].

## 6. REDUCED (1D + 1) NLSE AND GRIN SOLITONS

We saw in Section 5.A that a multidimensional (3D+1) NLSE must be used to study the evolution of short optical pulses inside a GIMF. As numerical solutions of this equation are time consuming, one may ask whether the propagation problem could be simplified in some specific situations. It turns out that this is indeed possible in view of the self-imaging property of a GRIN medium. We have seen in Section 2.C.1 that optical beams in the form of CW evolve inside a GRIN fiber in a periodic fashion with a relatively small period ( $\sim 1$  mm). This feature suggests that we may be able to find multimode solitons that maintain a constant temporal width, but whose spatial width evolves periodically along the length of a GRIN medium. It is important to stress that such temporal solitons are quite different from the spatiotemporal solitons discussed in Section 3 because they maintain a constant spatial width as well.

### A. Effective (1D+1) NLSE

To examine this possibility, we consider a Gaussian beam launched into a GRIN fiber with a planar wavefront with an electric field oscillating at the frequency  $\omega_0$ . In the CW case, the propagation problem can be solved analytically [101], and the electric field associated with the Gaussian beam can be written in the form

$$E_r(\mathbf{r}, t) = \text{Re}\{A_0 F_s(\mathbf{r}) \exp(i\beta_0 z - i\omega_0 t)\}, \quad (131)$$

where  $A_0$  is the initial amplitude of the beam and  $\beta_0 = n(\omega_0)k_0$  is its propagation constant. The function  $F_s(\mathbf{r})$ , governing the spatial self-imaging of the Gaussian beam, is given by

$$F_s(\mathbf{r}) = \exp\left[-\frac{x^2 + y^2}{2w^2(z)} + \frac{i}{2}h(z)(x^2 + y^2) + i\psi(z)\right], \quad (132)$$

where the beam's width  $w(z)$  varies in a periodic fashion as

$$w(z) = w_0[\cos^2(bz) + C_f^2 \sin^2(bz)]^{1/2}. \quad (133)$$

The parameter  $b$ , defined as  $b = \sqrt{2\Delta n}/R$ , is a measure of the index gradient, where  $\Delta n$  represents the refractive index difference between core and cladding, and  $R$  is the core radius. The parameter  $C_f$  is defined as

$$C_f = (w_g/w_0)^2 \sqrt{1-p}, \quad p = \frac{n_2}{2n_0} (\beta_0 A_0 w_0)^2, \quad (134)$$

where  $w_g = (b\beta_0)^{-1/2}$  represents the spot size of the fundamental mode of a GRIN fiber, with a typical value close to  $5 \mu\text{m}$ , and  $n_2$  is the nonlinear index. The phase-front curvature of the beam in Eq. (132) is obtained using  $h(z) = d(\ln w)/dz$ . The phase  $\psi(z)$  also varies periodically but is

not of concern here. The parameter  $p$  includes the effects of self-focusing. In practice, its value is such that  $p \ll 1$ . Notice that only the fundamental mode of the GRIN fiber is excited when the spot size of the incoming Gaussian beam is narrow enough that  $w_0 \approx w_g$ . In this situation, the beam's width does not change with  $z$  because  $C_f$  is close to 1, resulting in  $w(z) = w_0$ .

To apply the CW solution given in Eq. (132) to a pulsed Gaussian beam, we assume that the bandwidth of the pulse is narrow enough that the spatial profile  $F_s(\mathbf{r})$  of the beam is not affected much by the nonlinear effects. This assumption is reasonable because the periodic spatial pattern of the beam in Eq. (133) maintains the same periodicity when  $n_2 > 0$ , and its amplitude is only affected through the  $C_f$  parameter given in Eq. (134). As long as the peak power  $P_0$  of the pulse remains below the self-focusing critical power  $P_c$ , i.e., one has  $p \ll 1$ , the pulsed beam should follow the same periodic self-imaging pattern that a CW beam follows inside a linear GRIN medium. With this approximation, we look for solutions of the (3D+1) NLSE Eq. (94) in the form of Eq. (131) but allow the amplitude  $A_0$  to depend on both  $z$  and  $t$  by using [102]

$$E(x, y, z, t) \approx A(z, t) F_s(\mathbf{r}), \quad (135)$$

where  $A(z, t)$  describes temporal evolution of each pulse within the beam, whose spatial evolution depends on the spatial coordinates  $x$  and  $y$  through the known function  $F_s(\mathbf{r})$  given in Eq. (132). It is important to realize that  $F_s(\mathbf{r})$  does not correspond to any specific mode but can be thought of as a superposition of many modes of a GRIN fiber that are excited by the incident Gaussian beam.

To obtain an equation for  $A(z, t)$ , we follow a well-known procedure [56]. When we substitute Eq. (135) in Eq. (94), we obtain

$$F_s \left( \frac{\partial A}{\partial z} + \frac{i\beta_2}{2} \frac{\partial^2 A}{\partial t^2} - i \frac{\beta_0 n_2}{n_{co}} |F_s|^2 |A|^2 A \right) + A \left[ \frac{\partial F_s}{\partial z} + \frac{\nabla_{\perp}^2 F_s}{2i\beta_0} + \frac{i\beta_0}{2} b^2 (x^2 + y^2) F_s \right] = 0. \quad (136)$$

The expression in the second line vanishes because  $F_s$  is its solution. We multiply Eq. (136) with  $F_s^*$  and integrate over the transverse coordinates  $x$  and  $y$ . The final result can be written as [102]

$$i \frac{\partial A}{\partial z} - \frac{i\beta_2}{2} \frac{\partial^2 A}{\partial t^2} + \tilde{\gamma}(z) |A|^2 A, \quad (137)$$

where  $|A|^2$  has units of power and the effective nonlinear parameter is defined as

$$\tilde{\gamma}(z) = \frac{k_0 n_2}{A_{\text{eff}}(z)}, \quad A_{\text{eff}}(z) = \frac{\left[ \iint_{-\infty}^{\infty} |F_s(\mathbf{r})|^2 dx dy \right]^2}{\iint_{-\infty}^{\infty} |F_s(\mathbf{r})|^4 dx dy}. \quad (138)$$

Physically,  $A_{\text{eff}}(z)$  represents the local effective cross section of the beam, which varies with  $z$  as the Gaussian beam undergoes periodic focusing during each self-imaging cycle.

Equation (137) is remarkable because it has the form of a 1D NLSE with the only difference that its effective nonlinear

parameter  $\tilde{\gamma}(z)$  varies with  $z$ . It shows that the evolution of pulses inside a GRIN fiber can be studied under certain conditions by solving a single 1D NLSE in the time domain, and represents a drastic simplification of the original (3D+1) NLSE given in Eq. (94). According to this equation, periodic oscillations of the spatial width of a pulsed Gaussian beam resulting from self-imaging give rise to an effective nonlinear parameter  $\tilde{\gamma}(z)$ , which is also periodic in  $z$  with the same period  $L_p$  [see their typical values in Fig. 4(a)]. This is not surprising, because the intensity at a given distance  $z$  depends on the beam's width, becoming larger when the beam compresses and smaller as it expands. One can interpret this effect as the formation of a Kerr-induced nonlinear index grating within the GRIN medium. The local refractive index of the medium increases in a periodic fashion only near the focal planes where the beam's intensity is enhanced.

The integrals in Eq. (138) can be carried out using  $F_s(\mathbf{r})$  from Eq. (132). The resulting effective mode area has the form  $A_{\text{eff}}(z) = A_{\text{eff}}(0)f(z)$ , where the periodic function  $f(z)$  is defined as

$$f(z) = \cos^2(bz) + C_f^2 \sin^2(bz). \quad (139)$$

The functional form of  $f(z)$  becomes clear when we note that  $A_{\text{eff}}(z)$  at any location scales with the spatial width as  $w^2(z)$ . We can use this relation to define  $\tilde{\gamma}(z) = \gamma/f(z)$ , where  $\gamma = k_0 n_2 / A_{\text{eff}}(0)$  is its initial value at  $z = 0$ . This step allows us to write Eq. (137) in the form

$$i \frac{\partial A}{\partial z} - \frac{\beta_2}{2} \frac{\partial^2 A}{\partial t^2} + \frac{\gamma}{f(z)} |A|^2 A = 0, \quad (140)$$

which reduces to the standard NLSE when  $f(z) = 1$ . As seen from Eq. (137),  $f(z) = 1$  occurs when  $C_f = 1$ . It turns out that this requirement is met when the width of the incident Gaussian beam is matched to that of the fundamental mode of a GRIN fiber, so that only this mode is excited by the incoming beam.

Similar to the case of singlemode fibers, Eq. (140) needs to be modified for pulses shorter than a few picoseconds [56]. The reason is related to the nature of the nonlinear response of the fiber's material to an electromagnetic field (see Fig. 2 and detailed description in Section 2.B.4). In general, vibrations of silica molecules also produce a nonlinear response, in addition to that of electrons bound to each atom of the molecule. This response, known as the Raman response, is delayed in time, compared to the nearly instantaneous response of electrons, and this delay becomes relevant for short optical pulses. In the case of silica-based GRIN fibers, the Raman response is included by replacing the Kerr-induced index change  $(\Delta n)_{\text{NL}} = n_2 |E|^2$  in Eq. (94) with

$$(\Delta n)_{\text{NL}} = (1 - f_{\text{R}}) n_2 |E|^2 + f_{\text{R}} n_2 \int_0^\infty h_{\text{R}}(t') |E(\mathbf{r}, t - t')|^2 dt', \quad (141)$$

where  $f_{\text{R}}$  represents the fractional contribution of the delayed response and  $h_{\text{R}}(t)$  is the Raman response function of silica molecules, normalized such that  $\int h_{\text{R}}(t) dt = 1$ . Its use in

Eq. (94) leads to the following modified form of the effective NLSE:

$$i \frac{\partial A}{\partial z} + \sum_{n=2}^M \frac{i^n \beta_n}{n!} \frac{\partial^n A}{\partial t^n} + \frac{\gamma}{f(z)} [(1 - f_{\text{R}}) |A|^2 A + f_{\text{R}} \int_0^\infty h_{\text{R}}(t') |A(z, t - t')|^2 dt'] = 0, \quad (142)$$

where the sum includes the second and higher-order dispersion terms in the Taylor expansion of  $\beta(\omega)$ . The spectral width of ultrashort pulses becomes large enough that the contribution of the  $\beta_3$  term may not remain negligible. Often, it is sufficient to consider the first two terms by choosing  $M = 3$ , but the  $\beta_4$  and higher-order terms may also be needed, depending on the situation.

The Raman response  $h_{\text{R}}(t)$  in Eq. (142) affects short pulses through the Raman gain, as detailed in Section 2.B.5. It is worth noting that the functional form of the Raman response  $h_{\text{R}}(t)$  depends on the Raman gain spectrum that has been measured for silica fibers. It is useful in practice to have an approximate analytic form for  $h_{\text{R}}(t)$ . Assuming a single vibrational frequency of silica molecules is involved in the Raman process,  $h_{\text{R}}(t)$  can be approximated as Eq. (31) [103]. Although Eq. (31) is used often in practice, its predictions do not always agree with experiments. For this reason, a modified form of  $h_{\text{R}}(t)$  was proposed in 2006 [104]:

$$h_{\text{R}}^{\text{new}}(t) = (1 - f_b) h_{\text{R}}(t) + f_b [(2\tau_b - t)/\tau_b^2] \exp(-t/\tau_b), \quad (143)$$

where  $f_b = 0.21$  and  $\tau_b = 96$  fs. This form requires  $f_{\text{R}} = 0.245$  and explains better the observed Raman-induced frequency shifts of short optical pulses inside silica fibers.

In the following subsection, we use the 1D NLSE Eq. (140) and its generalized form in Eq. (142) to investigate the formation of multimode solitons inside GRIN fibers. These NLSEs involve only two variables ( $z$  and  $t$ ) and can be solved numerically much faster than the full 3D problem for GRIN fibers involving also the spatial variables  $x$  and  $y$ . They include the effects of periodic self-imaging, occurring invariably inside a GRIN fiber, through the function  $f(z)$  and the two parameters  $C$  and  $z_p$  appearing in its definition in Eq. (139). However, they neglect the impact of temporal dynamics on the spatial features of the beam and cannot be applied under all experimental conditions. It is thus important to summarize the conditions under which the effective 1D NLSE can be used in practice.

- Weakly guiding approximation requiring  $\Delta n \ll 1$  must hold. This approximation is often valid in practice as  $\Delta n < 0.01$  for most GRIN fibers.

- The core size of the GRIN fiber must be large enough for it to support a large number of modes. As the core radius exceeds 20  $\mu\text{m}$  for most GRIN fibers, this is often the case in practice.

- The spatial width of the input beam must be smaller than the core diameter but still large enough that many low-order modes are excited simultaneously.

- The spectral bandwidth of pulses must be narrow enough, so that the spatial cross section of the optical beam does not

change much over its entire range at any point within the GRIN fiber.

- The preceding situation is possible only for multicycle input pulses. Even a femtosecond pulse should be wide enough to contain ten or more optical cycles within its temporal envelope.

Under such conditions, spatial width variations of an optical beam caused by the self-imaging phenomenon affect its temporal evolution but the reverse does not occur, i.e., temporal field profile changes have no effect on the spatial evolution of the optical beam.

### B. Temporal Solitons with Spatial Self-Imaging

The NLSE Eq. (140) differs from the standard NLSE because the effective nonlinear parameter  $\gamma/f(z)$  is not constant but varies in a periodic fashion. The presence of  $f(z)$  in this equation indicates that it is not integrable by the inverse scattering method. As a result, it is not expected that this equation would have solutions in the form of ideal solitons that propagate without any change in their shape, or evolve in a periodic fashion while preserving their energy over long distances. Nevertheless, it may support, under certain conditions, the soliton-like evolution of an optical pulse such that its energy is nearly preserved over considerable lengths of GRIN fibers. Indeed, an equation similar to Eq. (140) also occurs in the context of singlemode fiber links employing periodically spaced optical amplifiers for compensating fiber's losses. It was found in 1990 that a new kind of soliton, called the guiding-center soliton, can form in such fiber links [105]. It is also known as the loss-managed soliton [106].

To find the conditions under which soliton formation is possible inside a GRIN fiber, we solve Eq. (140) numerically with the split-step Fourier method [56]. For this purpose, it is useful to normalize this equation using the variables

$$\tau = t/T_0, \quad \xi = z/L_D, \quad U = A/\sqrt{P_0}, \quad (144)$$

where  $T_0$  and  $P_0$  are the width and the peak power of input pulses, and  $L_D = T_0^2/|\beta_2|$  is the dispersion length. The resulting equation takes the form

$$i \frac{\partial U}{\partial \xi} + \frac{1}{2} \frac{\partial^2 U}{\partial \tau^2} + \frac{N^2}{f(\xi)} |U|^2 U = 0, \quad (145)$$

where we assumed  $\beta_2 < 0$  and introduced the soliton order as  $N = (\gamma P_0 L_D)^{1/2}$ . The periodically varying function  $f(z)$  given in Eq. (139) can be written as

$$f(\xi) = \cos^2(2\pi q \xi) + C_f^2 \sin^2(2\pi q \xi), \quad q = L_D/L_p, \quad (146)$$

where  $L_p = 2\pi/b$  is the self-imaging period of a GRIN fiber (about 1 mm for typical GRIN fibers). This NLSE reduces to its standard form for  $C_f = 1$  because  $f(\xi) = 1$  for this value of  $C_f$ . A sech-shaped pulse launched with a peak power such that  $N = 1$  forms a fundamental soliton in this situation and propagates without any change in its shape and spectrum. Clearly, this will not be the case when  $C_f$  deviates from one.

As an example, Fig. 21 shows the evolution of such a pulse with  $N = 1$  over 10 dispersion lengths. These results were obtained by solving Eq. (140) numerically using  $C_f = 0.2$ ,

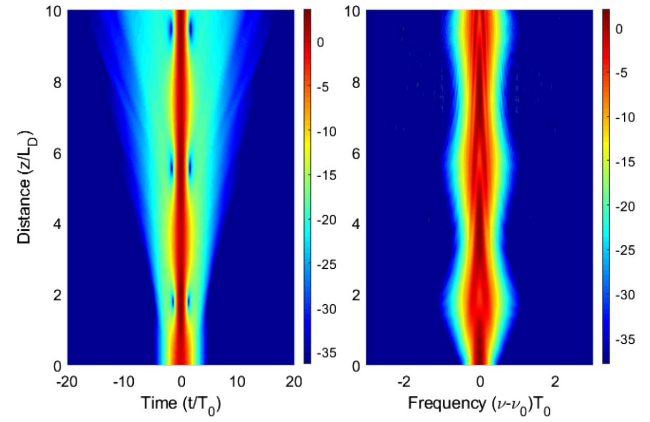


**Fig. 21.** Temporal and spectral evolutions of an optical pulse, launched into a GRIN fiber with a peak power such that  $N = 1$  using the parameter values  $C_f = 0.5$  and  $q = 100$ .

$q = 100$ , and the initial field  $U(0, \tau) = U_0 \text{sech}(\tau)$ , where  $U_0$  was chosen to ensure  $N = 1$ . As expected, both the shape and spectrum change as the pulse propagates inside the GRIN fiber. A nearly periodic evolution seen in Fig. 21 provides a clue that the pulse is forming a higher-order soliton. This feature suggests that the peak power of the input pulse is larger than what is needed for a fundamental soliton, and it should be lowered by reducing  $N$  to below one. The reason for the behavior seen in Fig. 21 can be understood by recalling the periodic spatial focusing of the optical beam owing to its self-imaging. As the beam is compressed during each self-imaging cycle, its peak power  $P_0$  increases considerably, and the nonlinear effects are enhanced.

The solitons evolve on a length scale provided by the fiber's dispersion length  $L_D$ , whereas self-imaging occurs on a length scale  $L_p$  related to the index gradient  $b$  of the GRIN fiber as  $L_p = 2\pi/b$ . The ratio of these two lengths,  $q = L_D/L_p$ , plays an important role as is also evident from Eq. (146). Typically,  $L_p$  is close to 1 mm, whereas the dispersion length  $L_D$  exceeds 1 m even for  $T_0 > 0.1$  ps if we use  $\beta_2 = -20$  ps<sup>2</sup>/km, a typical value for silica fibers at wavelengths near 1550 nm. As a result,  $q$  is a large number ( $q > 100$ ) under typical experimental conditions. Physically, it represents the number of times self-imaging of the input beam occurs inside a GRIN fiber over a distance of one dispersion length.

Solitons cannot respond to beam-size changes taking place on a scale of 1 mm or less when  $L_D$  exceeds 1 m. This suggests that we should average Eq. (145) over one self-imaging period. If we write its solution as  $U = \tilde{U} + u$ , where  $\tilde{U}$  represents average over one self-imaging period  $L_p$ , perturbations  $|u(\xi, \tau)|$  induced by spatial variations remain small enough that they can be neglected (as long as  $q \gg 1$ ). In other words, the dynamics of the soliton can be captured by solving the averaged NLSE

$$i \frac{\partial \tilde{U}}{\partial \xi} + \frac{1}{2} \frac{\partial^2 \tilde{U}}{\partial \tau^2} + \tilde{N}^2 |\tilde{U}|^2 \tilde{U} = 0, \quad (147)$$

where  $\tilde{N}$  is the effective soliton order defined as

$$\bar{N}^2 = N^2(f^{-1}(\xi)) = N^2/C_f. \quad (148)$$

As Eq. (147) has the form of the standard NLSE, it follows that it has a solution in the form of a fundamental soliton when  $\bar{N} = 1$ , or  $N = \sqrt{C_f}$ . Figure 22 shows the numerical results obtained when we solved Eq. (145) with this value of  $N$  using  $q = 100$ . As seen there, both the shape and spectrum of the launched pulse do not change much over a distance of  $10L_D$ . This is also apparent from the bottom panels of Fig. 22, where the shape and spectrum of the pulse at  $z = 10L_D$  are compared with their input shapes. The temporal intensity profiles overlap almost perfectly. Perturbations caused by the periodic self-imaging can be seen in the spectra but only at a level of below 20 dB. We call such solitons GRIN solitons because a GRIN medium is required for their formation. Note also that GRIN solitons can form for a wide range of pulse widths, as long as the peak power of pulses is adjusted to satisfy the condition  $N = \sqrt{C_f}$ .

An important question is related to the stability of GRIN solitons. They are not expected to remain stable over long distances simply because Eq. (140) is not integrable by the inverse scattering method. Small perturbations caused by the periodic spatial self-imaging of the solitonic beam build up over long distances and eventually begin to lose energy through the emission of dispersive radiation. This feature is seen clearly in Fig. 23, where the evolution of a GRIN soliton inside a

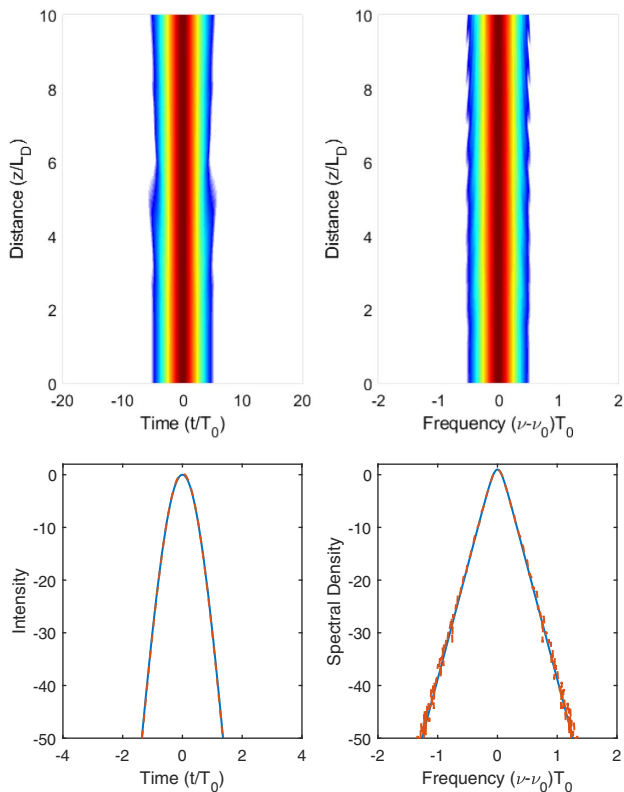


**Fig. 22.** Temporal and spectral evolutions of a fundamental soliton, launched into a GRIN fiber with a peak power such that  $N = \sqrt{C_f}$  using the parameter values  $C_f = 0.5$  and  $q = 100$ . Corresponding intensity profiles are compared at a distance of 0 and  $10L_D$  in the bottom panel.

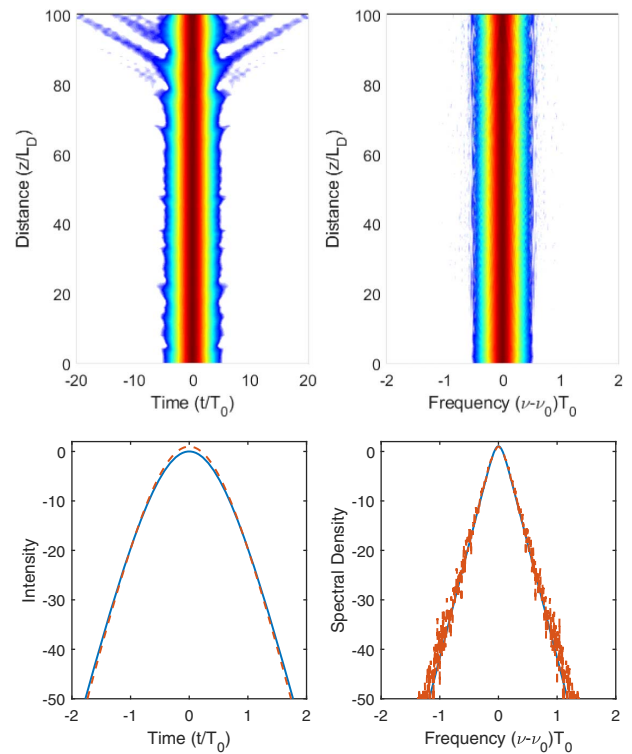


**Fig. 23.** Temporal and spectral evolutions of a fundamental soliton over a distance of  $100L_D$  using the same parameter values used for Fig. 22. Corresponding intensity profiles are compared at a distance of 0 and  $100L_D$  in the bottom panel.

GRIN fiber is shown over 100 dispersion lengths using the same parameter values used for Fig. 22. A comparison of these two figures shows that the GRIN soliton begins to emit dispersive radiation after 80 dispersion lengths. A comparison of temporal and spectral profiles of a fundamental GRIN soliton at the input and output ends shows that noticeable changes indeed occur at a distance of  $100L_D$ .

Higher-order solitons for which both the spatial and temporal widths evolve periodically can also form inside a GRIN fiber [107]. The period of temporal oscillations is set by the dispersion length and is much longer than the period of spatial-width oscillations. This feature is seen clearly in Fig. 24, where the evolution of a second-order GRIN soliton inside a GRIN fiber is shown over 10 dispersion lengths using the same parameter values used for Fig. 22. In contrast with the fundamental soliton, a second-order soliton is perturbed very strongly by the periodic spatial self-imaging of the optical beam. This is apparent from the bottom panel in Fig. 24, where the temporal and spectral profiles of the soliton are compared to those of the input pulse at a distance of  $10L_D$ . Among other things, the pulse's spectrum broadens considerably and develops an oscillatory structure in its wings. The temporal intensity profile also develops fluctuations outside of its central region whose magnitude exceeds 10% of the peak level. Higher-order solitons also break up into multiple fundamental solitons if third-order dispersion is included in Eq. (140).

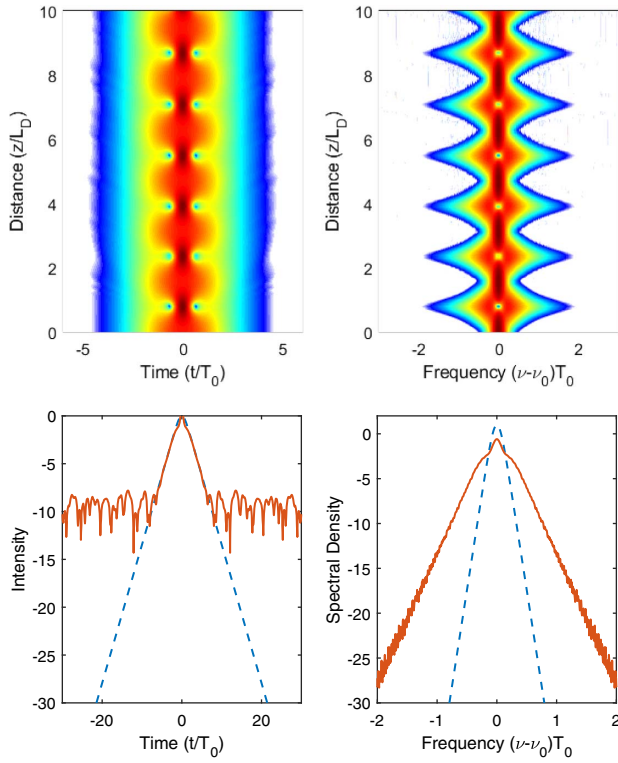


**Fig. 24.** Temporal and spectral evolutions of a second-order soliton over a distance of  $10L_D$  using the same parameter values used for Fig. 22. Corresponding intensity profiles are compared at a distance of 0 and  $10L_D$  in the bottom panel.

### C. Impact of Higher-Order Effects

As we discussed earlier, higher-order effects that become important for short pulses can be included through the generalized NLSE given in Eq. (142). If we use dimensionless variables and include both the third-order dispersion and intrapulse Raman scattering, we can write this equation in the form

$$i \frac{\partial U}{\partial \xi} + \frac{1}{2} \frac{\partial^2 U}{\partial t^2} - i \delta_3 \frac{\partial^3 U}{\partial t^3} + \frac{N^2}{C_f} \left[ (1 - f_R) |U|^2 U + f_R U \int_0^\infty h_R(t') |U(z, t - t')|^2 dt' \right] = 0, \quad (149)$$

where  $\delta_3 = \beta_3 / (6\beta_2 T_0)$ . This equation allows us to study the Raman-induced spectral shift of pulses shorter than 1 ps. This shift is enhanced in GRIN fibers, compared to step-index fibers, because of the periodic self-imaging of a pulsed optical beam inside such fibers [108].

The impact of higher-order effects is even more interesting for higher-order solitons because of a fission process that breaks them into multiple fundamental solitons of different widths. We expect the fission of higher-order solitons to occur even in the case of GRIN fibers because the underlying dynamics remain the same, except for the enhancement of the nonlinear effects when the spatial width of the beam shrinks in each self-imaging period. An important question is whether the self-imaging leads to new features in GRIN fibers during the fission of a higher-order soliton.

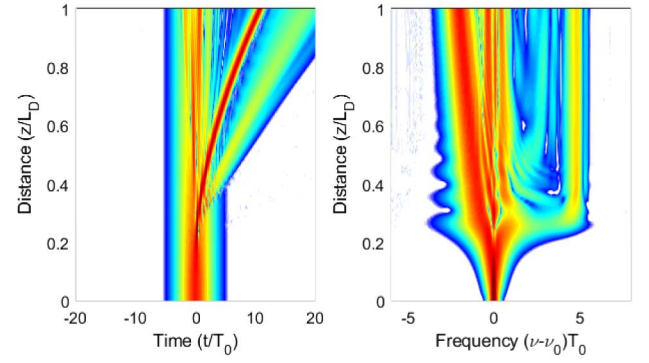


**Fig. 25.** Temporal and spectral evolutions of a fourth-order soliton ( $N = 4$ ) over one dispersion length inside a GRIN fiber with  $C_f = 1$  and  $q = 100$ . Higher-order effects are included using  $f_R = 0.245$  and  $\delta_3 = 0.02$ . Periodic spatial focusing of the pulsed beam does not occur for  $C_f = 1$ .

Figures 25 and 26 compare the evolution of a fourth-order soliton (width 100 fs) over one dispersion length in the time and spectral domains by solving Eq. (149) numerically using  $N = 4$ ,  $\delta_3 = 0.02$ , and  $q = 100$ . The parameter  $C_f$  has a value of one in Fig. 25 and 0.5 in Fig. 26. Recall that only the fundamental mode of a GRIN fiber is excited when  $C_f = 1$ , and no periodic self-imaging or spatial focusing of the beam occurs in this situation. In contrast, multiple modes of a GRIN fiber are excited for  $C_f = 0.5$ , and the pulsed beam undergoes spatial focusing during each self-imaging period.

A comparison of Figs. 25 and 26 shows that the fission of the fourth-order soliton occurs near  $\xi = 0.3$  in both cases. The original soliton breaks into multiple fundamental solitons of different widths. Intrapulse Raman scattering shifts their spectra toward lower frequencies by different amounts and reduces each soliton's speed, resulting in a bent trajectory. The shortest soliton with the largest spectral shift slows down the most, resulting in a bent trajectory that shifts to the right most. The spectrum becomes considerably broader at the output end of the GRIN fiber and exhibits multiple peaks. A new feature

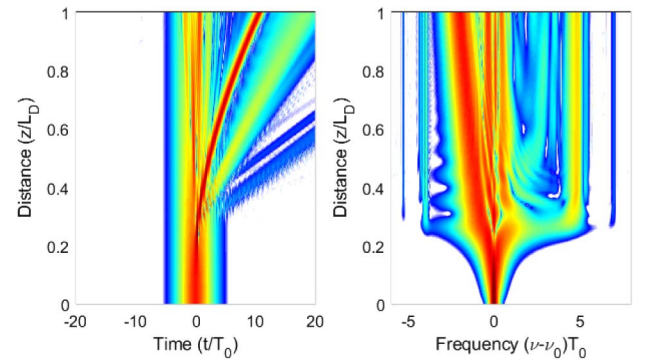


**Fig. 26.** Temporal and spectral evolution of a fourth-order soliton ( $N = 4$ ) over one dispersion length inside a GRIN fiber. Parameter values are identical to those used in Fig. 25 except that the value of  $C_f$  has been reduced to 0.5. Periodic spatial focusing of the pulsed beam occurs when  $C_f < 1$  because multiple modes of the GRIN fiber are excited when  $C_f = 0.5$ .

is the appearance of a blue-shifted peak just after the fission occurs. This peak belongs to a dispersive wave, generated because solitons shed radiation when perturbed by third-order dispersion, a well-known feature in single-mode fibers [56].

The spectral evolution seen in Fig. 26 develops considerably more structures and has multiple sidebands that result from the periodic spatial focusing of a pulsed beam inside a GRIN medium for  $C_f = 0.5$ . The origin of the sidebands is related to the phenomenon of resonant dispersive radiation [41,59] and geometrical parametric instability [60], as discussed in Section 2.C. In the time domain, one can see low-intensity dispersive waves emitted at the frequencies of these sidebands.

## 7. QUADRATURE NUMERICAL MODEL

In this section we describe a Gaussian quadrature approach for the numerical simulation of the generalized nonlinear Schrödinger equation (GNLSE). This approach is similar to the split-step Fourier method that is ubiquitously used for simulation of the standard NLSE, but it uses a mode decomposition based on the natural eigenmodes of the fiber and performs the transformation to this modal basis using an optimized Gaussian quadrature scheme.

A mode decomposition is generally accomplished by projecting the field inside the fiber onto an orthogonal set of linear eigenmodes. These modes maintain a fixed transverse profile and propagate with only a phase shift in the absence of any nonlinearity. The projection is achieved by the evaluation of an integral that can be approximated by a weighted sum of field values that are sampled on a discrete grid of points. In Gaussian quadrature [109] one selects both the weighting coefficients and the location of the sample points (abscissas) to enable an exact mode projection for the first  $N$  modes. The transformation to and from the modal basis, as well as the linear propagation step, can then be carried out as a single multiplication with a predetermined matrix.

A similar numerical quadrature approach to propagation in nonlinear multimode waveguides was previously introduced by Lægsgaard; see Refs. [110,111]. This method has its starting point in the coupled mode model and simulates the GMMNLSE by using on-the-fly real-space Gaussian quadrature integration of the nonlinear polarization. This alleviates the scaling problem common to more conventional approaches that compute the nonlinear polarization by the summation of mode overlap integrals. In Ref. [110] Lægsgaard considered a multimode fiber with a step-index profile, and showed that the numerical complexity of the Gaussian quadrature approach scales linearly or at most quadratically with the number of modes. In particular, it was found that this scheme enables superior computational performance for the nonlinear propagation in a step-index fiber having more than six guided modes, when compared to the overlap integral approach. It was moreover demonstrated that the Gaussian quadrature approach can be extended to accurately account for mode profile dispersion and the associated frequency dependence of the effective area.

### A. Radially Symmetric Model

To illustrate the method, we first consider the non-dispersive case where the beam dynamics is modeled by a radially

symmetric GNLSE with a parabolic refractive index profile:

$$i \frac{\partial E}{\partial z} = \frac{1}{2k_0 r} \frac{\partial}{\partial r} \left( r \frac{\partial E}{\partial r} \right) - \frac{k_0 \Delta n}{R^2} r^2 E + \frac{k_0 n_2}{n_{co}} |E|^2 E. \quad (150)$$

In the linear limit when the power is sufficiently low or when the nonlinear-index coefficient  $n_2 \rightarrow 0$  one finds that the last term can be neglected, and that the GNLSE has an orthogonal set of Laguerre-Gaussian eigenmodes:

$$E_m(r, z) = \exp \left[ -\frac{\beta_0 k_0}{2} r^2 + i\beta_0(2m+1)z \right] L_m(\beta_0 k_0 r^2), \quad (151)$$

where  $\beta_0 = \sqrt{2\Delta n}/R$  and  $L_m$  are Laguerre polynomials with integer mode number  $m$ . These ring-shaped modes can be found, e.g., by variable separation and have a constant normalization factor  $\sqrt{\beta_0 k_0/\pi}$  that has been omitted for clarity. Because of the functional dependence of the Gauss-Laguerre modes, it is convenient to rescale the radial distance and introduce the dimensionless variable  $x = \beta_0 k_0 r^2$  and the nonlinear coefficient  $\Gamma = k_0 n_2/n_{co}$ , so that Eq. (150) becomes

$$i \frac{\partial E}{\partial z} = 2\beta_0 \frac{\partial}{\partial x} \left( x \frac{\partial E}{\partial x} \right) - \frac{\beta_0 x}{2} E + \Gamma |E|^2 E. \quad (152)$$

The different eigenmodes can then be written more compactly as

$$E_m(x, z) = e^{-x/2 + i\beta_0 m z} L_m(x), \quad (153)$$

with the propagation constant  $\beta_m = \beta_0(2m+1)$ .

The Laguerre polynomials and the Gauss-Laguerre functions  $l_m(x) = e^{-x/2} L_m(x)$  form a complete basis for the linear combination of guided modes that can propagate inside the fiber and have the important property of being mutually orthogonal with respect to the weight function  $W(x) = e^{-x}$ . This means that the scalar product

$$\int_0^\infty L_m(x) L_n(x) e^{-x} dx = \int_0^\infty l_m(x) l_n(x) dx = \delta_{mn}, \quad (154)$$

where  $\delta_{mn}$  is the Kronecker delta that vanishes unless the indices of the two modes are equal. The orthogonality is used in the Gaussian quadrature method to approximate the mode projection integral

$$\int_0^\infty f(x) e^{-x} dx \approx \sum_{j=1}^N w_j f(x_j) \quad (155)$$

by a finite  $N$  term sum with weighting coefficients  $w_j$  that are evaluated on a discrete grid of non-equidistantly spaced points  $x_j$ . This approximation can be shown to be exact when the field is a linear superposition of modes in the form of weighted orthogonal polynomials of degree  $2N-1$  or less [109]. In Gauss-Laguerre quadrature the abscissas are chosen as the  $N$  different zeros of the Laguerre polynomial  $L_N(x)$ , i.e., as the roots of the equation

$$L_N(x_j) = 0, \quad j = 1, \dots, N, \quad (156)$$

with  $x_j$  being the  $j$ th zero. The corresponding weighting coefficients are given by [112]



$$w_j = \frac{x_j}{(N+1)^2 [L_{N+1}(x_j)]^2}. \quad (157)$$

To apply the method we expand the spatially varying electric field envelope using the eigenmode functions as

$$E(x, z) = \sum_{k=0}^{N-1} a_k(z) l_k(x), \quad (158)$$

where the complex spectral coefficients  $a_k$  determine the longitudinally evolving mode occupancy. These are obtained from Eq. (155) by identifying the integrand  $f(x) = E(x) l_k(x) e^x$  and approximating the projection operation using the orthogonality relation Eq. (154) with

$$a_k = \int_0^\infty E(x) l_k(x) dx \approx \sum_{j=1}^N w_j e^{x_j} l_k(x_j) E(x_j). \quad (159)$$

This summation can be efficiently performed as a matrix multiplication of the row vector  $E(x_j)$  with the  $N^2$  matrix  $A_{kj} = w_j e^{x_j} l_k(x_j)$ . Given the spectral coefficients  $a_k$  we can perform the inverse transformation and obtain the field values  $E(x_j, z)$  by simply evaluating the summation in Eq. (158) as another multiplication with the matrix  $B_{jk} = l_k(x_j)$ . In particular, it is seen that the product of these two operations  $A_{mj} B_{jn} = B_{mj} A_{jn} = \delta_{mn}$  corresponds to the orthogonality relation given in Eq. (154).

The benefit of projecting the field onto the eigenmode basis is that one directly can simulate radially symmetric fields, without using a Cartesian coordinate system where the Laplacian operator must be evaluated either in 2D or approximated by the second derivative in 1D. The method can moreover be extended to enable spatiotemporal simulations of modal dispersion, as we will see in the next subsection. Because the linear and nonlinear terms in the GNLS Eq. (150) have different natural bases where their solution is particularly easy, we use operator splitting to separately determine the linear and nonlinear evolution of the field in the same way as in the ordinary split-step Fourier method. The equation governing the linear propagation step for  $E(x, z)$ , viz.,

$$i \frac{\partial E}{\partial z} = 2\beta_0 \frac{\partial}{\partial x} \left( x \frac{\partial E}{\partial x} \right) - \frac{\beta_0 x}{2} E, \quad (160)$$

has the solution given by a linear combination of Eq. (153) in the eigenmode basis. Assuming a fixed propagation distance  $\Delta z$  we can therefore evolve the field in the spectral domain by multiplying each component with a simple phase factor that may be written in the form of a diagonal matrix  $D_{kj} = e^{i\beta_0(2k+1)\Delta z} \delta_{kj}$ . Each step of transforming to the eigenmode basis, applying the propagation operator, and performing the inverse transformation is a linear operation that can be reduced to a single matrix multiplication:

$$E(x, z + \Delta z) = \hat{L}(\Delta z) E(x, z), \quad (161)$$

where we have introduced the constant matrix operator  $(\hat{L})_{kj} = B_{kl} D_{li} A_{ij}$  that is calculated beforehand. Note that this also applies to methods using the equidistant Fourier basis when the discrete Fourier transform is represented by the  $N^2$  matrix operator  $W_{kj} = e^{-i2\pi kj/N}$ , but where the steps

are usually performed in sequence to take advantage of the faster  $\mathcal{O}(N \log N)$  scaling of the FFT algorithm.

Conversely, the nonlinear propagation step is governed by the equation

$$i \frac{\partial E}{\partial z} = \Gamma |E|^2 E, \quad (162)$$

which describes self-phase modulation and which has the real space solution

$$E(x, z + \Delta z) = E(x, z) e^{-i\Gamma |E(x, z)|^2 \Delta z} = \hat{N}(\Delta z) E(x, z), \quad (163)$$

which can be represented by the nonlinear matrix operator  $(\hat{N})_{kj} = e^{-i\Gamma |E(x_j, z)|^2 \Delta z} \delta_{kj}$ . Here, we assume a simple dielectric fiber material with an instantaneous Kerr nonlinearity, but the method can easily be extended to handle Raman, self-steepening, and other higher-order effects.

With the separate solutions for both the linear propagation step Eq. (161) and the nonlinear step Eq. (163) determined, we sample the field at the grid points  $x_j$  and apply them alternately. Specifically, we use the fact that the evolution equation

$$i \frac{\partial E}{\partial z} = (\hat{\mathcal{L}} + \hat{\mathcal{N}}) E, \quad (164)$$

where  $\hat{\mathcal{L}}$  and  $\hat{\mathcal{N}}$  are linear differential and nonlinear operators, respectively, has the formal solution  $E(x, z + \Delta z) = e^{-i(\hat{\mathcal{L}} + \hat{\mathcal{N}})(\Delta z)} E(x, z)$ , which can be approximated by the factorized solution  $E(x, z + \Delta z) = \hat{L}(\Delta z/2) \hat{N}(\Delta z) \hat{L}(\Delta z/2) E(x, z)$  with second-order accuracy for small  $\Delta z$  [56].

To apply the method it is necessary to have function values for the Laguerre polynomials  $L_k(x_j)$  at the grid points  $x_j$ . These values can be generated recursively from  $L_0(x) = 1$  and  $L_1(x) = 1 - x$  using the recurrence relation

$$(m+1)L_{m+1}(x) = (2m+1-x)L_m(x) - mL_{m-1}(x). \quad (165)$$

After selecting the number of modes  $N$ , we proceed with these preprocessing steps:

- determine the abscissas  $x_j$  by solving Eq. (156) numerically;
- generate a matrix with the Laguerre polynomials  $L_k(x_j) = l_k(x_j) e^{x_j/2}$  from the recurrence relation Eq. (165);
- calculate the quadrature weight coefficients  $w_j$  from Eq. (157);
- generate the forward and inverse transformation matrices  $A_{kj} = w_j e^{x_j/2} L_k(x_j)$  and  $B_{jk} = e^{-x_j/2} L_k(x_j)$ .

The results of these steps are saved, so that they can be reused in multiple simulations. They need only be repeated if the number of modes is changed in order to, e.g., adjust the trade-off between numerical precision and computation time.

A disadvantage of the above Gauss-Laguerre quadrature is that the endpoints of the radial interval are not included among the sampling points. The lower endpoint at the origin can be particularly important since the optical field will often have its maximum intensity in the center of the fiber and the field at this point will therefore experience a large nonlinear phase shift. To include the origin we can employ an alternative Radau-Laguerre quadrature scheme for the radially symmetric  $l=0$  mode. Modes of higher angular order are not considered

since they are identically zero on axis and have a singularity in the corresponding quadrature scheme.

The modified Radau-Laguerre quadrature relation is given by [113]

$$\int_0^\infty f(x)dx \approx \frac{1}{N}f(0) + \sum_{j=1}^{N-1} w_j f(x_j), \quad (166)$$

where  $x_j$  are now the zeros of the generalized Laguerre polynomial  $L_{N-1}^{(1)}(x) = -L'_N(x)$  and

$$w_j = \frac{1}{N[L_{N-1}^{(1)}(x_j)]^2}. \quad (167)$$

Expanding the field as before, we have the spectral coefficients

$$a_k = \int_0^\infty E(x)l_k(x)dx \approx \frac{1}{N}E(0) + \sum_{j=1}^{N-1} w_j e^{x_j} l_k(x_j)E(x_j), \quad (168)$$

which again can be written as a matrix multiplication. In fact by extending the set of abscissas with  $x_0 = 0$  one can use the same numerical propagation code with either quadrature scheme by simply changing the definition of the matrix operators.

When performing any type of numerical simulations, it is important to consider issues of accuracy, numerical errors, and convergence. The transformed GNLS Eq. (152) conserves two integral quantities corresponding to the power

$$P = \int |E|^2 dx \quad (169)$$

and the Hamiltonian

$$\mathcal{H} = \int \left( 4\beta_0 x \left| \frac{\partial E}{\partial x} \right|^2 + \beta_0 x |E|^2 - \Gamma |E|^4 \right) dx. \quad (170)$$

These invariants are useful to check on the accuracy of the numerical scheme by comparison of their values for the initial and final fields. The derivatives may be evaluated from knowledge of the expansion coefficients by using  $(\partial/\partial x)E(x, z) = \sum_{k=0}^{N-1} a_k(z) l'_k(x)$  and the property that  $l'_m(x) = e^{-x/2} [-L_m(x)/2 + L'_m(x)]$ , where  $L'_m(x) = m[L_m(x) - L_{m-1}(x)]/x$ .

### B. (3D+1) Quadrature Model

The field in a multimode fiber can generally have both angular and temporal dependence. Here, we consider the spatiotemporal dynamics in a parabolic GIMF with an instantaneous Kerr nonlinearity that is governed by the (3D+1) GNLS

$$i \frac{\partial E}{\partial z} = \frac{1}{2k_0} \nabla_\perp^2 E - \frac{k_0 \Delta n}{R^2} r^2 E + \Gamma |E|^2 E - \mathcal{D}^{-1} \left\{ \Delta \beta_0^{(p)} + i \Delta n \beta_1^{(p)} \frac{\partial}{\partial t} + \frac{\beta_2^{(p)}}{2} \frac{\partial^2}{\partial t^2} \right\} E, \quad (171)$$

where  $\mathcal{D}^{-1}$  is an operator for transformation from the linear eigenmode basis, which denotes that the argument should be applied individually to each mode  $p$ , and the longitudinally evolving field  $E = E(\tilde{r}_\perp, t, z)$  is a function of the two transverse coordinates  $\tilde{r}_\perp = x'\hat{x} + y'\hat{y}$  with radius  $r = \sqrt{x'^2 + y'^2}$  and time  $t$ . The nonlinear term can be neglected in the linear limit when the input power is sufficiently low, while the modal

dispersion term can be disregarded by considering a CW field in the form of a single frequency beam. The remaining terms in the model are then the diffractive transverse Laplacian operator and the parabolic refractive index potential. In this limit, the equation has an orthogonal set of separable Gauss-Hermite eigenmode solutions that in Cartesian coordinates are given by

$$E_{l,m}(x, y, z) = H_l(x)H_m(y) \cdot \exp[(x^2 + y^2)/2 + i\beta_0(l + m + 1)z], \quad (172)$$

where  $H_l(x)$  are Hermite polynomials of integer order  $l$  and we have introduced the dimensionless scaled variables  $x = \sqrt{\beta_0 k_0} x'$  and  $y = \sqrt{\beta_0 k_0} y'$ . We note that the function values of the Hermite polynomials can be generated from  $H_0 = 1$  and  $H_1 = 2x$  through the recurrence relation

$$H_{j+1}(x) = 2xH_j(x) - 2jH_{j-1}(x). \quad (173)$$

Alternatively, one can use polar coordinates and the generalized Gauss-Laguerre eigenmode solutions

$$E_m^{(l)}(r, \varphi, z) = x^{l/2} \exp \left[ -\frac{x}{2} + i l \varphi + i \beta_0 (2m + l + 1) z \right] L_m^{(l)}(x), \quad (174)$$

with  $x = \beta_0 k_0 r^2$  as in the previous subsection. However, these are less suitable as a basis for implementing a Gaussian quadrature scheme, since the abscissa points  $x_j^{(l)}$  are not the same for modes of different angular orders. Each order requires the use of a separate sampling grid. This makes the numerical implementation inefficient: it is preferable to expand the field by using the Gauss-Hermite basis instead. The spectral expansion coefficients for the Gauss-Hermite modes can be converted for problems where it is desirable to work in the Gauss-Laguerre basis; see Ref. [114].

Analogous to the radially symmetric model, the Gauss-Hermite functions are mutually orthogonal for each component and form a complete basis. They satisfy the orthogonality relation

$$\frac{1}{2^n n! \sqrt{\pi}} \int_{-\infty}^{\infty} H_m(x) H_n(x) e^{-x^2} dx = \int_{-\infty}^{\infty} \phi_m(x) \phi_n(x) dx = \delta_{nm}, \quad (175)$$

with the basis functions

$$\phi_l(x) = \frac{1}{\sqrt{2^l l! \sqrt{\pi}}} H_l(x) e^{-x^2/2}. \quad (176)$$

The quadrature relation for the Gauss-Hermite functions is given by [112]

$$\int_{-\infty}^{\infty} e^{-x^2} f(x) dx \approx \sum_{j=1}^N w_j f(x_j), \quad (177)$$

where the abscissas  $x_j$  are the  $N$  different zeros of the Hermite polynomial  $H_N(x)$ , i.e.,  $H_N(x_j) = 0, j = 1, \dots, N$ , and the weight coefficients

$$w_j = \frac{2^{N+1} N! \sqrt{\pi}}{[H_{N+1}(x_j)]^2}. \quad (178)$$

Importantly, the Hermite basis functions are separable, and the abscissas for the  $x$ - and  $y$ -directions are therefore independent of each other. This permits the transverse field to be sampled on a single two-dimensional grid in the form of a rectangle. The abscissas are located symmetrically for positive and negative values, and the origin can be included by simply choosing an odd number of points.

Using the basis functions Eq. (176), the field envelope is expanded as a double sum:

$$E(x, y, z) = \sum_{l=0}^{N-1} \sum_{m=0}^{M-1} a_{lm}(z) \phi_l(x) \phi_m(y), \quad (179)$$

with a matrix of longitudinally evolving spectral coefficients  $a_{lm}(z)$ . These are obtained from the quadrature relation Eq. (177) with  $f(x, y) = E(x, y) \phi_l(x) \phi_m(y) e^{x^2+y^2}$  as

$$\begin{aligned} a_{lm} &= \int_{-\infty}^{\infty} \int_{-\infty}^{\infty} E(x, y) \phi_l(x) \phi_m(y) dx dy \\ &\approx \sum_{j=1}^N \sum_{k=1}^M w_j e^{x_j^2} \phi_l(x_j) E(x_j, y_k) w_k e^{y_k^2} \phi_m(y_k) \\ &= A_{lj} E(x_j, y_k) A_{km}, \end{aligned} \quad (180)$$

which can be implemented by matrix multiplication with  $A_{lj} = w_j e^{x_j^2} \phi_l(x_j)$  and  $A_{km} = w_m e^{y_k^2} \phi_m(y_k)$  from the left and right, respectively. Meanwhile, the inverse transformation is given by

$$E(x_j, y_k, z) = \sum_{l=0}^{N-1} \sum_{m=0}^{M-1} \phi_l(x_j) a_{lm}(z) \phi_m(y_k) = B_{jl} a_{lm}(z) B_{mk}, \quad (181)$$

where  $B_{jl} = \phi_l(x_j)$  and  $B_{mk} = \phi_m(y_k)$ . It is convenient to consider a quadratic grid with the same number of sampling points  $N = M$  for each transverse dimension. It is then possible to use the same abscissas  $x_j$  and  $y_k$  and the two  $A$  and  $B$  matrices become the transpose of each other, i.e.,  $A_{km} = (A_{lj})^T$  and  $B_{mk} = (B_{jl})^T$ .

The (3D+1) GNLSSE includes modal dispersion that is taken into account by storing the field in a three-dimensional array where two dimensions are used for the transverse spatial coordinates and one dimension is used for the temporal field variation. A major advantage of using Gaussian quadratures instead of spatial Fourier transforms is that separate dispersive phase shifts can be applied to each individual mode  $p$ . This is done through another frequency-dependent matrix multiplication in the linear step after transforming the field to the eigenmode basis. The modal field is sampled on an equidistant grid in time and is subsequently transformed to and from the frequency domain by applying FFTs along the temporal dimension of the array.

The time-independent version of the evolution Eq. (171) has three invariant integral quantities:

$$P = \iint |E|^2 dx' dy', \quad (182)$$

$$M = \frac{i}{2} \iint \left[ x' \left( \frac{\partial E}{\partial x'} E^* - E \frac{\partial E^*}{\partial x'} \right) + y' \left( \frac{\partial E}{\partial y'} E^* - E \frac{\partial E^*}{\partial y'} \right) \right] dx' dy', \quad (183)$$

$$H = \iint \left[ \frac{1}{k_0} \left( \left| \frac{\partial E}{\partial x'} \right|^2 + \left| \frac{\partial E}{\partial y'} \right|^2 \right) + \beta_0^2 k_0 r'^2 |E|^2 - \Gamma |E|^4 \right] dx' dy', \quad (184)$$

with  $r'^2 = x'^2 + y'^2$ , that corresponds to the conservation of power, angular momentum, and Hamiltonian, respectively. These can be evaluated from the spectral coefficients using the relation  $\phi_l'(x) = -x \phi_l(x) + \sqrt{2} l \phi_{l-1}(x)$ , which follows from  $H_l'(x) = 2 l H_{l-1}(x)$ , and are useful for verifying the numerical accuracy.

### C. Simulation Results

To illustrate the use of quadrature models for the simulation of spatiotemporal solitons, we numerically solve the GNLSSE for a GIMF with a parabolic refractive index profile using a radially symmetric Radau-Laguerre split-step code with constant temporal group-velocity dispersion. As initial conditions we consider the stationary light bullet ansatz

$$E(x, y, t) = A \operatorname{sech}(t/w_t) \exp\left(-\frac{x^2 + y^2}{2w_s^2}\right), \quad (185)$$

where  $A$  is the peak amplitude on the radial axis at the center of the bullet,  $w_t$  is the temporal pulse duration, and  $w_s$  is the beam width. These parameters determine the pulse energy  $\mathcal{E} = 2\pi w_t w_s^2 A^2$  (see Section 5.B.1) that can be used as a control parameter for specifying the soliton solution, as previously shown in Section 5.B.

Working in normalized variables, we assume a pulse energy  $\mathcal{E} = 6$  and set the initial soliton parameters using the semi-analytical expressions from the variational approach. The simulations are performed with 50 radial modes and 1024 points in time. The spatiotemporal intensity profile of the soliton obtained after a normalized distance  $z = 100$  is shown in Fig. 27. The longitudinal evolution of the peak amplitude, spatial beam width, and temporal pulse duration is meanwhile shown in Fig. 28. Here, the beam width and pulse duration are extracted as root-mean-square values from the two moments

$$w_s^2 = \frac{1}{\mathcal{E}} \iint (x^2 + y^2) |E|^2 dx dy dt, \quad (186)$$

$$w_t^2 = \frac{12}{\pi^2 \mathcal{E}} \iint t^2 |E|^2 dx dy dt, \quad (187)$$

respectively. The results show oscillations due to a mismatch of the initial ansatz with the actual light bullet solution. These consist both of radial self-imaging oscillations with spatial period  $z_{S1} = \pi$  and temporal breather oscillations, similar to those that occur in the emission of radiation by conservative solitons with a non-integer soliton number in the standard (1D+1) NLSE.

The time required to simulate the light bullet evolution using the quadrature model was about 30 s on a laptop computer.

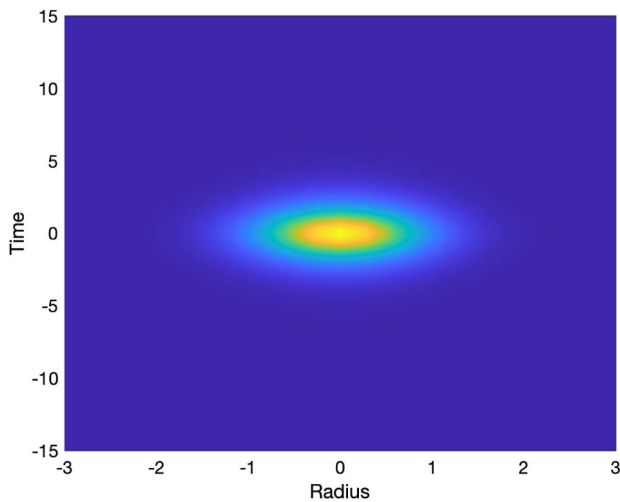


**Fig. 27.** Space-time plot, showing intensity of a light bullet with normalized energy  $\mathcal{E} = 6$ .

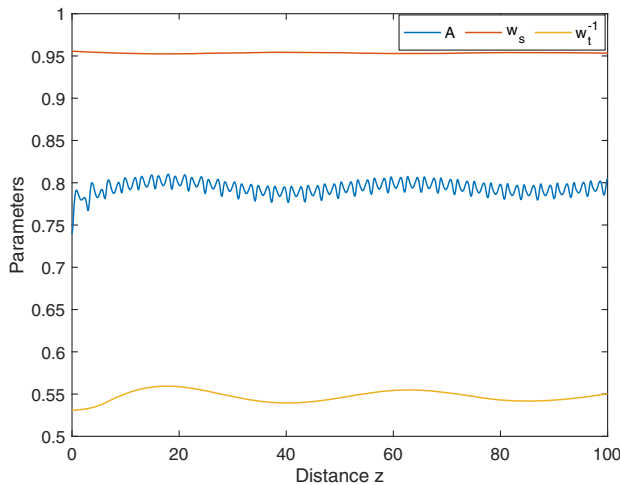


**Fig. 28.** Simulated evolution of peak amplitude, spatial beam width, and temporal pulse duration, respectively, for a light bullet with energy  $\mathcal{E} = 6$ .

## 8. MULTIMODE PROPAGATION IN THE PRESENCE OF RANDOM MODE MIXING

In this section, we focus on the propagation regime that is encountered in the realm of space-division multiplexed (SDM) optical communications in fibers supporting multiple modes [115]. Space-division multiplexed transmission has been in the spotlight of the optical communication research for more than a decade, as it is considered the only viable solution to scale the throughput of fiber-optic communication systems in a sustainable way [116]. An important difference between SDM and transmission in parallel singlemode systems is that SDM entails some form of integration of the transceivers, the optical amplifiers, the network elements, and, ultimately, the lightpaths, as is the case when few-mode fibers (FMFs) and multi-core fibers (MCFs) are utilized. Compared to the propagation regimes discussed in the previous sections of this

paper, SDM transmission differs primarily in the targeted reach, which extends from tens to thousands of kilometers, and in the properties of the transmitted signals, whose average power is of the order of mW, and whose bandwidth is of a few tens of GHz, in typical wavelength-division multiplexed transmission systems.

On the one hand, the significantly longer reach magnifies the impact of linear propagation effects, primarily stemming from manufacturing imperfections and environmental perturbations, which are unavoidable in long fibers. These perturbations are random in nature and therefore they are responsible for inducing random linear coupling between the propagating modes. On the other hand, the relatively small transmission power reduces the impact of nonlinear propagation effects, which are typically modeled within a perturbation approach. Most importantly, nonlinear propagation effects are characterized by a much greater length scale than linear propagation effects, with the result that the nonlinear dynamics is influenced by the random mode coupling. Specifically, the effect of linear mode mixing is to average out the coherent terms in the coupled NLSEs. These terms are responsible for nonlinear power transfer between modes, while the remaining incoherent terms produce cross-mode phase modulation, which is therefore the dominant nonlinear propagation effect in SDM fibers.

The modeling of linear coupling requires supplementing Eq. (26) with additional terms that can be conveniently described by using a generalized Jones formalism [117]. In the frequency domain, neglecting mode-dependent loss [118], linear propagation is described by the following equation [note that, in contrast to Eq. (26), here no moving reference frame is assumed]:

$$\frac{\partial \tilde{\mathbf{A}}}{\partial z} = i\mathbf{B}\tilde{\mathbf{A}}. \quad (188)$$

Here  $\tilde{\mathbf{A}}(z, \omega)$  is the electric field's generalized Jones vector, whose  $2N$  components  $\tilde{A}_p(z, \omega)$  are the Fourier transforms of the complex envelopes  $A_p(z, t)$  describing the excitation of the individual modes and polarizations. (In this section we account for the two-fold polarization degeneracy of each spatial mode, consistent with the need of addressing all space and polarization modes in multiple-input-multiple-output SDM transmission.) The vector  $\tilde{\mathbf{A}}(z, \omega)$  collecting the complex envelopes  $A_p(z, t)$  is sometimes referred to as the field hyper-polarization vector. The term  $\mathbf{B}(z, \omega)$  is a  $2N \times 2N$  Hermitian matrix describing frequency-dependent mode coupling. In all cases of practical relevance, it is sufficient to expand  $\mathbf{B}$  to the second-order around the central frequency  $\omega_0$ :

$$\mathbf{B}(z, \omega) \simeq \mathbf{B}_0 + \mathbf{B}_1(\omega - \omega_0) + \mathbf{B}_2 \frac{(\omega - \omega_0)^2}{2}, \quad (189)$$

where  $\mathbf{B}_q(z) = \partial^q \mathbf{B}(z, \omega) / \partial \omega^q |_{\omega=\omega_0}$ . In the absence of perturbations to the ideal fiber structure, the matrices  $\mathbf{B}_0$ ,  $\mathbf{B}_1$ , and  $\mathbf{B}_2$  reduce to a diagonal form and their elements are the propagation constants, group delays per unit fiber length, and chromatic-dispersion coefficients of the individual modes, respectively, with the modal dependence of the diagonal terms of  $\mathbf{B}_1$  being responsible for the phenomenon of modal dispersion. In the presence of perturbations, off-diagonal terms appear, along with additional traceless diagonal terms [117].

The effect of the perturbations is most relevant on  $\mathbf{B}_0$ , and less on  $\mathbf{B}_1$ , while it is typically negligible on  $\mathbf{B}_2$ . This is consistent with the observation that perturbing the modes' optical phases requires less effort than perturbing their group velocities and even less group-velocity dispersion. Therefore, in the following we neglect the effect of perturbations on  $\mathbf{B}_2$ .

An important property of multimode propagation in SDM fibers is the existence of groups of modes with very similar propagation constants. Modes belonging to the same group are referred to as degenerate or quasi-degenerate, and they undergo strong random coupling during propagation. On the other hand, modes belonging to different groups couple weakly even over long propagation distances, and they are referred to as non-degenerate. This situation can be conveniently described in the field hyper-polarization vector by grouping together quasi-degenerate modes, so that the vector  $\vec{A}$  results from stacking on top of other hyper-polarization vectors with lower dimensions. Consistently, the matrix  $\mathbf{B}_0$  can be divided into blocks, each describing either intra-group coupling or inter-group coupling, while the matrices  $\mathbf{B}_1$  and  $\mathbf{B}_2$  are block-diagonal, as is clarified in the following.

Moving to the modeling of the Kerr nonlinearity, here we restrict the discussion to considering the instantaneous contribution only, in which case the coupled propagation equation can be recast in the following vector form:

$$\frac{\partial \vec{A}}{\partial z} = i\mathbf{B}_0 \vec{A} - \mathbf{B}_1 \frac{\partial \vec{A}}{\partial t} - \frac{i}{2} \mathbf{B}_2 \frac{\partial^2 \vec{A}}{\partial t^2} + \vec{\mathcal{N}}, \quad (190)$$

with

$$\vec{\mathcal{N}} = i\gamma \sum_{p=1}^{2N} \left( \sum_{l,m,n} C_{plmn} A_l^* A_m A_n \right) \hat{e}_p, \quad (191)$$

where, by  $\hat{e}_p$ , we denote a vector whose  $p$ -th element is equal to one and all the others to zero, and  $\gamma = \gamma^{(1)}$  is the nonlinearity coefficient of the fundamental mode defined in Eq. (5) (in this section we drop the superscript for ease of notation). The definition of the nonlinearity coefficients  $C_{plmn}$  accounts for polarization, and their expressions can be found in Eq. (17) of Ref. [66].

### A. Single Group of Strongly Coupled Modes

A particularly relevant propagation regime in SDM systems is the one where all the transmitted modes undergo strong and random mixing along the fiber. This is the case in coupled-core MCFs [119], where the fiber cores are spaced to the extent that the supermodes have sufficiently similar propagation constants to behave almost as degenerate modes. In this regime, the matrix  $\mathbf{B}_0$  can be expressed as  $\mathbf{B}_0 = \tilde{\beta} \mathbf{I} + \delta \mathbf{B}_0$ , where  $\tilde{\beta}$  is the mode-averaged propagation constant, while  $\delta \mathbf{B}_0$  accounts for the modes' propagation-constant mismatch relative to  $\tilde{\beta}$ , as well as for the effect of the perturbations. The matrix  $\mathbf{B}_1$  can be expressed as  $\mathbf{B}_1 = \tilde{\beta}_1 \mathbf{I} + \delta \mathbf{B}_1$ , where  $\tilde{\beta}_1$  is the mode-averaged mode delay per unit propagation length, while  $\delta \mathbf{B}_1$  accounts for the differential mode delays relative to  $\tilde{\beta}_1$ , as well as for the effect of the perturbations. Finally, the matrix  $\mathbf{B}_2$  is typically approximated as  $\mathbf{B}_2 \simeq \tilde{\beta}_2 \mathbf{I}$ , where  $\tilde{\beta}_2$  is the mode-averaged chromatic-dispersion coefficient. Note that the terms involving  $\tilde{\beta}_0$

and  $\tilde{\beta}_1$  are responsible for a mode-independent phase and group delay, respectively, and therefore they can be dropped from the propagation equation with no consequences on the analysis.

As for the nonlinear term  $\vec{\mathcal{N}}$ , a dramatic simplification is obtained by noting that the perturbations produce full randomization of the propagating field hyper-polarization state on a length-scale over which nonlinear effects are not appreciable for typical transmission signal power levels. As a result of this separation of length scales,  $\vec{\mathcal{N}}$  can be replaced with its average, performed with respect to the isotropic distribution of the field hyper-polarization in the generalized Jones space. The only plausible form of  $\vec{\mathcal{N}}$  resulting from this procedure is  $\vec{\mathcal{N}} = i\gamma \bar{\kappa} |\vec{A}|^2 \vec{A}$ , where  $|\vec{A}|^2 = \sum_{k=1}^{2N} |A_k|^2$  is the total optical power carried by the multi-modal field, given by the sum of the optical power in each mode. This follows from noting that since the generalized Jones vector  $\vec{A}$  is isotropically oriented in its space, there can be no privileged direction other than its own, and hence the nonlinear term  $\vec{\mathcal{N}}$  must be aligned with  $\vec{A}$ . On the other hand, owing to the isotropic argument, the magnitude of  $\vec{\mathcal{N}}$  can only depend on the magnitude of  $\vec{A}$ . Therefore,  $|\vec{A}|^2 \vec{A}$  is the only form of  $\vec{\mathcal{N}}$  that at the same time is compatible with the above requirements and with Eq. (191). This argument indicates that the nonlinear interaction between strongly coupled spatial modes takes the form of cross-phase modulation, similar to the nonlinear interaction between polarization modes in singlemode fibers [56].

The derivation of the expression for the nonlinearity coefficient  $\bar{\kappa}$  is described in Refs. [66,120]. It is based on the observation that  $\bar{\kappa}$  should ensure that the average infinitesimal phase shift over a length  $dz$  obtained with the averaged expression is preserved, that is,

$$\vec{\mathcal{N}} \cdot \vec{A}^* dz = i\bar{\kappa} |\vec{A}|^2 \vec{A} \cdot \vec{A}^* dz, \quad (192)$$

or equivalently, using Eq. (191),

$$\sum_{p,l,m,n} C_{plmn} A_l^* A_m A_n A_p^* = \bar{\kappa} |\vec{A}|^4. \quad (193)$$

The problem at hand is to find  $\bar{\kappa}$  such that Eq. (193) is valid when averaged over an isotropic distribution, for a fixed amplitude of the field vector  $|\vec{A}|$ . The derivation starts by noting that an isotropically distributed unit vector can be described as  $\vec{G}/|\vec{G}|$ , where  $\vec{G} = \sum_{p=1}^{2N} G_p \hat{e}_p$  is a vector whose components are  $2N$  identically distributed, statistically independent zero-mean complex variables with Gaussian distribution and correlations  $\langle G_p^* G_q \rangle = \delta_{p,q}$  and  $\langle G_p G_q \rangle = 0$ . The angular degrees of freedom of  $\vec{G}$  are independent of the intensity  $|\vec{G}|^2$ , so that they can be averaged separately. Being the angular distribution of  $\vec{G}$  equal to that of  $\vec{A}$ , if we average Eq. (193) with  $\vec{A}$  replaced by  $\vec{G}$  and divide both sides by the average of  $|\vec{G}|^4$ , we remove the dependence on the statistics of  $|\vec{G}|^2$  and obtain the same result as if the averages were performed over the isotropic distribution of the unit modulus vector  $\vec{G}/|\vec{G}|$ .

The above discussion suggests that  $\bar{\kappa}$  can be derived by averaging both sides of Eq. (193) with  $\vec{A}$  replaced by  $\vec{G}$ . In doing so,

we utilize at the left-hand side the independence of the components of  $\vec{G}$  and the property of independent Gaussian variables that allow us to average them pairwise, so that we get for the average inside the sum  $\langle G_i^* G_m G_n G_p^* \rangle = \delta_{i,m} \delta_{n,p} + \delta_{i,n} \delta_{m,p}$ . In averaging the right-hand side, we exploit that the distribution of  $|\vec{G}|^2$  is a chi-square with  $4N$  degrees of freedom (the real and imaginary parts of  $2N$  modes), each one with variance  $1/2$ , resulting in  $\langle |\vec{G}|^4 \rangle = 4N(4N + 2)(1/2)^2$ . Equating the results of these two averages yields

$$\bar{\kappa} = \sum_{m,n} \frac{C_{nnmm} + C_{mmnn}}{2N(2N + 1)}. \quad (194)$$

The propagation equation for  $\vec{A}$  hence simplifies to [120]

$$\frac{\partial \vec{A}}{\partial z} = i\delta\mathbf{B}_0 \vec{A} - \delta\mathbf{B}_1 \frac{\partial \vec{A}}{\partial t} - \frac{i}{2}\beta_2 \frac{\partial^2 \vec{A}}{\partial t^2} + i\gamma\bar{\kappa}|\vec{A}|^2 \vec{A}. \quad (195)$$

In the case of singlemode fibers, the nonlinearity coefficient reduces to  $\bar{\kappa} = (8/9)(1 - f_R) + f_R$ , and to the familiar value of  $8/9$  when the instantaneous Raman contribution is ignored [121]. It is customary expressing Eq. (195) in a reference frame that accounts for the random mode coupling, that is, by defining the field  $\vec{A}'$  through  $\vec{A} = \mathbf{U}\vec{A}'$ , with  $d\mathbf{U}/dz = i\delta\mathbf{B}_0 \mathbf{U}$ . This results in the disappearance of the first term on the right-hand side of Eq. (195), which, dropping the primes for ease of notation, becomes

$$\frac{\partial \vec{A}}{\partial z} = -\mathbf{D} \frac{\partial \vec{A}}{\partial t} - \frac{i}{2}\beta_2 \frac{\partial^2 \vec{A}}{\partial t^2} + i\gamma\bar{\kappa}|\vec{A}|^2 \vec{A}, \quad (196)$$

where  $\mathbf{D} = \mathbf{U}^\dagger \delta\mathbf{B}_1 \mathbf{U}$ . This equation is the generalization to the multi-dimensional case of the equation that describes nonlinear propagation in single-mode fibers with polarization-mode dispersion (PMD), also known as the PMD-Manakov equation [121]. The first term on the right-hand side describes the phenomenon of spatial mode dispersion (MD), which is the multimodal equivalent of PMD [122].

In the absence of MD, Eq. (196) reduces to the form of a generalized multi-component Manakov equation [123], which in the singlemode case coincides with the famous Manakov equation [124], which was found to describe nonlinear propagation in singlemode fibers in the presence of random polarization-mode coupling [125]. In this limit, Eq. (196) is known to be integrable by using the inverse-scattering transform method, and to admit vector-soliton solutions. The existence of this class of solutions was used in Ref. [120] to test the accuracy of the multi-component Manakov equation in describing multimode propagation in the regime of strong mode mixing.

Modal dispersion renders Eq. (196) non-integrable by introducing frequency-dependent random-mode coupling. In SDM systems, this effect is one of the key factors that determine the complexity of the multiple-input-multiple-output (MIMO) digital-signal processing (DSP) that is required to equalize the fiber-optic channel [126]. The magnitude of MD is typically quantified in terms of the duration of the fiber intensity impulse response (IIR) [127], which grows proportionally to the square-root of propagation distance as  $T_{\text{IIR}} = \bar{\kappa}_{\text{MD}}\sqrt{z}$ , where the proportionality coefficient  $\bar{\kappa}_{\text{MD}}$  depends on the fiber design and perturbation statistics [128]. As a result, MD

prevents the existence of soliton solutions. Its effect on the propagation of an input waveform corresponding to the fundamental soliton of Eq. (196) in the absence of MD is illustrated in Fig. 29 in the case of a fiber with  $2N = 4$  strongly coupled modes. The three panels show the evolution of  $|\vec{A}|^2$  for the input field  $\vec{A}(0, t) = A_0 \text{sech}(t/t_0)\hat{e}_1$ , with  $A_0 = \sqrt{|\beta_2|/\gamma\bar{\kappa}t_0^2}$  and  $L_D = t_0^2/|\beta_2|$ . The numerical values assumed for the plot are  $t_0 = 10$  ps,  $\gamma\bar{\kappa} \approx 0.63 \text{ W}^{-1} \text{ km}^{-1}$ , and  $\beta_2 = -25 \text{ ps}^2/\text{km}$  [120], while the values of  $\bar{\kappa}_{\text{MD}}$  are displayed

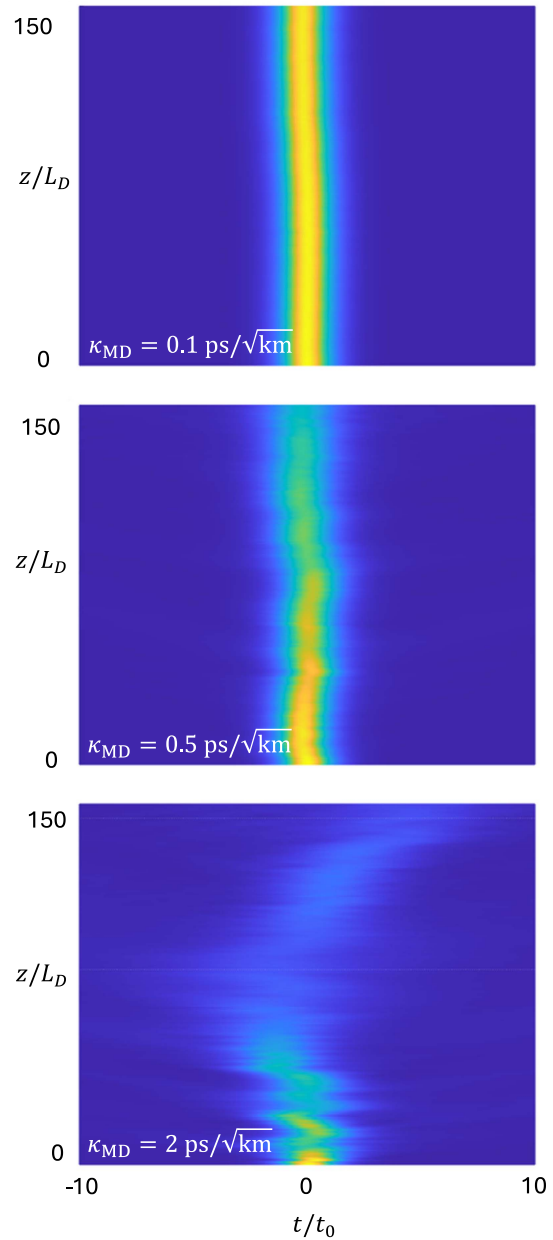


**Fig. 29.** Evolution of an input hyperbolic-secant waveform  $\vec{A}(0, t) = A_0 \text{sech}(t/t_0)\hat{e}_1$ , which in the absence of mode dispersion would result in a fundamental soliton, in a fiber supporting  $2N = 4$  strongly coupled modes for the displayed values of the mode-dispersion coefficient  $\bar{\kappa}_{\text{MD}}$ . Time and propagation distance are normalized to the input-waveform width  $t_0$  and the fiber dispersion length  $L_D = t_0^2/|\beta_2|$ , respectively.

in the individual panels. The plot shows that when MD is sufficiently small, the evolving field preserves its input intensity profile, whereas this is disrupted already after a few dispersion lengths as MD increases.

## B. Multiple Groups of Non-degenerate Modes

A more general propagation regime in fibers for SDM is the one in which multiple groups of non-degenerate modes propagate with little-to-negligible inter-group local coupling. This is the case of both SIMF and GIMF, where the two-fold degenerate fundamental mode LP<sub>01</sub> (with two degenerate polarization modes) and the four-fold degenerate mode group LP<sub>11</sub> (with its two degenerate modes LP<sub>11a</sub> and LP<sub>11b</sub>) form a typical example of non-degenerate mode groups.

Nonlinear propagation in this regime can be conveniently described by organizing the elements of  $\vec{A}$  into vectors of reduced dimensions, each describing a single-mode group. Without loss of generality, in the following we consider the case of two mode groups, which we denote by  $a$  and  $b$  (the generalization to the more general case of an arbitrary number of mode groups is straightforward). The propagation Eq. (190) can therefore be expressed as

$$\frac{\partial \vec{A}_a}{\partial z} = i\mathbf{B}_{a,0}\vec{A}_a - \mathbf{B}_{a,1} \frac{\partial \vec{A}_a}{\partial t} - \frac{i}{2}\tilde{\beta}_{a,2} \frac{\partial^2 \vec{A}_a}{\partial t^2} + i\mathbf{K}_{ab}\vec{A}_b + i\vec{\mathcal{N}}_a, \quad (197)$$

$$\frac{\partial \vec{A}_b}{\partial z} = i\mathbf{B}_{b,0}\vec{A}_b - \mathbf{B}_{b,1} \frac{\partial \vec{A}_b}{\partial t} - \frac{i}{2}\tilde{\beta}_{b,2} \frac{\partial^2 \vec{A}_b}{\partial t^2} + i\mathbf{K}_{ab}^\dagger \vec{A}_a + i\vec{\mathcal{N}}_b. \quad (198)$$

Here  $\vec{A}_a$  and  $\vec{A}_b$  are vectors of dimensions  $2N_a$  and  $2N_b$ , respectively, with  $\vec{A}_a$  collecting the first  $2N_a$  and  $\vec{A}_b$  the last  $2N_b$  elements of  $\vec{A}$ . All the matrices are either  $2N_a \times 2N_a$  or  $2N_b \times 2N_b$  dimensional, except for the matrix  $\mathbf{K}_{ab}$  describing instantaneous inter-group linear coupling, whose dimension is  $2N_a \times 2N_b$ . (Note that only instantaneous inter-group coupling has been taken into account, whereas high-order terms in the expansion of off-diagonal blocks are neglected, as is appropriate in cases of practical relevance.) The nonlinear terms have the following form:

$$\vec{\mathcal{N}}_a = i\gamma \sum_{p=1}^{2N_a} \left( \sum_{l,m,n} C_{plmn} A_l^* A_m A_n \right) \hat{e}_p, \quad (199)$$

$$\vec{\mathcal{N}}_b = i\gamma \sum_{p=2N_a+1}^{2N_a+2N_b} \left( \sum_{l,m,n} C_{plmn} A_l^* A_m A_n \right) \hat{e}_p. \quad (200)$$

Owing to the strong intra-group mode mixing, similar arguments used for the derivation of the multi-component MD-Manakov Eq. (196) can be used to simplify the nonlinear terms in Eqs. (199) and (200). To this end it is critical to assume statistically independent random coupling processes in the two mode groups. Under this assumption, the only plausible forms for  $\vec{\mathcal{N}}_a$  and  $\vec{\mathcal{N}}_b$  are  $\vec{\mathcal{N}}_a = i\gamma(\bar{\kappa}_{aa}|\vec{A}_a|^2 + \bar{\kappa}_{ab}|\vec{A}_b|^2)\vec{A}_a$  and  $\vec{\mathcal{N}}_b = i\gamma(\bar{\kappa}_{bb}|\vec{A}_b|^2 + \bar{\kappa}_{ba}|\vec{A}_a|^2)\vec{A}_b$ . This indicates that, similar to the case of a single group of modes, inter-group nonlinear interaction takes the form of cross-phase modulation,

with each mode group imposing a phase modulation proportional to its overall optical intensity onto each of the modes of the other mode group.

The derivation of the expressions for  $\bar{\kappa}_{aa}$ ,  $\bar{\kappa}_{bb}$ ,  $\bar{\kappa}_{ab}$ , and  $\bar{\kappa}_{ba}$  is described in Ref. [129]. In this case too, the derivation is based on the observation that the average infinitesimal phase shift over a length  $dz$  obtained with the averaged expression is preserved, that is, for  $\vec{\mathcal{N}}_a$

$$\vec{\mathcal{N}}_a \cdot \vec{A}_a^* dz = i\gamma(\bar{\kappa}_{aa}|\vec{A}_a|^4 + \bar{\kappa}_{ab}|\vec{A}_b|^2|\vec{A}_a|^2) dz, \quad (201)$$

or, using Eq. (191),

$$\sum_{p=1}^{2N_a} \sum_{l,m,n} C_{plmn} A_l^* A_m A_n A_p^* = \bar{\kappa}_{aa}|\vec{A}_a|^4 + \bar{\kappa}_{ab}|\vec{A}_b|^2|\vec{A}_a|^2. \quad (202)$$

The only terms whose average is nonzero are those for which either  $m = p$  and  $l = n$ , or  $n = p$  and  $l = m$ . Moreover, all terms for which  $l, m$ , and  $n$  range between one and  $2N_a$  contribute to  $\bar{\kappa}_{aa}|\vec{A}_a|^4$ , with the same result obtained for the case of a single group of modes, that is,

$$\bar{\kappa}_{aa} = \sum_{m,n=1}^{N_a} \frac{C_{mnm} + C_{mnmn}}{2N_a(2N_a + 1)}. \quad (203)$$

When  $m = p$  and  $l = n$ , with  $n > 2N_a$ , the average of  $|A_p|^2|A_n|^2$  splits into the product of the two averages of  $|A_p|^2$  and  $|A_n|^2$ . Similarly, when  $n = p$  and  $l = m$  with  $m > 2N_a$ , the average of  $|A_p|^2|A_m|^2$  reduces to the product of the two averages of  $|A_p|^2$  and  $|A_m|^2$ . These terms contribute to  $\bar{\kappa}_{ab}|\vec{A}_b|^2|\vec{A}_a|^2$ , with the result

$$\bar{\kappa}_{ab} = \sum_{m=1}^{N_a} \sum_{n=2N_a+1}^{2N_a+2N_b} \frac{C_{mnm} + C_{mnmn}}{4N_a N_b}. \quad (204)$$

Along the same lines, one may also find that

$$\bar{\kappa}_{bb} = \sum_{m,n=1}^{N_b} \frac{C_{mnm} + C_{mnmn}}{2N_b(2N_b + 1)}, \quad (205)$$

and  $\bar{\kappa}_{ba} = \bar{\kappa}_{ab}$ . Assuming a moving reference frame that accounts for intra-group random-mode coupling in each mode group, Eqs. (197) and (198) simplify to the following form:

$$\frac{\partial \vec{A}_a}{\partial z} = -\tilde{\beta}_{a,1} \frac{\partial \vec{A}_a}{\partial t} - \mathbf{D}_a \frac{\partial \vec{A}_a}{\partial t} - \frac{i}{2}\tilde{\beta}_{a,2} \frac{\partial^2 \vec{A}_a}{\partial t^2} + i\mathbf{K}_{ab}\vec{A}_b + i\gamma(\bar{\kappa}_{aa}|\vec{A}_a|^2 + \bar{\kappa}_{ab}|\vec{A}_b|^2)\vec{A}_a, \quad (206)$$

$$\frac{\partial \vec{A}_b}{\partial z} = -\tilde{\beta}_{b,1} \frac{\partial \vec{A}_b}{\partial t} - \mathbf{D}_b \frac{\partial \vec{A}_b}{\partial t} - \frac{i}{2}\tilde{\beta}_{b,2} \frac{\partial^2 \vec{A}_b}{\partial t^2} + i\mathbf{K}_{ab}^\dagger \vec{A}_a + i\gamma(\bar{\kappa}_{bb}|\vec{A}_b|^2 + \bar{\kappa}_{ba}|\vec{A}_a|^2)\vec{A}_b, \quad (207)$$

where the matrices  $\mathbf{D}_a$  and  $\mathbf{D}_b$  describe intra-group mode dispersion, and  $\tilde{\beta}_{a,1}$  and  $\tilde{\beta}_{b,1}$  are the intra-group mode-averaged group delays per unit propagation length. Note that when  $N_a = N_b = 1$ , Eqs. (206) and (207) may be used to describe nonlinear propagation in weakly coupled core MCFs [130] or in fibers guiding optical-angular momentum modes. It is also interesting to note that in the absence of intra-group MD and inter-group linear coupling, Eqs. (206) and (207) predict

soliton trapping (see the previous Sections 3 and 4 for its detailed discussion), the phenomenon where two solitary waves, each propagating within distinct groups of modes, dynamically adjust their center frequency to eliminate the group velocity mismatch between the two groups of modes [120,131].

## 9. MMS EXPERIMENTS

### A. Quasi-Single-Mode Regime

In spite of the widespread interest in soliton science, virtually no experimental studies of MMS propagation in MMF have been reported until 11 years ago, when Renninger and Wise carried out the first systematic experimental study of MMSs in GIMF [132]. In their experiments, 300 fs pulses at 1550 nm, with energies of up to a few nJ, were injected into a standard GIMF with 62.5  $\mu\text{m}$  core diameter. Since the input beam came from a single-mode fiber, its diameter (11.5  $\mu\text{m}$ ) was smaller than that of the fundamental mode of the MMF ( $\approx 17.5 \mu\text{m}$ ). Although three radially symmetric nondegenerate modes were excited at the fiber input, more than 90% of the input energy remained coupled into the fundamental mode. Under these conditions, numerical simulations demonstrated that the modes are trapped and propagate collectively in the temporal domain. In other words, the group-velocity walk-off between the fundamental and the HOMs was compensated for by the presence of nonlinear cross-phase modulation, as elaborated in the examples provided in Section 3.B.1. Consequently, this leads to a blue shift of the HOMs, hence a compensation of group-velocity mismatch via group-velocity dispersion. The situation is analogous to the case observed for solitons in birefringent optical fibers in the presence of polarization mode dispersion [73,133].

Whenever one replaces the description based on the multi-component or coupled NLSEs with the collective approach, based on the 3D+1 NLSE or the Gross-Pitaevskii equation, one may exploit the variational approach to find a stable spatiotemporal soliton, or optical bullet (see methodology in Section 5). In the conditions of the experiments in Ref. [132], the MMS can be well approximated by a single-mode soliton solution of the NLSE, with an effective area equal to that of the fundamental mode of the GIMF. The quasi-single-mode nature of the generated MMSs was confirmed by measurements of their output temporal duration versus pulse energy, as well as of the pulse energy dependence of the Raman-induced SSFS (see Fig. 30). A red-shift of the MMS frequency was observed that could be accurately fitted by single-mode soliton perturbation theory, as well as a compression of the pulse width  $T_0$  as its energy  $\mathcal{E}$  grows larger, according to Eq. (21) in Section 2.D. The fundamental Raman soliton wavelength shift, which grows larger with the fourth power of pulse energy (theoretical dependence for single-mode solitons), is given by the red solid curve in Fig. 30(c).

### B. Fully Multimode Regime

The generation of highly multimode MMS, that is, by exciting a relatively large number of HOMs at the fiber input, was experimentally investigated by Wright *et al.* in 2015 [62]. In that study, the input pulse width at 1550 nm was 500 fs, and a 62.5  $\mu\text{m}$  core diameter, 25 m long GRIN fiber was used.

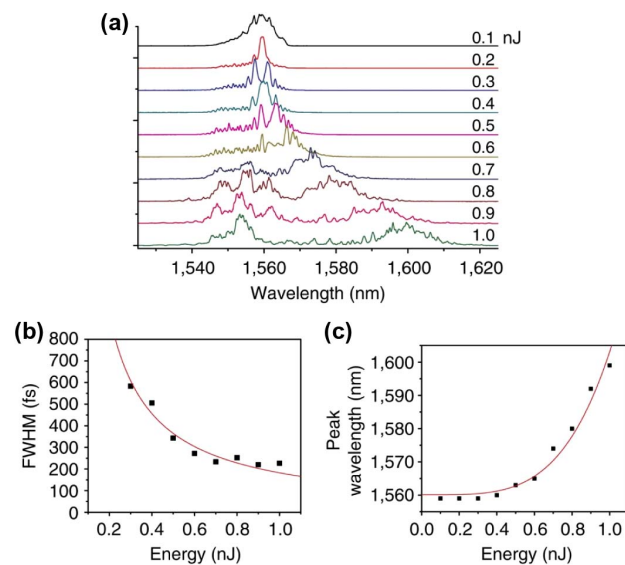


**Fig. 30.** Experimental study of MMS versus input pulse energy. (a) Output spectra. (b) Measured output pulse temporal duration. (c) Measured peak wavelength. Reprinted with permission from Ref. [134]. Copyright 2013, Nature Group.

The relatively larger input beam size leads to the generation of MMSs comprising up to 8–13 modes. Under these conditions, a relatively complex interplay of MMS fission and subsequent SSFS was observed. Specifically, the process of SSFS is accompanied by a transfer of energy from the HOMs towards the fundamental mode of the fiber. This occurs because, as a result of the previously described mechanism of nonlinear modal trapping leading to MMS formation, the fundamental mode is slightly red-shifted with respect to the HOMs. Hence, the fundamental mode is a Stokes wave for HOMs, which act as Raman pumps (see detailed discussion in Section 2.B.5). Moreover, the fundamental mode also exhibits the strongest modal overlap with the dispersive waves that remain around the input pump wavelength, so it preferentially drags energy from them as well [63]. As a result, a Raman MMS beam amplification and spatial cleanup are observed, at the expense of HOMs.

The generation of an MMS rests on the compensation of intermodal dispersion (which is much stronger than intramodal, or chromatic dispersion) by nonlinear phase shifts. As a result, the cross-phase modulation among the different modal components of an MMS should be much stronger than the self-phase modulation for a singlemode soliton (which is only sufficient to counteract chromatic dispersion). This condition was confirmed in the experiments [62]: by measuring the relation between the MMS pulse energy  $\mathcal{E}$  and its temporal width  $T_0$  for a variety of different spatial beam widths  $R_g$ . Wright *et al.* have shown that, for a given temporal soliton duration, its energy is always significantly larger than that of a pure single-mode soliton with the same beam width (see Fig. 31), in qualitative agreement with the early findings by Grudinin *et al.* [135]. From a multimodal perspective, the nonlinear lengths for HOMs in GIMF, as defined in Eq. (6), are longer when compared to that of the fundamental mode, owing to their



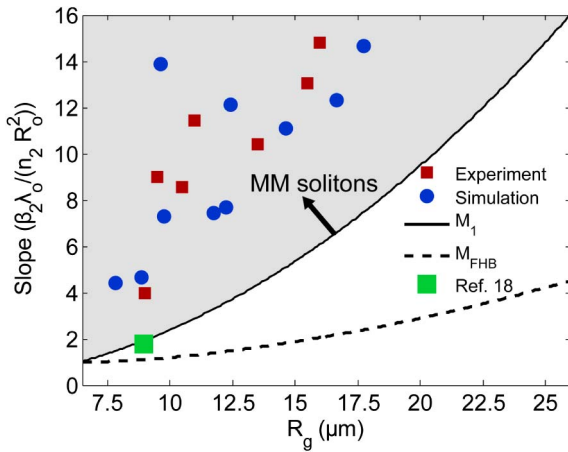


**Fig. 31.** Experimental demonstration that MMSs require more energy than single-mode solitons, for a given temporal duration. In the vertical axis, the figure reports experimental and simulation results for the slope of the linear relation between pulse energy and inverse temporal duration, as a function of the average size of the beam waist  $R_g$  (the waist of the fundamental mode is  $R_0 = 6.5 \mu\text{m}$ ). All data points are higher than the curve for single-mode solitons [solid black curve shows  $M_1 = \mathcal{E}T_0$  as given by Eq. (23)]; the green point indicates the case of quasi-single-mode soliton observed in Ref. [134]. Reprinted with permission from Ref. [62]. Copyright 2015, Optical Society of America.

larger effective areas. Consequently, generating MMS with HOMs requires a relatively higher field peak power. On the other hand, because of their essential single-mode nature, the energy of the first MMS that was studied in Ref. [132] was still very close to that of single-mode fiber solitons. The experimental observation is that highly multimode MMSs are formed at comparatively higher pulse energies than that of single-mode solitons with the same pulse width. This is because stronger nonlinear trapping forces are required to balance modal walk-off [33–35]. The results of Fig. 31 imply that for highly multimode MMSs the pulse duration can be continuously varied, provided the pulse energy scales in inverse proportion, according to Eq. (24).

### C. Femtosecond Walk-Off Solitons

Multimode solitons result from a balance between (modal and chromatic) dispersion and Kerr nonlinearity. This means that, on the one hand, as discussed in the previous subsection, a stronger nonlinearity, due to the larger mode area of HOMs, is required for an MMS to form, compared with singlemode fiber solitons. Simultaneously, the nonlinearity must counteract not only chromatic dispersion-induced pulse broadening, but also modal walk-off effects.

Typically (i.e., for pulses of picosecond duration or longer), the walk-off length  $L_W$  between fiber modes [Eq. (15)] is much shorter than the chromatic dispersion length  $L_D$  [Eq. (16)] [see Figs. 4(b) and 4(c)]. On the other hand, as discussed in Sections 3 and 4, the most favorable condition for the formation of an MMS by nonlinear trapping of pulses carried in different fiber modes occurs when modal (or walk-off) and chromatic dispersion lengths are equal [see Eq. (22) in Section 2.D]. In this case, one minimizes the amount of

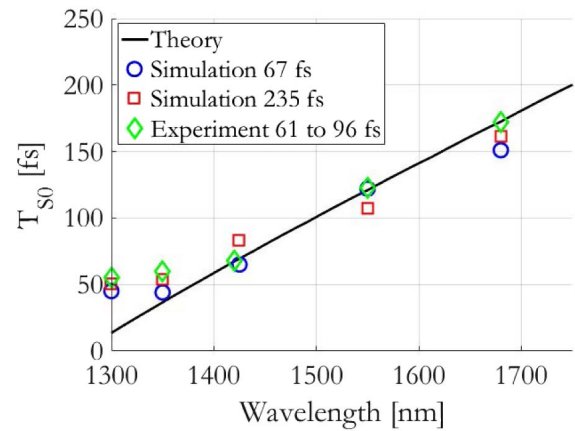


**Fig. 32.** Soliton pulse duration versus wavelength, compared with measured (green diamonds), simulated (empty red circles and blue squares, respectively), and with Eq. (208) (solid line). Reprinted with permission from Ref. [37]. Copyright 2021, Nature Group.

nonlinearity, which is necessary for trapping a pulse via the simultaneous nonlinear compensation of both intramodal and intermodal dispersions. It turns out that the condition  $L_W \simeq L_D$  can be achieved with femtosecond pulses, by taking advantage of the different scalings with pulsewidth  $T_0$  of  $L_D$  and  $L_W$  [37]. In this case, the temporal duration, say,  $T_w$ , of the MMS turns out to be fixed by the condition

$$T_0 = T_w = C \frac{|\beta_2|}{|\Delta\beta'_1|}, \quad (208)$$

where  $C$  is a constant of the order of unity. An experimental verification of Eq. (208) was carried out in Ref. [37]: in Fig. 32 we show that the MMS temporal duration is a constant at each wavelength, irrespective of the initial femtosecond pulse duration. The variation of  $T_w$  with wavelength is due to the chromatic dispersion slope. The experimental points refer to: 1 m of GRIN fiber, with input wavelength and pulse width 1300 nm and 61 fs, or 1420 nm and 70 fs, respectively; or 6 m of GRIN fiber, with input wavelength and pulse width 1550 nm and 67 fs, or 1680 nm and 96 fs, respectively.

### D. Multimode Soliton Fission

For relatively large input pulse energies, so that multiple MMSs are generated, the initial pulse gets temporally compressed at first, and subsequently undergoes Raman-induced fission into multiple fundamental solitons and dispersive waves [62]. As shown in Fig. 33, an initial beam mostly composed of HOMs is progressively cleaned into a bell-shaped beam composed of LOMs, as the input pulse energy grows larger. Moreover, long-pass filtering permits to leave out the Raman-shifted soliton: as can be seen, the soliton emerges from the input high-order MMS fission with a spatial bell shape, indicating that it is essentially carried by the fundamental mode of the fiber [135].

The process of soliton fission has been extensively investigated by using a short span (20 cm) of GRIN fiber and input femtosecond pulses with up to megawatt peak power, approaching the level for catastrophic self-focusing [36]. Figure 34 compares experimental data and numerical simulations for the variation of the output pulse width as a function of

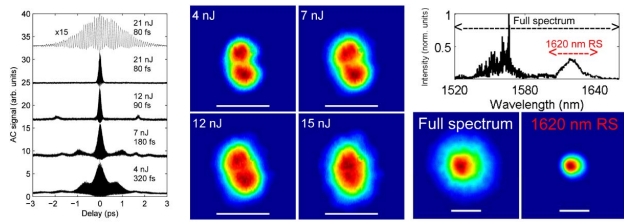


**Fig. 33.** Experimental study of high-order soliton fission in GRIN fiber. Left, autocorrelation of the output pulse versus input energy; middle, corresponding output beam profiles; right, output spectrum. Reprinted with permission from Ref. [62]. Copyright 2015, Optical Society of America.

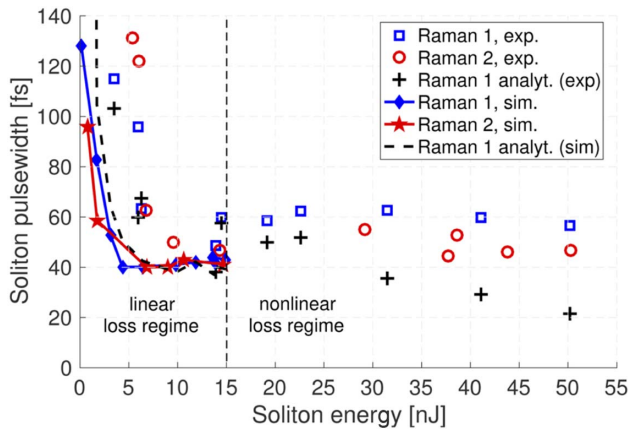


**Fig. 34.** Experimental data (empty squares and empty circles for first and second Raman solitons, respectively) versus numerical simulations (solid curves) for the output soliton time width versus its energy; black crosses and black dashed line are obtained from Eq. (24) by using experimental or simulation soliton parameters, respectively. Reprinted with permission from Ref. [36]. Copyright 2020, Optical Society of America.

its energy for the first and the second Raman MMSs that are generated by the fission. In Fig. 34, the black dashed line (black crosses) is obtained from Eq. (24) with the nominal (experimental) soliton parameters.

As can be seen, to the left of the vertical dashed line (here called the “linear-loss” regime), for soliton energies  $\mathcal{E} < 15$  nJ, although the trend is the same, for a given pulse duration  $T_0$  the energy of Raman solitons is always much larger than the value obtained from the single-mode relationship of Eq. (24).

On the other hand, Fig. 34 shows that to the right of the vertical dashed line (here called the “nonlinear-loss” regime, because multiphoton absorption effects are present) the experimentally observed soliton pulse durations remain nearly constant as the pulse energy grows larger. This is confirmed by the experimental soliton spectra (not shown here), showing that all MM Raman-shifted solitons converge to nearly the same and constant pulse width, between 50 fs and 60 fs.

### E. Few-Mode Fiber Solitons

The intermediate case, i.e., between quasi-single-mode and highly multimode solitons, was experimentally studied in a

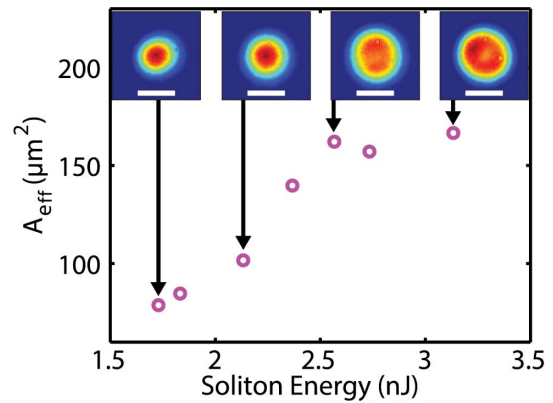


**Fig. 35.** Experimental dependence of MMS beam area versus soliton energy. Reprinted with permission from Ref. [136]. Copyright 2016, Optical Society of America.

so-called few-mode fiber (FMF) that supports the propagation of  $LP_{01}$ ,  $LP_{11a}$ , and  $LP_{11b}$  modes only, for a total of three spatial eigenmodes [136]. FMFs are of interest for optical communication links using the SDM technique [137]. For ultrashort pulses, the Raman effect splits the input pulse into dispersive waves, and temporally compressed red-shifting Raman solitons. The dependence of the SSFS on input pulse energy, and the modal composition of the generated MMS were investigated, and found to be in qualitative agreement with numerical simulations based on coupled GNLSs. Also in this case, the experiments have shown that, for a given pulse width, the MMS energy is typically found to be larger than that associated with a single-mode soliton carried within individual modes. Again, this result can be interpreted by considering that, for trapping modes with different linear group velocities, i.e., for overcoming intermodal dispersion, nonlinearity should be larger than the value that is necessary for compensating for the much weaker intramodal dispersion.

As can be seen in Fig. 35, these experiments have shown that the spatial beam width increases with the soliton energy. At low energies ( $1.5 < \mathcal{E} < 2.5$  nJ) the soliton beam has a Gaussian shape. On the other hand, at higher pulse energies the soliton is carried by a multimode superposition [136]. This can be explained by the fact that higher pulse energies permit to bind a larger proportion of HOMs.

Those experiments [136] have also shown that the MMS temporal duration remains inversely proportional to its energy, as described by the 1D soliton formula Eq. (21). This behavior is different from the case of (3D+1) spatiotemporal solitons in bulk media under the combined action of chromatic dispersion and diffraction: here the beam compresses both in time and in space when its energy grows larger.

### F. Solitons in Step-Index Fibers

The generation of MMS in SIMF has been a subject of different experimental studies [42,43,138,139]. In experiments by Zitelli *et al.* [43], ultrashort pulses of 70 fs duration at 1450 nm wavelength were introduced into a SIMF with a 50  $\mu\text{m}$  core diameter. That experiment involved two distinct input beam coupling conditions: axial and non-axial coupling.

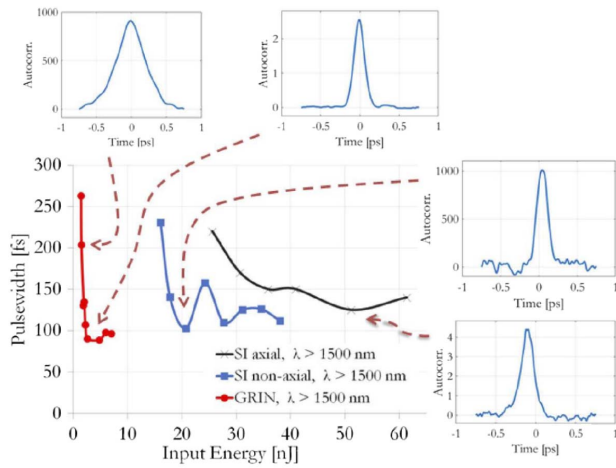


**Fig. 36.** Dependence of MMS temporal width on input pulse energy for GIMF (red curve), SIMF with axial (black curve) or non-axial (blue curve) input beam. Insets show examples of autocorrelation traces. Reprinted with permission from Ref. [43]. Copyright 2019, Optical Society of America.

Clearly, non-axial coupling facilitates the excitation of a larger amount of HOMs into the fiber. It was observed that non-axial coupling in SIMF leads to a lower energy threshold for MMS formation, when compared with axial coupling. An opposite behavior was observed when using GIMF. The reason for this difference lies in the fact that HOMs in SIMF (GIMF) have relatively higher (lower) nonlinear coefficients, owing to their smaller (larger) effective mode areas, as detailed in Section 2.E. The evolution of the generated MMS temporal width with increasing input energy is depicted in Fig. 36. As can be seen, the initial trend of a decreasing pulse width is followed by an oscillation of the output pulse duration around a fixed value as the pulse energy grows larger. Figure 36 also shows that a GIMF has a much lower energy threshold for MMS generation when compared with a SIMF. In any case, for both input coupling conditions, fundamental mode-based Raman MMSs emerge at the fiber output.

More recently, Wu *et al.* [42] have theoretically and experimentally studied the emergence of highly multimode MMSs in SIMFs in a high input pulse energy regime. These MMSs are characterized by superpositions of 5–10 temporally aligned transverse modes, resulting in speckled beam profiles and complex spatio-spectral variations across the MMS, as illustrated in Fig. 37. In a representative experiment, a Gaussian pulse at 1550 nm wavelength with a 500 fs duration was launched into a SIMF, requiring an input pulse energy reaching a maximum of up to 720 nJ, in order to induce a sufficient nonlinearity: this is a notably higher requirement when compared to the previous study [43]. Remarkably, irrespective of the excitation conditions that were employed, the resulting MMSs consistently comprised superpositions of HOMs. Again, this phenomenon can be understood by recognizing that HOMs exhibit a relatively smaller effective mode area, as shown in Fig. 3(e) in Section 2.E. Consequently, HOMs possess heightened nonlinearity compared to LOMs during mode competition, thereby facilitating the formation of highly multimode MMSs.

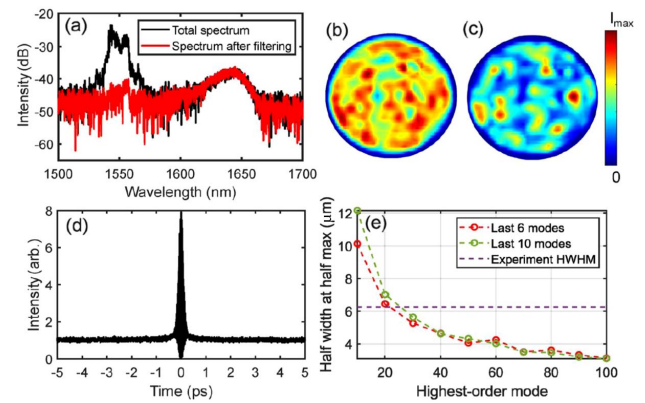


**Fig. 37.** (a) Total (black curve) and bandpass filtered (red curve) output spectrum from a step-index MMF; output spatial intensity profile before (b) and after (c) filtering; (d) spatially integrated pulse measurement; (e) simulated half width at half maximum of the spatial correlation function for randomly generated beam patterns from the last six modes (red) and the last ten modes (green), with highest-order mode indicated on  $x$ -axis; purple dashed line: half-width of the experimental spatial correlation function. Reprinted with permission from Ref. [42]. Copyright 2023, American Institute of Physics.

Utilizing SIMFs, it has been demonstrated both numerically and experimentally that Raman gain can facilitate energy transfer between single-mode solitons carried by different HOMs [138,139]. This phenomenon is referred to as soliton self-mode conversion (SSMC). In SIMFs, the group velocities of different spatial modes exhibit a considerable variation. This allows spectrally separated pulses in different modes to co-propagate at the same group velocity. By meticulously selecting the modes and central frequencies of the pulses, it becomes possible to match the frequency separation required for group velocity equalization with the Raman gain peak, typically occurring near 13 THz. Under these optimized conditions, efficient energy transfer from one mode to another can occur through intermodal Raman scattering when solitons are launched into HOMs of a SIMF. The results of cutback experiments depicted in Fig. 38 illustrate the process [139]. A soliton pulse, with a duration of 100 fs and a wavelength of 1045 nm, is initially launched into the  $LP_{0,19}$  mode of a SIMF with a core diameter of 97  $\mu\text{m}$ . This specific mode is excited in the fiber by encoding the spatial phase onto a Gaussian beam using a spatial light modulator. Upon propagation, the soliton formed in the  $LP_{0,19}$  mode undergoes red-shifting via conventional SSFS to 1141 nm after 33 cm. At this point, it becomes group-index matched to the  $LP_{0,18}$  mode with a frequency separation of 16 THz. Consequently, power transfers from the  $LP_{0,19}$  pulse to the  $LP_{0,18}$  mode pulse. After approximately 40 cm of propagation, the mode and wavelength conversion process is completed. Subsequently, the new fundamental soliton in the  $LP_{0,18}$  mode experiences further red-shifting to 1257 nm via SSFS. At this wavelength, it becomes group-index matched to the  $LP_{0,17}$  mode with a 14 THz frequency separation. Again, through SSMC, full power transfer to the  $LP_{0,17}$  mode is achieved with further propagation. These alternating SSFS and SSMC processes repeat along the fiber, ultimately resulting

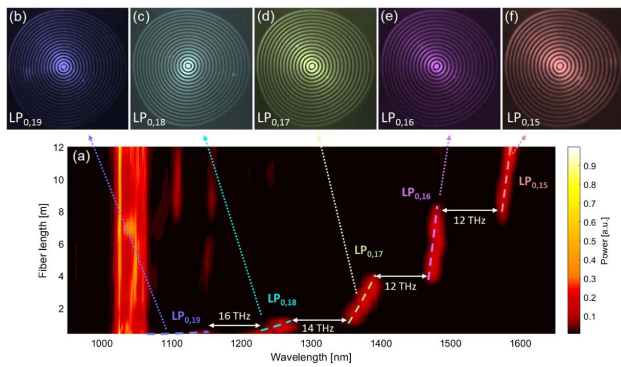


**Fig. 38.** Cutback experiments. (a) Spectra as a function of fiber length with input pulse at 1045 nm in the LP<sub>0,19</sub> mode. (b)–(f) Output mode images from different bandpass filters. Reprinted with permission from Ref. [139]. Copyright 2019, Optical Society of America.

in obtaining a pulse at 1587 nm in a pure LP<sub>0,15</sub> mode at the longest fiber length.

### G. Emergence of Soliton Attractors from Long Multimode Fibers

A pioneering experimental study of soliton generation in a GIMF has shown that femtosecond Raman solitons emerge from a relatively long length of fiber [135]. In their study, Grudinin *et al.* launched into the fiber 150 ps pulses from a Q-switched and mode-locked Nd:YAG laser: these pulses excite a multitude of modes at this wavelength. Surprisingly, the experiments have shown that, as a result of the generation of multiple Raman scattering Stokes sidebands, a supercontinuum is formed in the anomalous dispersion region of the fiber. From the supercontinuum a single Raman shifted soliton emerges, with a nearly single-mode beam, whose waist is close to that of the fundamental mode of the fiber. It was speculated that such Raman soliton beam cleaning is a manifestation of a universal property of nonlinear multimode systems [140]. Namely, energy redistribution among all fiber modes, or thermalization, eventually gives way to confinement into the first few low-order modes only.

To date, the properties of the original fascinating discovery remain yet to be fully explained: they appear to be a combined manifestation of Raman beam cleanup [63] and Kerr-induced beam self-cleaning [49]. In those experiments, it was observed that Raman solitons that are formed in GIMF have a peak power (or energy) about six times larger than that of a single-mode fiber soliton with the same pulse duration. Moreover, the spatial field distribution of these multimode Raman solitons is stable and quasi-single-mode, whenever the power of the input pulses grows larger than a certain threshold value. Equivalently, the same properties are observed whenever the GIMF length increases from 10 m to 500 m [135].

The emergence of solitons in MMFs can be seen as a fundamental manifestation of the robustness of solitons as attractors in weakly nonlinear turbulent wave systems, as discussed by Zakharov *et al.* [141,142]. This hypothesis has received a recent interesting experimental confirmation in studies of femtosecond soliton propagation of relatively long (up to 1 km)

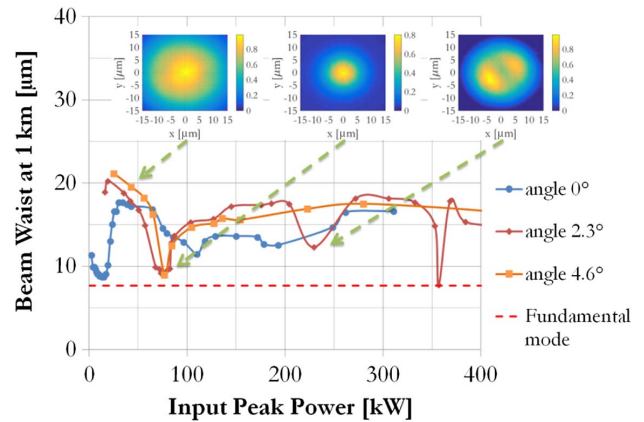


**Fig. 39.** Experimental study of MMS attractor in GIMF. Here we show the output beam waist after 1 km of GRIN fiber, versus input peak power, and 0°, 2.3°, and 4.6° input beam tilt angles; the dashed horizontal line indicates the fundamental beam waist. Insets illustrate the output beam shapes at selected powers. Reprinted with permission from Ref. [38]. Copyright 2021, Optical Society of America.

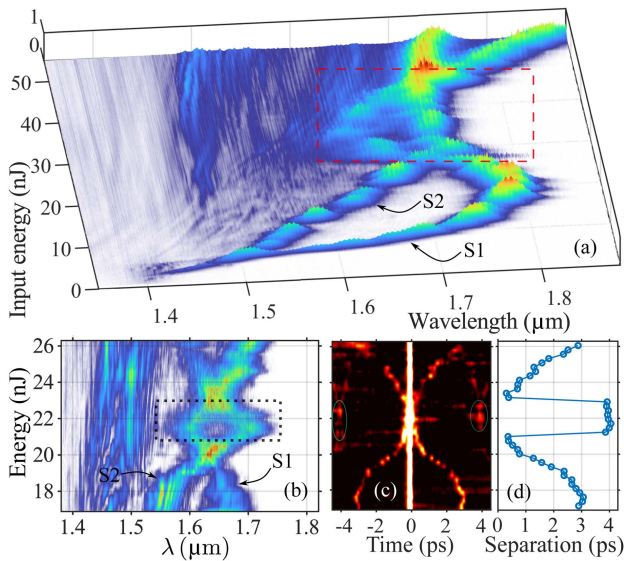
spans of GIMF [38]. In those experiments, ultrashort (70 fs) pulses at 1550 nm wavelength were injected in a 50/125 standard GIMF. The input laser beam was focused at the fiber end face with an approximately 15 μm waist. Moreover, the beam was injected at different small angular tilts with respect to the fiber axis for controlling the excitation of higher-order modes besides the fundamental.

Figure 39 illustrates experimentally observed dependence on input pulse peak power of the output beam waist after 1 km of fiber [38]. For 0° input tilt, a nearly monomode soliton (with a waist close to that of the fundamental mode) is formed at 15 kW. For initially tilted and highly multimode beams, the monomode fundamental soliton still emerges, but at a comparatively higher power, as shown by the beam compression effect, which occurs at about 80 kW. In all cases, the beam quality parameter of the emerging soliton was  $M^2 \approx 1.4$ .

### H. Soliton-Soliton Collision Experiments

Understanding soliton interactions in optical fibers, particularly how they evolve over propagation distance, poses a significant experimental challenge due to the intricacies of cutback experiments. Even slight adjustments in fiber positioning can yield vastly different outcomes. To circumvent this issue, in Ref. [39], researchers have turned to studying the interaction of two MMSs, generated by Raman MMS fission, by varying the input pulse energy. This approach, motivated by their simulations in Ref. [39], enables the examination of soliton interactions by observing variations in output spectra and temporal traces as the input energy changes. The positioning of soliton interactions is manipulated by adjusting the input pulse energy (see Fig. 11 in Section 3.B.2).

In their experimental investigation, Sun *et al.* [39] study the dynamics of soliton collisions within GIMF by varying the energy of an input pulse with 70 fs duration at 1400 nm wavelength. To capture high-resolution output spectrum evolution with input energy, the experimental setup integrates motorized-polarizer-based input power control with automated recording



**Fig. 40.** Soliton collision experiments. (a) Evolution of output spectrum versus input pulse energy for a 10 m GRIN fiber. (b) Output spectrum, (c) autocorrelation, and (d) soliton temporal separation versus input energy for a 2 m GRIN fiber. Reprinted with permission from Ref. [39]. Copyright 2022, Optical Society of America.

of output spectra and input power measurements using a spectrometer and power meter, respectively. These components are seamlessly coordinated and controlled by a computer, ensuring synchronization during data acquisition throughout the experiment. By slightly offsetting the input beam to introduce more HOMs, they obtained Fig. 40(a), illustrating the evolution of measured output spectra concerning input pulse energy ( $\mathcal{E}$ ) over a 10 m GRIN fiber length, which shows striking similarities to simulation results in Fig. 11. For  $\mathcal{E} > 6$  nJ, the input pulse's fission produced MMSs S2 and S1. As the input energy increases, two MMSs experience significant SSFS. Further increasing  $\mathcal{E}$  leads to the unconventional SSFS in S1, characterized by a relative “blue-shift” as depicted in Fig. 40(a), due to the reduced LOM content in S1. Notably, the spectral overlap with fringe shape occurred at a region of  $\mathcal{E} \simeq 27$  nJ, indicating that collisions [e.g., Figs. 11(d)–11(h)] may appear in the red dashed box. Finally, for  $\mathcal{E} > 45$  nJ, both solitons (S1 and S2) reemerged as distinct entities.

In order to further investigate the dynamics of MMS collisions in both temporal and spectral domains, a similar experiment was carried out by using an  $L_1 = 2$  m GRIN fiber. Figures 40(b) and 40(c) report the measured output spectra and their corresponding autocorrelation traces across various input pulse energies. For  $\mathcal{E} < 19$  nJ, two MMSs are visible in both spectral and temporal domains. As  $\mathcal{E}$  increases, the spectra of the two MMSs get progressively closer, until their separation becomes indistinguishable. Fringe patterns within the spectrum emerge for energies  $20$  nJ  $< \mathcal{E} < 21$  nJ, corresponding to two MMSs with a temporal separation of less than 0.5 ps. For  $21$  nJ  $< \mathcal{E} < 23$  nJ, a dominant peak in the middle of the autocorrelation trace and a weak peak at  $\pm 4$  ps are observed, suggesting the presence of non-overlapping solitons at the fiber output.

The temporal separation of two MMS peaks is plotted in Fig. 40(d). As previously predicted in simulations, this temporal separation is due to a collision at a position  $Z_c < L_1$  within the fiber [e.g., Figs. 11(d)–11(h)]. As a result, at the fiber output, the two MMSs emerge with a large temporal separation, owing to energy transfer from the leading MMS S2 to the trailing MMS S1 at the collision point, which enhances the red-shift and group delay for S1. For input energies exceeding the collision region ( $\mathcal{E} > 23$  nJ), Figs. 40(b) and 40(c) indicate a clear separation between the MMSs at the fiber output.

## I. Dispersive Wave Generation

Another fundamental mechanism that is known to play a key role in supercontinuum in single-mode fibers is the process of dispersive wave emission from MMSs, which can be interpreted in analogy with Cherenkov radiation in electrodynamics [143]. Experiments by Wright *et al.* revealed the formation of broad multi-octave supercontinuum spectra, which are characterized by the presence of an ultra-wideband series of sharp spectral peaks extending from the visible into the mid-infrared regions [59]. As the physical origin of these spectral peaks was not yet clear, they were referred to as mystery peaks.

A subsequent study [41] revealed that the mechanism underlying the formation of a series of spectral peaks (see Fig. 41) in the anomalous dispersion regime of the MMF is that of dispersive wave generation, resonantly phase-matched by the spatiotemporal intensity oscillations, due to self-imaging, of MMSs along the fiber. The mechanism is fully analogous to the multiple dispersive wave resonances of single-mode solitons that occur in fiber lasers or in periodically amplified optical fiber links [144]. Figure 41 shows that the supercontinuum featuring a series of unequally spaced dispersive wave peaks can be qualitatively well reproduced by using the generalized multimode coupled NLSEs [145]. As a matter of fact, the observed sideband peak positions can be well predicted by a simple reduction of the Gross-Pitaevskii equation Eq. (126) into a 1D NLSE with a periodically varying (because of MMS intensity oscillations due to self-imaging) nonlinear coefficient [41], as discussed in Section 6.

This phenomenon is clearly illustrated through comparable numerical examples presented in Figs. 25 and 26 in Section 6.C. These figures demonstrate that distinct peaks emerge as a result of the periodic evolution induced by the

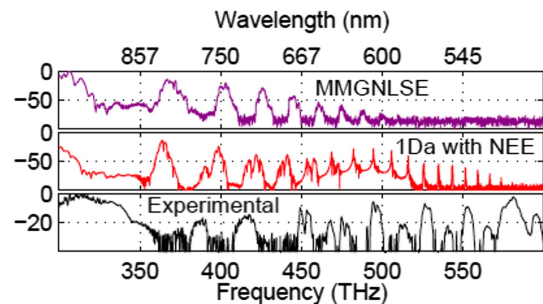


**Fig. 41.** Simulated (using the MM GNLSSE or the 1D NLSE model, respectively) and experimental generation of dispersive wave peaks in multimode GRIN fiber. Reprinted with permission from Ref. [41]. Copyright 2015, American Physical Society.

self-imaging effect, and conversely, these peaks vanish upon its removal. The resulting dynamics are essentially single-mode, and the sideband frequencies are determined by the phase-matching condition between the wave numbers of the soliton,  $k_{\text{sol}}$ , and that of the dispersive wave,  $k_{\text{dis}}$ , which reads as

$$k_{\text{sol}} - k_{\text{dis}} = 2m\pi/Z_c = \left(\frac{1}{2} + 4b_3^2 - 8b_3^4\right) + \left(\frac{\Omega^2}{2} + b_3\Omega^3\right), \quad (209)$$

where  $Z_c$  is the self-imaging period,  $\Omega$  is the frequency shift from the input pump pulse, and  $b_3$  is associated with third-order dispersion [41].

### J. Solitons in Hollow-Core and Capillary Multimode Fibers

Another frontier for MMS and spatiotemporal soliton phenomena is provided by intense optical pulse propagation in multimode hollow-core, gas-filled fibers, and capillaries [146]. Figure 42 presents a chronological overview of the dramatic (more than 10 orders of magnitude) peak power increase of fiber solitons when moving from standard single-mode fibers to specialty fibers such as bandgap, antiresonant hollow-core, and capillary fibers [147].

In gas-filled hollow-core fibers (HCFs), preferential guiding by the fundamental mode occurs at low powers, because of its low loss. As the input light intensity grows larger, ionization leads to plasma defocusing, which in turn excites HOMs. The resulting nonlinear mode coupling enables pulse compression, and sustains spatiotemporal localization leading to MMS propagation at powers below the self-focusing threshold [148–150].

In an interesting work by Safaei *et al.* [151], a high-energy (5 mJ) 700 fs laser pulse at 780 nm was coupled into the fundamental mode of a 3 m long HCF with a 500  $\mu\text{m}$  core size, filled with nitrogen. Because of self-focusing, the progressively spatially compressed pulse within the HCF coupled its energy away from the fundamental mode and into radially symmetric HOMs. The resulting MMS (also called a “multi-dimensional solitary state”) experienced a substantial Raman SSFS until a wide supercontinuum was generated. The emitted pulses were accompanied by a high spatial beam quality and exhibited a negative quadratic spectral phase, which permitted their subsequent

dispersive compression down to 10 fs, thus providing a compact source for high-harmonic-generation applications.

When considering gas-filled hollow capillary fibers using the lightest noble gas with the highest ionization potential, helium, the MMS intensity is limited to about  $I_{\text{th}} \approx 3 \times 10^{14}$  W/cm<sup>2</sup>, before excessive gas ionization takes place [152]. For higher intensities, most of the input pulse energy is absorbed; moreover, a huge amount of self-phase modulation is produced, which, in association with complex spatial mode-coupling, ultimately breaks down the soliton dynamics. Nevertheless, soliton generation in hollow-core optical fibers has enabled a new class of light sources, with unique properties. These include: extreme pulse compression; generation of tunable, few-cycle ultraviolet to visible pulses through resonant dispersive wave emission; and the production of tunable visible and infrared light via soliton frequency shifting. Light beams produced from these soliton-based sources have distinctive characteristics that are unachievable by other methods, with far-reaching potential for both fundamental science and technological applications [147].

## 10. CONCLUSIONS AND PERSPECTIVES

The exploration of MMSs in MMFs has revealed a rich landscape of nonlinear optical phenomena, advancing the understanding of soliton dynamics in complex media. In this review paper, we started with a tutorial on MMSs within MMFs in Section 2. This includes an analysis of the linear eigenmode properties of the two main types of multimode fibers: SIMFs and GIMFs. We highlight the key fiber properties that influence the formation of multimode solitons, thereby setting the groundwork for understanding their role in soliton generation. Of course, fiber types are not limited to SIMFs and GIMFs; however, the framework to evaluate a fiber’s performance remains consistent, as illustrated in Fig. 2. One can design a fiber based on the transverse refractive index geometry and the nonlinear material response. Generally, dispersion management strategies are crucial for optimizing system performance. These strategies, including minimizing the modal walk-off length  $L_W$  and increasing nonlinear coefficients, may reduce the power threshold for MMS formation. By carefully managing these parameters, the overall efficiency and effectiveness of optical fiber systems can be significantly enhanced.

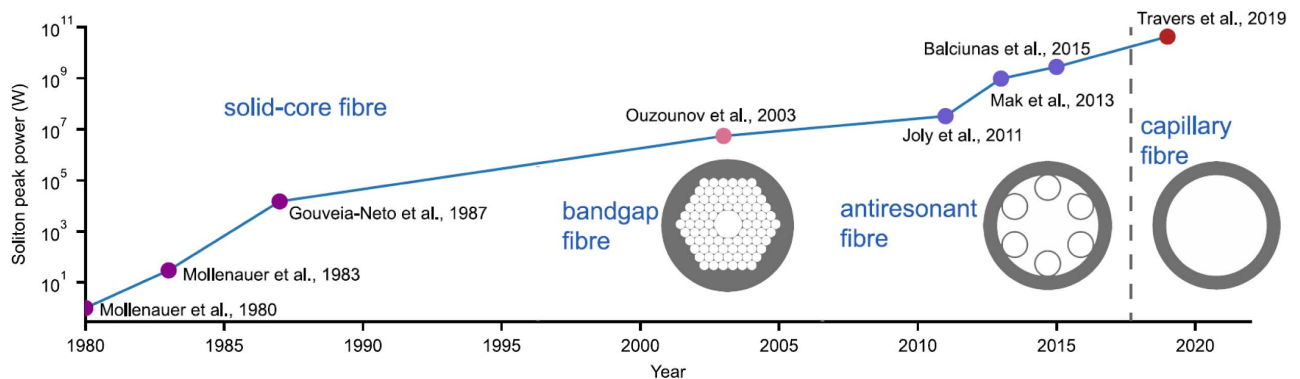


**Fig. 42.** Temporal evolution of soliton peak power in different fiber structures (in the insets, glass is depicted in gray, while white indicates empty spaces). Reprinted with permission from Ref. [147]. Copyright 2024, Elsevier.

After familiarizing with the fundamental concepts, we introduced the GMMNLSE in Section 3, which is relevant to describing a wide range of MMFs with distinguishable eigenmodes. We then provided succinct examples, ranging from linear multimode pulse walk-off to the formation of an MMS, including phenomena such as the SSFS, soliton fission, and soliton collision processes. These examples effectively elucidate the concepts discussed in Section 2, thereby establishing a robust foundation for further analytical and experimental exploration. These concepts and the model are not only applicable to studying MMSs in MMFs but also prove valuable in the design of spatiotemporal mode-locked lasers [44–46].

Understanding the impact of modal walk-off is particularly crucial in the formation of MMSs. In Section 4, we provide a comprehensive review of the theoretical framework underpinning the dynamics of MMSs with two modes, utilizing a simplified coupled mode model. Much of these findings can be derived from the variational formulation of the GMMNLSE, which aids in the creation of effective theories that describe an MMS with a reduced number of degrees of freedom. Our primary focus is on the formation of two-mode solitons, and we employ the variational formulation, the Kantorovich approach, and the virial (or moment) method to analyze these solitons. This analysis is further extended to a multimode context, thereby generalizing the previously discussed theories. Nevertheless, theoretical investigations of MMS with multiple modes present significant challenges and opportunities.

Similar analytical approaches can be applied to study STS in the 3D+1 NLSE within GIMFs. In Section 5, we review the primary theoretical results concerning the formation and stability of STSs in the 3D+1 dimensional framework for GIMFs. Our focus is on the variational formulation as the main tool for gaining analytical insights into the properties of these states. This approach allows us to obtain analytical solutions for spatiotemporal MMSs in regimes below the energy threshold. High-order dispersion is found to stabilize these STS states. Furthermore, these STSs primarily arise from solitons carrying fundamental modes with a small amount of high-order mode content, as we mainly consider ansatzes expressed in terms of fundamental modes. Potential directions for studying higher-order STS can be explored by considering ansatzes that include high-order modes.

To reduce the complexity of high-dimensional systems and enhance computational efficiency, in Section 6, we simplify the 3D+1 NLSE to a 1D+1 NLSE form by leveraging the periodic evolution of short optical pulses within a GIMF. We discuss the practical conditions under which the effective 1D NLSE can be applied, and provide several examples of MMSs exhibiting self-imaging, including GRIN soliton formation, and the influence of higher-order effects. This method is particularly efficient numerically and simplifies the implementation of analytical analysis, making it a valuable tool for studying complex multimode fiber dynamics.

The complexity of the coupling terms in the GMMNLSE imposes significant computational challenges when considering a large number of modes. One approach to mitigate this issue is to simulate the full field in the temporal domain, rather than

dealing directly with the coupling terms of the mode amplitudes. In Section 7, we present an innovative Gaussian quadrature approach for numerical simulations of the generalized NLSE. This method employs a mode decomposition based on the fiber's natural eigenmodes, utilizing an optimized quadrature scheme for weighted orthogonal polynomials to enhance computational efficiency. We begin with a radially symmetric model and then extend our approach to a 3D+1 quadrature model, providing illustrative examples of the results. A major advantage of using Gaussian quadratures, instead of relying on spatial Fourier transforms, is that separate dispersive phase shifts can be efficiently handled for each mode through frequency-dependent matrix multiplication during the linear step.

When considering long-distance propagation in SDM optical communications within multimode fibers, perturbations caused by fiber imperfections and environmental factors can amplify the influence of linear propagation effects. These linear perturbation effects can significantly impact the dynamics of MMS via random mode coupling. To accurately model this phenomenon, additional terms are required, which can be effectively described using a generalized Jones formalism. In Section 8, we review the model and illustrate its application with examples demonstrating how mode-dispersion coefficients degrade MMS propagation.

In Section 9, we overview recent experiments involving MMS, spanning various regimes such as the quasi-single-mode and fully multimode domains. These experiments encompass a diverse array of phenomena, including femtosecond walk-off solitons, MMS fission, and solitons in SIMF. Additionally, we explore the emergence of soliton attractors from long MMF, investigate soliton-soliton collision dynamics, and examine dispersive wave generation. We envisage that potentially new research directions for MMS may involve additional topics such as single pulse mode decomposition techniques, high-power fiber damage threshold, and high-order mode MMS spatial beam shaping.

Despite evident advances in understanding MMSs, numerous questions persist. For instance, how can we quantitatively assess the formation conditions of MMSs for modal walk-off compensation, considering varying mode orders and modal group velocities, especially when there is a significant disparity in mode order? Does mode beating degrade or enhance the stability of MMSs? Are there qualitatively distinct types of MMSs, such as those featuring high-order modes with coherent beam quality? Can optical frequency conversion be achieved by exploiting the self-imaging effect? What strategies can enhance our ability to control MMSs interactions by manipulating their propagation speed? How can we better manipulate the propagation speed of MMSs to control their interaction? How do MMSs propagate under conditions of weak mode coupling or mode-dependent loss? How do MMSs evolve in environments with strong or weak disorder? What impact do plasma interactions have on MMSs? These questions represent intriguing areas for further exploration. Additionally, for modeling very-high-energy soliton dynamics, particularly in hollow-core fibers [153], the full vector polarization model [154,155] demonstrates strong similarities between simulations and

experiments even when the peak power reaches terawatt levels [156].

To efficiently explore diverse soliton solutions within the framework of the GMMNLSE, 3D+1 NLSE, and 1D+1 NLSE models, both analytical and numerical methods are crucial. In this review, we combined analytical techniques (e.g., the variational approach; see Sections 4 and 5) with direct numerical solutions based on the familiar split-step method (Sections 2, 3, and 6) or using newly developed techniques such as the Gaussian quadrature approach (Section 7). Recently, the strong data-fitting capabilities of machine learning (ML) have gained popularity in ultrafast optics, based on the use of neural networks [157,158]. These ML algorithms establish relationships between the input conditions and the output variables within a constrained dynamical space, based on output data from physical models, which may not adhere to the system dynamics beyond this limited space. Since 2019, physics-informed neural networks (PINNs) have garnered significant attention for solving partial differential equations (PDEs) [159–161]. PINNs integrate model equations, like PDEs, directly into the neural network architecture, resulting in physics-supervised neural networks. Substantial research has focused on nonlinear optics within the NLSE framework [162–168], investigating vector solitons in birefringent fibers [162–164], higher-order terms [168], GMMNLSE [165], and three-component coupled NLSE [167]. Future research could further benefit from applying PINNs to 3D+1, 1D+1, and GMMNLSE models for MMS studies.

We would like to dedicate this review to Bruno Crosignani, a pioneer in multimode fiber solitons, who recently passed away. To some of us, he has been a mentor in soliton research, a dear friend, and a precious source of inspiration in science. We are deeply grateful to all of our many collaborators in the field of multimode optical solitons. We also thank the anonymous reviewers for their constructive remarks.

## APPENDIX A: ABBREVIATION

Here we list the abbreviations in Table 1.

## APPENDIX B: MODE DECOMPOSITION OF AN INPUT GAUSSIAN PULSE

In this appendix, we detail the procedure for computing the input mode distribution, when taking into account the specific input beam coupling conditions, which are encountered experimentally.

In order to determine the input mode distribution, it is crucial to know the waist of the input laser beam (supposed to be Gaussian) and its displacement relative to the central axis of the fiber. Let us first focus on the specific case of a Gaussian beam that is injected into the fiber core, with an offset  $(x_0, y_0)$  from the fiber axis. Hence, the beam at the fiber input facet is described by

$$E_{\text{in}}(x, y) = \frac{1}{\sigma\sqrt{\pi}} e^{-\frac{(x-x_0)^2+(y-y_0)^2}{2\sigma^2}}, \quad (\text{B1})$$

where  $\sigma$  is related to the beam full width at half maximum (FWHM) of its intensity  $|E_{\text{in}}(x, y)|^2$ , or beam size  $w = \sigma/1.665$ , under the normalization condition

**Table 1. List of Abbreviations**

Abbreviations	Definitions
CW	Continuous wave
DMD	Differential mode delay
FMF	Few-mode fiber
FWHM	Full width at half maximum
FWM	Four-wave mixing
GIMF	Graded-index multimode fiber
GMMNLSE	Generalized multimode NLSE
GNLSE	Generalized NLSE
GPI	Geometric parametric instability
GRIN	Graded index
GVD	Group-velocity dispersion
HOM	High-order mode
IIR	Fiber intensity impulse response
LG modes	Laguerre-Gaussian modes
LOM	Low-order mode
MCF	Multi-core fiber
MD	Spatial mode dispersion
MEA	Mode's effective area
MIMO	Multiple-input-multiple-output
MMF	Multimode fiber
MMS	Multimode soliton
MNC	Modal nonlinear coefficient
MNL	Modal nonlinear length
NLSE	Nonlinear Schrödinger equation
PDE	Partial differential equation
PINN	Physics-informed neural network
PMD	Polarization-mode dispersion
SDM	Space-division multiplexing
SIMF	Step-index multimode fiber
SPM	Self-phase modulation
STS	Spatiotemporal soliton
VKS	Vakhitov-Kolokolov stability
XPM	Cross-phase modulation
ZDW	Zero-dispersion wavelength

$$\int_{-\infty}^{\infty} \int_{-\infty}^{\infty} |E_{\text{in}}(x, y)|^2 dx dy = 1. \quad (\text{B2})$$

Projecting this input beam onto the eigenmode basis, we obtain the input modal coefficients

$$C_p = \int_{-\infty}^{\infty} \int_{-\infty}^{\infty} E_{\text{in}}(x, y) \cdot F_p(x, y) dx dy. \quad (\text{B3})$$

Given that the eigenmodes  $F_p(x, y)$  are normalized, the coefficients  $|C_p|^2$  quantify the power fraction of mode  $p$ , ensuring energy conservation:

$$\sum_{p=1}^N |C_p|^2 = 1. \quad (\text{B4})$$

For a nuanced analysis of the input beam size and displacement, we normalize both parameters against the FWHM or waist  $w_{\text{mode}, p=1}$  of the fundamental mode, by introducing the two parameters  $r_w$  and  $r_s$ :

$$r_w = w/w_{\text{mode}, p=1} \quad (\text{B5})$$

$$r_s = x_0/w_{\text{mode}, p=1}. \quad (\text{B6})$$

By manipulating  $r_w$  and  $r_s$ , we may explore the variation of the input mode content  $E_{\text{in}}(x, y)$  for different Gaussian beam profiles. In Fig. 43, we illustrate how the input mode content



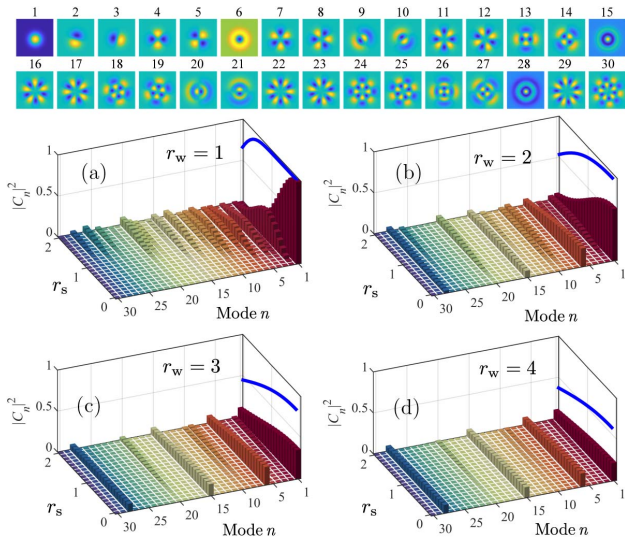


**Fig. 43.** Decomposition of a Gaussian beam into the first  $N = 30$  modes of a GIMF, with panels (a)–(d) showing mode coefficients  $|C_p|^2$  against the beam lateral offset  $r_s$  for beam widths  $r_w = 1, 2, 3, 4$ . Radial modes ( $p = 1, 6, 15, 28$ ) are predominantly excited at precise center alignment ( $r_s = 0$ ). The blue lines in (a)–(d) indicate the total power fraction  $\sum_{p=1}^N |C_p|^2$  as a function of  $r_s$ . Values below one result from the finite number of modes considered.

shifts with  $r_s$  across four distinct  $r_w$  values, when considering up to  $N = 30$  modes. Notably, when the Gaussian beam width matches that of the fundamental mode ( $r_w = 1$  and  $r_s = 0$ ), the mode content simplifies to  $|C_1|^2 = 1$  with  $|C_p|^2 = 0$  for  $p > 1$ , indicating a pure fundamental mode excitation. Note that radial modes, specifically those indexed as  $p = 1, 6, 15, 28$ , are predominantly excited when the beam is precisely centered at the fiber axis, providing that there is no lateral shift, i.e.,  $r_s \neq 0$ . Conversely, deviations in either  $r_w$  or  $r_s$  from unity yield a more complex input mode distribution.

The blue lines in Fig. 43 depict the variation of the quantity  $\sum_{p=1}^N |C_p|^2$  as a function of the beam lateral offset  $r_s$  from the fiber axis. A decline in the blue curve values occurs because beams characterized by relatively large values of  $r_w$  or  $r_s$  cannot be fully represented by merely  $N = 30$  modes. Naturally, enhancing the number of modes considered in the decomposition analysis improves its precision, thereby enabling the accurate decomposition of beams with larger  $r_w$  and  $r_s$  dimensions, albeit at the cost of an increased computational time.

For numerical implementations, if a beam cannot be fully represented by the limited number of total modes  $N$ , indicated by  $\sum_{p=1}^N |C_p|^2 < 1$ , it becomes necessary to adjust the mode coefficients to  $C'_p = \sqrt{C_p / \sum_{p=1}^N |C_p|^2}$  for all modes. This adjustment ensures that the ratio of mode energies remains a constant, while the corrected coefficients satisfy  $\sum_{p=1}^N |C'_p|^2 = 1$ , thus preserving the total energy distribution among the modes.

To express the temporal input profile of the field, we assume that at the fiber input ( $z = 0$ ), all modes share identical temporal shapes. Specifically, a Gaussian temporal profile is presumed, centered at  $t_0$  and characterized by a duration  $T_{\text{FWHM}} = T_0/1.665$ , outlined as

$$A_p(z = 0, t) = C_p \sqrt{\frac{\mathcal{E}}{T_0 \sqrt{\pi}}} e^{-\frac{(t-t_0)^2}{2T_0^2}}. \quad (\text{B7})$$

Thus, we may obtain the input condition for all modal amplitudes  $A_p$  for a given pulse with input energy  $\mathcal{E}$  and beam values  $r_w$  and  $r_s$ . Given that the mode field power is defined by  $|A_p(z, t)|^2$ , the total energy of the input pulse satisfies  $\mathcal{E} = \sum_{p=1}^N \int_{-\infty}^{\infty} |A_p(z = 0, t)|^2 dt$ , ensuring the conservation of the total input energy across all modes.

**Funding.** H2020 European Research Council (740355); H2020 Marie Skłodowska-Curie Actions (101023717); HORIZON EUROPE Marie Skłodowska-Curie Actions (101064614); Sapienza Università di Roma (EFFILOCKER, NOSTERDIS); Ministero dell'Istruzione e del Merito (ECS00000041 VITALITY - CUP E13C22001060006, PE00000001 - program "RESTART"); Olle Engkvists Stiftelse (214-0328).

**Acknowledgment.** We acknowledge the financial support from the European Research Council Advanced Grant STEMS; Marie Skłodowska-Curie Actions; Sapienza University; European Union under the Italian National Recovery and Resilience Plan (NRRP) of NextGenerationEU, partnership on "Telecommunications of the Future"; European Union - NextGenerationEU under the Italian Ministry of University and Research (MUR) National Innovation Ecosystem; and Olle Engkvist Foundation.

**Disclosures.** The authors declare no conflicts of interest.

**Data Availability.** Data underlying the results presented in this paper are not publicly available at this time but may be obtained from the authors upon reasonable request.

## REFERENCES

1. A. Blanco-Redondo, C. M. de Sterke, C. Xu, *et al.*, "The bright prospects of optical solitons after 50 years," *Nat. Photonics* **17**, 937–942 (2023).
2. J. M. Dudley, C. Finot, G. Genty, *et al.*, "Fifty years of fiber solitons," *Opt. Photon. News* **34**, 26–33 (2023).
3. A. Hasegawa and F. Tappert, "Transmission of stationary nonlinear optical pulses in dispersive dielectric fibers. I. Anomalous dispersion," *Appl. Phys. Lett.* **23**, 142–144 (1973).
4. L. F. Mollenauer, R. H. Stolen, and J. P. Gordon, "Experimental observation of picosecond pulse narrowing and solitons in optical fibers," *Phys. Rev. Lett.* **45**, 1095–1098 (1980).
5. Y. S. Kivshar and G. P. Agrawal, *Optical Solitons: From Fibers to Photonic Crystals* (Academic, 2003).
6. A. Hasegawa, "Soliton-based optical communications: an overview," *IEEE J. Sel. Top. Quantum Electron.* **6**, 1161–1172 (2000).
7. J. M. Dudley, G. Genty, and S. Coen, "Supercontinuum generation in photonic crystal fiber," *Rev. Mod. Phys.* **78**, 1135–1184 (2006).
8. J. Kim and Y. Song, "Ultralow-noise mode-locked fiber lasers and frequency combs: principles, status, and applications," *Adv. Opt. Photon.* **8**, 465–540 (2016).
9. F. Leo, S. Coen, P. Kockaert, *et al.*, "Temporal cavity solitons in one-dimensional Kerr media as bits in an all-optical buffer," *Nat. Photonics* **4**, 471–476 (2010).
10. G. Askaryan, "Effects of the gradient of a strong electromagnetic beam on electrons and atoms," *Sov. Phys. JETP* **15**, 1088–1090 (1962).

11. Z. Chen, M. Segev, and D. N. Christodoulides, "Optical spatial solitons: historical overview and recent advances," *Rep. Prog. Phys.* **75**, 086401 (2012).
12. G. I. Stegeman and M. Segev, "Optical spatial solitons and their interactions: universality and diversity," *Science* **286**, 1518–1523 (1999).
13. S. Trillo and W. Torruellas, *Spatial Solitons* (Springer, 2013), Vol. **82**.
14. G. I. Stegeman, D. N. Christodoulides, and M. Segev, "Optical spatial solitons: historical perspectives," *IEEE J. Sel. Top. Quantum Electron.* **6**, 1419–1427 (2000).
15. B. A. Malomed, *Multidimensional Solitons* (AIP, 2022).
16. Y. V. Kartashov, G. E. Astrakharchik, B. A. Malomed, *et al.*, "Frontiers in multidimensional self-trapping of nonlinear fields and matter," *Nat. Rev. Phys.* **1**, 185–197 (2019).
17. Y. Silberberg, "Collapse of optical pulses," *Opt. Lett.* **15**, 1282–1284 (1990).
18. L. Bergé, "Wave collapse in physics: principles and applications to light and plasma waves," *Phys. Rep.* **303**, 259–370 (1998).
19. E. A. Kuznetsov and F. Dias, "Bifurcations of solitons and their stability," *Phys. Rep.* **507**, 43–105 (2011).
20. P. Parra-Rivas, Y. Sun, and S. Wabnitz, "Dynamics of three-dimensional spatiotemporal solitons in multimode waveguides," *Opt. Commun.* **546**, 129749 (2023).
21. L. G. Wright, F. O. Wu, D. N. Christodoulides, *et al.*, "Physics of highly multimode nonlinear optical systems," *Nat. Phys.* **18**, 1018–1030 (2022).
22. R. McLeod, K. Wagner, and S. Blair, "(3+1)-dimensional optical soliton dragging logic," *Phys. Rev. A* **52**, 3254–3278 (1995).
23. M. Mitchell, M. Segev, and D. N. Christodoulides, "Observation of multihump multimode solitons," *Phys. Rev. Lett.* **80**, 4657–4660 (1998).
24. X. Liu, L. Qian, and F. Wise, "Generation of optical spatiotemporal solitons," *Phys. Rev. Lett.* **82**, 4631–4634 (1999).
25. S. Minardi, F. Eilenberger, Y. V. Kartashov, *et al.*, "Three-dimensional light bullets in arrays of waveguides," *Phys. Rev. Lett.* **105**, 263901 (2010).
26. B. A. Malomed, D. Mihalache, F. Wise, *et al.*, "Spatiotemporal optical solitons," *J. Opt. B* **7**, R53 (2005).
27. S.-S. Yu, C.-H. Chien, Y. Lai, *et al.*, "Spatio-temporal solitary pulses in graded-index materials with Kerr nonlinearity," *Opt. Commun.* **119**, 167–170 (1995).
28. S. Raghavan and G. P. Agrawal, "Spatiotemporal solitons in inhomogeneous nonlinear media," *Opt. Commun.* **180**, 377–382 (2000).
29. F. Lederer, G. I. Stegeman, D. N. Christodoulides, *et al.*, "Discrete solitons in optics," *Phys. Rep.* **463**, 1–126 (2008).
30. S. Buch and G. P. Agrawal, "Soliton stability and trapping in multimode fibers," *Opt. Lett.* **40**, 225–228 (2015).
31. P. Parra-Rivas, Y. Sun, and S. Wabnitz, "Spatiotemporal soliton stability in multimode fibers: a Hamiltonian approach," *Optik* **287**, 171079 (2023).
32. K. Krupa, A. Tonello, A. Barthélémy, *et al.*, "Multimode nonlinear fiber optics, a spatiotemporal avenue," *APL Photon.* **4**, 110901 (2019).
33. A. Hasegawa, "Self-confinement of multimode optical pulse in a glass fiber," *Opt. Lett.* **5**, 416–417 (1980).
34. B. Crosignani and P. D. Porto, "Soliton propagation in multimode optical fibers," *Opt. Lett.* **6**, 329–330 (1981).
35. B. Crosignani, A. Cutolo, and P. D. Porto, "Coupled-mode theory of nonlinear propagation in multimode and single-mode fibers: envelope solitons and self-confinement," *J. Opt. Soc. Am.* **72**, 1136–1141 (1982).
36. M. Zitelli, F. Mangini, M. Ferraro, *et al.*, "High-energy soliton fission dynamics in multimode GRIN fiber," *Opt. Express* **28**, 20473–20488 (2020).
37. M. Zitelli, F. Mangini, M. Ferraro, *et al.*, "Conditions for walk-off soliton generation in a multimode fiber," *Commun. Phys.* **4**, 182 (2021).
38. M. Zitelli, M. Ferraro, F. Mangini, *et al.*, "Single-mode spatiotemporal soliton attractor in multimode GRIN fibers," *Photon. Res.* **9**, 741–748 (2021).
39. Y. Sun, M. Zitelli, M. Ferraro, *et al.*, "Multimode soliton collisions in graded-index optical fibers," *Opt. Express* **30**, 21710–21724 (2022).
40. M. Eftekhar, H. Lopez-Aviles, F. Wise, *et al.*, "General theory and observation of Cherenkov radiation induced by multimode solitons," *Commun. Phys.* **4**, 137 (2021).
41. L. G. Wright, S. Wabnitz, D. N. Christodoulides, *et al.*, "Ultrabroadband dispersive radiation by spatiotemporal oscillation of multimode waves," *Phys. Rev. Lett.* **115**, 223902 (2015).
42. Y. Wu, N. Bender, D. N. Christodoulides, *et al.*, "Highly multimode solitons in step-index optical fiber," *APL Photon.* **8**, 091301 (2023).
43. M. Zitelli, Y. Sun, M. Ferraro, *et al.*, "Multimode solitons in step-index fibers," *Opt. Express* **30**, 6300–6310 (2022).
44. B. Cao, C. Gao, K. Liu, *et al.*, "Spatiotemporal mode-locking and dissipative solitons in multimode fiber lasers," *Light Sci. Appl.* **12**, 260 (2023).
45. L. G. Wright, D. N. Christodoulides, and F. W. Wise, "Spatiotemporal mode-locking in multimode fiber lasers," *Science* **358**, 94–97 (2017).
46. Y. Ding, X. Xiao, K. Liu, *et al.*, "Spatiotemporal mode-locking in lasers with large modal dispersion," *Phys. Rev. Lett.* **126**, 093901 (2021).
47. Y. Sun, P. Parra-Rivas, C. Millán, *et al.*, "Robust three-dimensional high-order solitons and breathers in driven dissipative systems: a Kerr cavity realization," *Phys. Rev. Lett.* **131**, 137201 (2023).
48. M. Nie, K. Jia, Y. Xie, *et al.*, "Synthesized spatiotemporal mode-locking and photonic flywheel in multimode mesoresonators," *Nat. Commun.* **13**, 6395 (2022).
49. K. Krupa, A. Tonello, B. M. Shalaby, *et al.*, "Spatial beam self-cleaning in multimode fibres," *Nat. Photonics* **11**, 237–241 (2017).
50. F. O. Wu, A. U. Hassan, and D. N. Christodoulides, "Thermodynamic theory of highly multimoded nonlinear optical systems," *Nat. Photonics* **13**, 776–782 (2019).
51. F. Mangini, M. Gervaziev, M. Ferraro, *et al.*, "Statistical mechanics of beam self-cleaning in grin multimode optical fibers," *Opt. Express* **30**, 10850–10865 (2022).
52. H. Pourbeyram, P. Sidorenko, F. O. Wu, *et al.*, "Direct observations of thermalization to a Rayleigh–Jeans distribution in multimode optical fibres," *Nat. Phys.* **18**, 685–690 (2022).
53. Z. Eslami, L. Salmela, A. Filipkowski, *et al.*, "Two octave supercontinuum generation in a non-silica graded-index multimode fiber," *Nat. Commun.* **13**, 2126 (2022).
54. I. H. Malitson, "Interspecimen comparison of the refractive index of fused silica," *J. Opt. Soc. Am.* **55**, 1205–1209 (1965).
55. A. B. Fallahkhair, K. S. Li, and T. E. Murphy, "Vector finite difference modesolver for anisotropic dielectric waveguides," *J. Lightwave Technol.* **26**, 1423–1431 (2008).
56. G. P. Agrawal, *Nonlinear Fiber Optics*, 6th ed. (Elsevier, 2019).
57. T. Hansson, A. Tonello, T. Mansuryan, *et al.*, "Nonlinear beam self-imaging and self-focusing dynamics in a GRIN multimode optical fiber: theory and experiments," *Opt. Express* **28**, 24005–24021 (2020).
58. M. Ferraro, F. Mangini, Y. Sun, *et al.*, "Multiphoton ionization of standard optical fibers," *Photon. Res.* **10**, 1394–1400 (2022).
59. L. G. Wright, D. N. Christodoulides, and F. W. Wise, "Controllable spatiotemporal nonlinear effects in multimode fibres," *Nat. Photonics* **9**, 306–310 (2015).
60. K. Krupa, A. Tonello, A. Barthélémy, *et al.*, "Observation of geometric parametric instability induced by the periodic spatial self-imaging of multimode waves," *Phys. Rev. Lett.* **116**, 183901 (2016).
61. M. Zitelli, V. Couderc, M. Ferraro, *et al.*, "Spatiotemporal mode decomposition of ultrashort pulses in linear and nonlinear graded-index multimode fibers," *Photon. Res.* **11**, 750–756 (2023).
62. L. G. Wright, W. H. Renninger, D. N. Christodoulides, *et al.*, "Spatiotemporal dynamics of multimode optical solitons," *Opt. Express* **23**, 3492–3506 (2015).
63. N. B. Terry, T. G. Alley, and T. H. Russell, "An explanation of SRS beam cleanup in graded-index fibers and the absence of SRS beam cleanup in step-index fibers," *Opt. Express* **15**, 17509–17519 (2007).
64. P. Horak and F. Poletti, *Multimode Nonlinear Fibre Optics: Theory and Applications* (InTech, 2012), pp. 3–25.
65. L. G. Wright, Z. M. Ziegler, P. M. Lushnikov, *et al.*, "Multimode nonlinear fiber optics: massively parallel numerical solver, tutorial, and outlook," *IEEE J. Sel. Top. Quantum Electron.* **24**, 5100516 (2018).
66. C. Antonelli, M. Shtaf, and A. Mecozzi, "Modeling of nonlinear propagation in space-division multiplexed fiber-optic transmission," *J. Lightwave Technol.* **34**, 36–54 (2016).
67. S. Buch and G. P. Agrawal, "Intermodal soliton interaction in nearly degenerate modes of a multimode fiber," *J. Opt. Soc. Am. B* **33**, 2217–2224 (2016).

68. P. Balla, S. Buch, and G. P. Agrawal, "Effect of Raman scattering on soliton interactions in optical fibers," *J. Opt. Soc. Am. B* **34**, 1247–1254 (2017).
69. E. Caglioti, B. Crosignani, and P. Di Porto, "Hamiltonian description of nonlinear propagation in optical fibers," *Phys. Rev. A* **38**, 4036–4042 (1988).
70. T. Ueda and W. L. Kath, "Dynamics of coupled solitons in nonlinear optical fibers," *Phys. Rev. A* **42**, 563–571 (1990).
71. Y. S. Kivshar, "Soliton stability in birefringent optical fibers: analytical approach," *J. Opt. Soc. Am. B* **7**, 2204–2209 (1990).
72. X. D. Cao and C. J. McKinstrie, "Solitary-wave stability in birefringent optical fibers," *J. Opt. Soc. Am. B* **10**, 1202–1207 (1993).
73. C. R. Menyuk, "Stability of solitons in birefringent optical fibers. I: equal propagation amplitudes," *Opt. Lett.* **12**, 614–616 (1987).
74. S. V. Manakov, "On the theory of two-dimensional stationary self-focusing of electromagnetic waves," *Sov. Phys. JETP* **38**, 248–253 (1974).
75. D. J. Kaup, B. A. Malomed, and R. S. Tasgal, "Internal dynamics of a vector soliton in a nonlinear optical fiber," *Phys. Rev. E* **48**, 3049–3053 (1993).
76. D. J. Kaup and B. A. Malomed, "Soliton trapping and daughter waves in the Manakov model," *Phys. Rev. A* **48**, 599–604 (1993).
77. R. Abraham and J. E. Marsden, *Foundations of Mechanics* (American Mathematical Society, 2008).
78. D. Anderson, "Variational approach to nonlinear pulse propagation in optical fibers," *Phys. Rev. A* **27**, 3135–3145 (1983).
79. V. M. Pérez-García, H. Michinel, J. I. Cirac, *et al.*, "Dynamics of Bose-Einstein condensates: variational solutions of the Gross-Pitaevskii equations," *Phys. Rev. A* **56**, 1424–1432 (1997).
80. B. A. Malomed, "Variational methods in nonlinear fiber optics and related fields," in *Progress in Optics* (Elsevier, 2002), Vol. **43**, pp. 71–193.
81. V. V. Afanasyev, Y. S. Kivshar, V. V. Konotop, *et al.*, "Dynamics of coupled dark and bright optical solitons," *Opt. Lett.* **14**, 805–807 (1989).
82. S. H. Strogatz, *Nonlinear Dynamics and Chaos: With Applications to Physics, Biology, Chemistry, and Engineering*, 2nd ed. (CRC Press, 2019).
83. M. Karlsson, D. Anderson, A. Höök, *et al.*, "A variational approach to optical soliton collisions," *Phys. Scripta* **50**, 265 (1994).
84. E. Caglioti, S. Trillo, S. Wabnitz, *et al.*, "Finite-dimensional description of nonlinear pulse propagation in optical-fiber couplers with applications to soliton switching," *J. Opt. Soc. Am. B* **7**, 374–385 (1990).
85. V. K. Mesentsev and S. K. Turitsyn, "Stability of vector solitons in optical fibers," *Opt. Lett.* **17**, 1497–1499 (1992).
86. C. J. McKinstrie and D. A. Russell, "Nonlinear focusing of coupled waves," *Phys. Rev. Lett.* **61**, 2929–2932 (1988).
87. P. Parra-Rivas, Y. Sun, F. Mangini, *et al.*, "Pure quartic three-dimensional spatiotemporal Kerr solitons in graded-index media," *Phys. Rev. A* **109**, 033516 (2024).
88. B. A. Malomed, F. Lederer, D. Mazilu, *et al.*, "On stability of vortices in three-dimensional self-attractive Bose-Einstein condensates," *Phys. Lett. A* **361**, 336–340 (2007).
89. V. Skarka, V. I. Berezhanii, and R. Miklaszewski, "Spatiotemporal soliton propagation in saturating nonlinear optical media," *Phys. Rev. E* **56**, 1080–1087 (1997).
90. V. Skarka and N. B. Aleksić, "Stability criterion for dissipative soliton solutions of the one-, two-, and three-dimensional complex cubic-quintic Ginzburg-Landau equations," *Phys. Rev. Lett.* **96**, 013903 (2006).
91. O. V. Shtyrina, M. P. Fedoruk, Y. S. Kivshar, *et al.*, "Coexistence of collapse and stable spatiotemporal solitons in multimode fibers," *Phys. Rev. A* **97**, 013841 (2018).
92. N. G. Vakhitov and A. A. Kolokolov, "Stationary solutions of the wave equation in a medium with nonlinearity saturation," *Radiophys. Quantum Electron.* **16**, 783–789 (1973).
93. C. Milián and D. V. Skryabin, "Soliton families and resonant radiation in a micro-ring resonator near zero group-velocity dispersion," *Opt. Express* **22**, 3732–3739 (2014).
94. P. Parra-Rivas, D. Gomila, F. Leo, *et al.*, "Third-order chromatic dispersion stabilizes Kerr frequency combs," *Opt. Lett.* **39**, 2971–2974 (2014).
95. M. Tliidi and L. Gelens, "High-order dispersion stabilizes dark dissipative solitons in all-fiber cavities," *Opt. Lett.* **35**, 306–308 (2010).
96. P. Parra-Rivas, S. Hetzel, Y. V. Kartashov, *et al.*, "Quartic Kerr cavity combs: bright and dark solitons," *Opt. Lett.* **47**, 2438–2441 (2022).
97. M. Karlsson and A. Höök, "Soliton-like pulses governed by fourth order dispersion in optical fibers," *Opt. Commun.* **104**, 303–307 (1994).
98. C. M. de Sterke, A. F. J. Runge, D. D. Hudson, *et al.*, "Pure-quartic solitons and their generalizations—theory and experiments," *APL Photon.* **6**, 091101 (2021).
99. G. Fibich, B. Ilan, and S. Schochet, "Critical exponents and collapse of nonlinear Schrödinger equations with anisotropic fourth-order dispersion," *Nonlinearity* **16**, 1809 (2003).
100. G. Fibich and B. Ilan, "Optical light bullets in a pure Kerr medium," *Opt. Lett.* **29**, 887–889 (2004).
101. M. Karlsson, D. Anderson, and M. Desaix, "Dynamics of self-focusing and self-phase modulation in a parabolic index optical fiber," *Opt. Lett.* **17**, 22–24 (1992).
102. M. Conforti, C. M. Arabi, A. Mussot, *et al.*, "Fast and accurate modeling of nonlinear pulse propagation in graded-index multimode fibers," *Opt. Lett.* **42**, 4004–4007 (2017).
103. K. Blow and D. Wood, "Theoretical description of transient stimulated Raman scattering in optical fibers," *IEEE J. Quantum Electron.* **25**, 2665–2673 (1989).
104. Q. Lin and G. P. Agrawal, "Raman response function for silica fibers," *Opt. Lett.* **31**, 3086–3088 (2006).
105. A. Hasegawa and Y. Kodama, "Guiding-center soliton in optical fibers," *Opt. Lett.* **15**, 1443–1445 (1990).
106. G. P. Agrawal, *Fiber-Optic Communication Systems*, 5th ed. (Wiley, 2021).
107. A. S. Ahsan and G. P. Agrawal, "Graded-index solitons in multimode fibers," *Opt. Lett.* **43**, 3345–3348 (2018).
108. A. S. Ahsan and G. P. Agrawal, "Spatio-temporal enhancement of Raman-induced frequency shifts in graded-index multimode fibers," *Opt. Lett.* **44**, 2637–2640 (2019).
109. W. H. Press, S. A. Teukolsky, W. T. Vetterling, *et al.*, *Numerical Recipes: The Art of Scientific Computing*, 3rd ed. (Cambridge University, 2007).
110. J. Lægsgaard, "Efficient simulation of multimodal nonlinear propagation in step-index fibers," *J. Opt. Soc. Am. B* **34**, 2266–2273 (2017).
111. J. Lægsgaard, "Efficient simulation of symmetric field propagation in parabolic-index fibers," in *Photonics & Electromagnetics Research Symposium* (IEEE, 2019), pp. 2416–2423.
112. M. Abramowitz and I. A. Stegun, *Handbook of Mathematical Functions with Formulas, Graphs, and Mathematical Tables* (Dover, 1964).
113. P. J. Davis and P. Rabinowitz, *Methods of Numerical Integration*, 2nd ed. (Academic, 1984).
114. M. W. Beijersbergen and L. Allen, "Astigmatic laser mode converters and transfer of orbital angular momentum," *Opt. Commun.* **96**, 123–132 (1993).
115. B. J. Puttnam, G. Rademacher, and R. S. Luís, "Space-division multiplexing for optical fiber communications," *Optica* **8**, 1186–1203 (2021).
116. P. J. Winzer, K. Nakajima, and C. Antonelli, "Scaling optical fiber capacities," *Proc. IEEE* **110**, 1615–1618 (2022).
117. C. Antonelli, A. Mecozzi, M. Shtaiif, *et al.*, "Stokes-space analysis of modal dispersion in fibers with multiple mode transmission," *Opt. Express* **20**, 11718–11733 (2012).
118. P. J. Winzer and G. J. Foschini, "MIMO capacities and outage probabilities in spatially multiplexed optical transport systems," *Opt. Express* **19**, 16680–16696 (2011).
119. T. Hayashi, T. Sakamoto, Y. Yamada, *et al.*, "Randomly-coupled multi-core fiber technology," *Proc. IEEE* **110**, 1786–1803 (2022).
120. A. Mecozzi, C. Antonelli, and M. Shtaiif, "Nonlinear propagation in multi-mode fibers in the strong coupling regime," *Opt. Express* **20**, 11673–11678 (2012).
121. D. Marcuse, C. Manyuk, and P. Wai, "Application of the Manakov-PMD equation to studies of signal propagation in optical fibers with randomly varying birefringence," *J. Lightwave Technol.* **15**, 1735–1746 (1997).

122. J. P. Gordon and H. Kogelnik, "PMD fundamentals: polarization mode dispersion in optical fibers," *Proc. Natl. Acad. Sci. USA* **97**, 4541–4550 (2000).
123. V. G. Makhan'kov and O. K. Pashaev, "Nonlinear Schrödinger equation with noncompact isogroup," *Theoret. Math. Phys.* **53**, 979–987 (1982).
124. S. V. Manakov, "On the theory of two-dimensional stationary self-focusing of electromagnetic waves," *Zhurnal Eksperimentalnoi i Teoreticheskoi Fiziki* **65**, 505–516 (1973).
125. P. K. A. Wai, C. R. Menyuk, and H. H. Chen, "Stability of solitons in randomly varying birefringent fibers," *Opt. Lett.* **16**, 1231–1233 (1991).
126. S. O. Arik, D. Askarov, and J. M. Kahn, "MIMO DSP complexity in mode-division multiplexing," in *Optical Fiber Communications Conference and Exhibition (OFC)* (Optica, 2015), paper Th1D.1.
127. A. Mecozzi, C. Antonelli, and M. Shtaif, "Intensity impulse response of SDM links," *Opt. Express* **23**, 5738–5743 (2015).
128. C. Antonelli, A. Mecozzi, and M. Shtaif, "The delay spread in fibers for SDM transmission: dependence on fiber parameters and perturbations," *Opt. Express* **23**, 2196–2202 (2015).
129. A. Mecozzi, C. Antonelli, and M. Shtaif, "Coupled Manakov equations in multimode fibers with strongly coupled groups of modes," *Opt. Express* **20**, 23436–23441 (2012).
130. S. Mumtaz, R.-J. Essiambre, and G. P. Agrawal, "Nonlinear propagation in multimode and multicore fibers: generalization of the Manakov equations," *J. Lightwave Technol.* **31**, 398–406 (2013).
131. A. Mecozzi, C. Antonelli, and M. Shtaif, "Soliton trapping in multimode fibers with random mode coupling," *arXiv*, arXiv:1207.6506 (2012).
132. W. H. Renninger and F. W. Wise, "Optical solitons in graded-index multimode fibres," *Nat. Commun.* **4**, 1719 (2012).
133. C. R. Menyuk, "Stability of solitons in birefringent optical fibers. II. Arbitrary amplitudes," *J. Opt. Soc. Am. B* **5**, 392–402 (1988).
134. W. H. Renninger and F. W. Wise, "Optical solitons in graded-index multimode fibres," *Nat. Commun.* **4**, 1719 (2013).
135. A. B. Grudinin, E. Dianov, D. Korbkin, *et al.*, "Nonlinear mode coupling in multimode optical fibers; excitation of femtosecond-range stimulated-Raman-scattering solitons," *JETP Lett.* **47**, 356–359 (1988).
136. Z. Zhu, L. G. Wright, D. N. Christodoulides, *et al.*, "Observation of multimode solitons in few-mode fiber," *Opt. Lett.* **41**, 4819–4822 (2016).
137. D. J. Richardson, J. M. Fini, and L. Nelson, "Space-division multiplexing in optical fibres," *Nat. Photonics* **7**, 354–362 (2013).
138. A. Antikainen, L. Rishøj, B. Tai, *et al.*, "Fate of a soliton in a high order spatial mode of a multimode fiber," *Phys. Rev. Lett.* **122**, 023901 (2019).
139. L. Rishøj, B. Tai, P. Kristensen, *et al.*, "Soliton self-mode conversion: revisiting Raman scattering of ultrashort pulses," *Optica* **6**, 304–308 (2019).
140. E. Fermi, J. Pasta, and S. Ulam, "Studies of nonlinear problems," Document LA-1940 (Los Alamos National Laboratory, 1955).
141. V. Zakharov, A. Pushkarev, V. Shvets, *et al.*, "Soliton turbulence," *JETP Lett.* **48**, 79–82 (1988).
142. A. Dyachenko, V. Zakharov, A. Pushkarev, *et al.*, "Soliton turbulence in nonintegrable wave systems," *Zh. Eksp. Teor. Fiz.* **96**, 19 (1989).
143. N. Akhmediev and M. Karlsson, "Cherenkov radiation emitted by solitons in optical fibers," *Phys. Rev. A* **51**, 2602–2607 (1995).
144. Y. Kodama, M. Romagnoli, S. Wabnitz, *et al.*, "Role of third order dispersion on soliton instabilities and interactions in optical fibers," *Opt. Lett.* **19**, 165–167 (1994).
145. F. Poletti and P. Horak, "Description of ultrashort pulse propagation in multimode optical fibers," *J. Opt. Soc. Am. B* **25**, 1645–1654 (2008).
146. F. Tani, J. C. Travers, and P. St. J. Russell, "Multimode ultrafast nonlinear optics in optical waveguides: numerical modeling and experiments in Kagome photonic-crystal fiber," *J. Opt. Soc. Am. B* **31**, 311–320 (2014).
147. J. C. Travers, "Optical solitons in hollow-core fibres," *Opt. Commun.* **555**, 130191 (2024).
148. D. Popmintchev, C. Hernández-García, F. Dollar, *et al.*, "Ultraviolet surprise: efficient soft X-ray high-harmonic generation in multiply ionized plasmas," *Science* **350**, 1225–1231 (2015).
149. X. Gao, G. Patwardhan, B. Shim, *et al.*, "Ionization-assisted spatio-temporal localization in gas-filled capillaries," *Opt. Lett.* **43**, 3112–3115 (2018).
150. B. A. López-Zubieta, E. C. Jarque, I. N. J. Sola, *et al.*, "Spatiotemporal-dressed optical solitons in hollow-core capillaries," *OSA Contin.* **1**, 930–938 (2018).
151. R. Safaei, G. Fan, O. Kwon, *et al.*, "High-energy multidimensional solitary states in hollow-core fibres," *Nat. Photonics* **14**, 733–739 (2020).
152. A. Lekosiotis, F. Belli, C. Brahms, *et al.*, "On-target delivery of intense ultrafast laser pulses through hollow-core anti-resonant fibers," *Opt. Express* **31**, 30227–30238 (2023).
153. C. Brahms and J. C. Travers, "HISCOL: high-energy soliton dynamics enable ultrafast far-ultraviolet laser sources," *APL Photon.* **9**, 050901 (2024).
154. M. Kolesik, J. V. Moloney, and M. Mlejnek, "Unidirectional optical pulse propagation equation," *Phys. Rev. Lett.* **89**, 283902 (2002).
155. M. Kolesik and J. V. Moloney, "Nonlinear optical pulse propagation simulation: from Maxwell's to unidirectional equations," *Phys. Rev. E* **70**, 036604 (2004).
156. J. C. Travers, T. F. Grigorova, C. Brahms, *et al.*, "High-energy pulse self-compression and ultraviolet generation through soliton dynamics in hollow capillary fibres," *Nat. Photonics* **13**, 547–554 (2019).
157. G. Genty, L. Salmela, J. M. Dudley, *et al.*, "Machine learning and applications in ultrafast photonics," *Nat. Photonics* **15**, 91–101 (2020).
158. L. Salmela, N. Tzipinakis, A. Foi, *et al.*, "Predicting ultrafast nonlinear dynamics in fibre optics with a recurrent neural network," *Nat. Mach. Intell.* **3**, 344–354 (2021).
159. M. Raissi, P. Perdikaris, and G. Karniadakis, "Physics-informed neural networks: a deep learning framework for solving forward and inverse problems involving nonlinear partial differential equations," *J. Comput. Phys.* **378**, 686–707 (2019).
160. G. E. Karniadakis, I. G. Kevrekidis, L. Lu, *et al.*, "Physics-informed machine learning," *Nat. Rev. Phys.* **3**, 422–440 (2021).
161. S. Cuomo, V. S. D. Cola, F. Giampaolo, *et al.*, "Scientific machine learning through physics-informed neural networks: where we are and what's next," *J. Sci. Comput.* **92**, 88 (2022).
162. G. Z. Wu, Y. Fang, Y. Y. Wang, *et al.*, "Predicting the dynamic process and model parameters of the vector optical solitons in birefringent fibers via the modified PINN," *Chaos Solitons Fractals* **152**, 111393 (2021).
163. Y. Fang, G.-Z. Wu, X.-K. Wen, *et al.*, "Predicting certain vector optical solitons via the conservation-law deep-learning method," *Opt. Laser Technol.* **155**, 108428 (2022).
164. B. W. Zhu, Y. Fang, W. Liu, *et al.*, "Predicting the dynamic process and model parameters of vector optical solitons under coupled higher-order effects via WL-TSPINN," *Chaos Solitons Fractals* **162**, 112441 (2022).
165. I. Chuprov, D. Efremenko, J. Gao, *et al.*, "Scaling transformation of the multimode nonlinear Schrödinger equation for physics-informed neural networks," *arXiv*, arXiv:2209.14641 (2022).
166. G. Z. Wu, Y. Fang, N. A. Kudryashov, *et al.*, "Prediction of optical solitons using an improved physics-informed neural network method with the conservation law constraint," *Chaos Solitons Fractals* **159**, 112143 (2022).
167. X. K. Wen, G. Z. Wu, W. Liu, *et al.*, "Dynamics of diverse data-driven solitons for the three-component coupled nonlinear Schrödinger model by the MPS-PINN method," *Nonlinear Dyn.* **109**, 3041–3050 (2022).
168. Y. H. Yin and X. Lü, "Multi-parallelized PINNs for the inverse problem study of NLS typed equations in optical fiber communications: discovery on diverse high-order terms and variable coefficients," *Chaos Solitons Fractals* **181**, 114595 (2024).